UC Santa Cruz
UC Santa Cruz Electronic Theses and Dissertations

Title
Testing theories for longterm accretion variability in black hole X-ray binaries

Permalink
https://escholarship.org/uc/item/55d0d405

Author
Cambier, Hal Jacques

Publication Date
2015

Copyright Information
This work is made available under the terms of a Creative Commons Attribution-NonCommercial-ShareAlike License, availalbe at https://creativecommons.org/licenses/by-nc-sa/4.0/

Peer reviewed|Thesis/dissertation

eScholarship.org Powered by the California Digital Library
University of California

UNIVERSITY OF CALIFORNIA
SANTA CRUZ

TESTING THEORIES FOR LONGTERM ACCRETION VARIABILITY IN BLACK HOLE X-RAY BINARIES

A dissertation submitted in partial satisfaction of the requirements for the degree of

DOCTOR OF PHILOSOPHY

in

PHYSICS

by

Hal J. Cambier

September 2015

The Dissertation of Hal J. Cambier
is approved:

Professor David M. Smith, Chair

Professor Mark Krumholz

Professor John Tomsick

Dean Tyrus Miller
Vice Provost and Dean of Graduate Studies

Copyright © by

Hal J. Cambier

2015

Table of Contents

List of Figures

Abstract

Testing theories for longterm accretion variability in black hole X-ray binaries

by

Hal J. Cambier

Many X-ray sources are now understood to be "black hole X-ray binaries" in which a stellar remnant black hole either tidally "squeezes" gas off a companion star, or pulls in some fraction the companion's wind. This gas can drain inward through a dense, thin disk characterized by thermalized radiation, or a sparse and radiatively-inefficient flow, or some combination of the two. Observations at other energies often provide crucial information, but our primary tools to study accretion, especially closest to the black hole, are X-ray spectra and their time evolution. This evolution includes numerous behaviors spanning orders of magnitude in timescale and luminosity, and also hints at spatial structure since draining is generally faster at smaller radii. This includes variability at time-scales of weeks to months which remains difficult to explain despite an abundance of possible variability mechanisms since direct simulations covering the full spatial and temporal range remain impractical.

After reviewing general aspects of accretion, I present both more and less familiar forms of longterm variability. Based on these, I argue the problem involves finding a physical process (or combination) that can generate repeatable yet adjustable cycles in luminosity and evolution of low and high energy spectral components, while letting the ionization instability dominate conventional outbursts. Specific models examined include: disks embedded in, and interacting with, hot, sparse flows, and another instability that quenches viscous-draining of the disk at more fundamental level. Testing these theories, alone and in combination, motivates building a very general and simplified numerical model presented here. I find that two-phase

flow models still predict excessive recondensation in LMC X-3 among other problems, while the viscosity-quenching instability may account for rapid drops and slow recoveries in disk accretion rate but also likely requires diffusivity orders of magnitude above the Spitzer value.

I also present complementary work on how total mass supply can vary (on day-week timescales) when the companion is irradiated by accretion-generated X-rays as the model is built with the intention (and features) to be used with more detailed disk models.

Acknowledgments

The advice of my committee improved this work dramatically, and their patience allowed me to complete it. I especially thank my advisor, Professor David Smith, for constant support and for more help than he will give himself credit.

Early work on this dissertation was supported by NASA grant NNX09AC86G, and two TA sabbatical grants from the Physics Department were also instrumental in completing this work.

The text of this dissertation includes reprints of the following published material:

Cambier, H. J. & Smith, D. M. (2013), Astronomical Physics Journal, Volume 767,46

Cambier, H. J. (2015), Monthly Notices of the Royal Astronomical Society, Volume 452,3620

where the co-author in the first paper directed and supervised the research which forms the basis for the dissertation.

Chapter 1

Accretion in general and black hole X-ray binaries in particular

Upon exhausting the supply of fusible elements in its core, a massive star will collapse inside its own Schwarzschild radius (R_{S}) to form a black hole unless neutron degeneracy pressure can arrest its collapse before this point, thus leaving a neutron star instead. Often this compact object had and retains a stellar companion. If the companion has a substantial wind, and/or if its envelope swells beyond the borders of its gravitational domain (i.e. Roche-lobe overflow), then the compact object may accrete more matter. In the latter case, the gas retains much angular momentum which must be transported out for the gas to wind its way down to the compact object as an optically thick, geometrically thin, nearly Keplerian disk. In the wind fed case much of the angular momentum of the matter that does accrete is - and must be - canceled as the compact object deflects some wind on opposite sides into collisions along its gravitational wake. This gas then streams in with low impact parameter and angular momentum severely limiting the disk size.

These are not the only type of black holes or ways to feed them. Super-massive black holes (SMBHs) with masses 10^6–10^9 times solar are now thought to inhabit the centers of most galaxies - including our own as indicated most dramatically by the orbits of stars near the Sgr A* radio source (Ghez et al., 2005; Genzel et al., 2010). Often these supermassive black holes feed on gas with low density, hindering radiative processes, and low specific angular momentum, leading to hotter, more spherical accretion flows. Furthermore, candidates for black holes with masses intermediate to these ranges have recently emerged, although for many systems such identification remains controversial (Miller & Colbert, 2004; Casares & Jonker, 2014).

Because astrophysical black holes - at least in general relativity - are described by just their mass and spin, many basic properties of accretion flows obey specific scalings with mass. For instance, the characteristic distance and orbital period scale linearly with mass leaving virial temperature near the horizon constant. Furthermore, to the outer accretion flow the differences between a black hole and neutron star are primarily tidal gravity and illumination spectrum. Results obtained studying a particular class of black hole systems can thus be applied more generally.[1]

This work focuses on the stellar-mass black hole X-ray binaries (BHXRBs), and specifically on those that obtain matter by Roche-lobe overflow. It is these conditions that readily lead to disks glowing in X-rays at peak accretion rates - redistributing considerable angular momentum over large distances to do so - but also allow hot, rarefied flows, and possibly combinations of the two. Many of the observations, including those I use directly, were carried out using the Rossi X-ray Timing Explorer (*RXTE*) which includes an All Sky Monitoring (*ASM*) instrument, and the Proportional Counter Array (*PCA*) used to obtain spectra.

Models for the regimes of a luminous disk, dim advection-dominated flow (ADAF), and

[1] Take Chartas et al. (2012) as a specific example of generalizing observations only possible with SMBHs. The authors examined X-ray spectra of a images from a gravitationally-lensed SMBH and saw spectral evolution consistent with caustics from lens imperfections first sweeping across an outer disk with a hard reflection spectrum, and then the power-law spectrum of the sparse, hot inner corona being reflected. Reasonable caustic speeds limit the corona size, and because microphysics like Compton-scattering cares about density and temperature versus black hole mass, this suggests limits on corona size for smaller black holes at lower accretion rates.

a quasi-hybrid [2] respectively date at least as far back as Shakura & Sunyaev (1973), Narayan & Yi (1995), and Ichimaru (1977). There is also consensus now that the viscosity these models invoke to transport angular momentum and release gravitational energy most generally comes from the magneto-rotational instability (MRI: Balbus & Hawley 1998) and/or magnetocentrifugal winds (Blandford & Payne, 1982; Pudritz & Norman, 1983).

In its simplest form, the MRI lends some credence to the Shakura-Sunyaev "α"-parameterization of Shakura & Sunyaev (1973) where the effective kinematic viscosity ν scales with sound-speed c_s and scaleheight H like:

$$\nu \sim \alpha c_s H \lesssim c_s H \tag{1.1}$$

thus defining α as some dimensionless angular momentum transport efficiency. The authors argued for the form and bound on ν based on a turbulence origin for the viscosity and the corresponding maximum eddy size (but they noted that the true origin might be magnetic). In terms of the MRI, Balbus & Hawley (1998) show that the radial-azimuthal component of the stress tensor $\tau_{R\phi}$ depends on the correlations of radial and azimuthal components of fluid and Alfvèn velocity fluctuations (δv, δv_A) from basic rotation flow via:

$$\tau_{R\phi} = \rho \left\langle \delta v_r \delta v_\phi - \delta v_{A,r}\, \delta v_{A,\phi} \right\rangle \tag{1.2}$$

where ρ is the mass density. They also note the instability condition on magnetic tension is analogous to the condition for a mechanical spring joining two masses at different radii to gradually transfer angular momentum from the inner mass to the other. I.e., when fluid elements undergo epicycles in a mild magnetic field, the out-of-step restoring tension drags on fluid in local apoastron and vice-versa. Too much magnetic tension, though, will reduce the dragged, unstable epicycles into stable, tightly-bound ones reflected in a vanishing difference of correlations.

[2] Ichimaru does not worry about the extreme low density limit and discards the advection term, but the ions still heat to ~virial temperatures through compressive heating and inability to dump their heat into the electrons

For a thin disk in vertical hydrostatic, equilibrium, $H \approx c_s/\Omega$ where Ω is the angular orbital frequency. Identifying $\tau_{R\phi} = \rho\nu(d\Omega/d\ln R)$, and further supposing that fluid and Alfvèn velocity fluctuations remain subsonic, and that competition between magnetic field growth and the accretion powering it reach some rough equilibrium, one recovers the previous Shakura-Sunyaev ansatz (e.g. Blaes 2004)

$$\nu \approx \left(\frac{\langle \delta v_r \delta v_\phi - \delta v_{A,r}\, \delta v_{A,\phi} \rangle}{c_s^2} \frac{d\ln R}{d\ln \Omega} \right) \frac{c_s^2}{\Omega} \rightarrow \alpha c_s^2/\Omega \tag{1.3}$$

The condition of vertical hydrostatic equilibrium also requires the dynamical timescale $t_\Omega \approx R/\Omega$ to exceed the thermal timescale, $t_{\rm th}$. Under these conditions, accretion can be treated as diffusion (Frank et al., 2002 - hereafter FKR02), where hotter flows typically drain faster, and the associated timescale for gas to accrete inwards from a particular radius R goes like

$$t_\nu \approx R^2/3\nu \tag{1.4}$$

This timescale is of order 100 days at the outer edge of a BHXRB disk and it is variability on this timescale that I focus on here, and abbreviate as "longterm".

At very high accretion rates, radiation pressure becomes competitive with gas pressure and then gravity, and the standard thin disk model breaks down. The Eddington luminosity, $L_{\rm E}$, where a spherical inflow with Thomson opacity would be momentarily "stopped" by radiation roughly characterizes the point of balancing gravity. Assuming a matter-to-energy accretion efficiency $\epsilon \approx 0.10$ defines a corresponding Eddington accretion rate, $\dot{M}_{\rm E}$, via $L = \epsilon \dot{M}_{\rm E} c^2$ where c is the speed of light (FKR02). Barring more exotic possibilities (e.g. Begelman 2002), radiation pressure should drive strong outflows that keep the ultimate accretion rate down unless the flow is so dense and/or rapid that it conveys many photons in faster than they wriggle out. Before reaching this point, radiation pressure likely exceeds gas pressure rendering the disk unstable to the radiation pressure instability (RPI: Lightman & Eardley 1974) while a highly advective slim disk (Abramowicz et al. 1988 and subsequent work) provides the next stable branch.

Transitions between the optically thick disk and optically thin ADAF regimes, in various configurations, still forms the basic paradigm for explaining hysteresis cycles between "low hard" and "high soft" states in the outbursts of transient BHXRBs reported since Miyamoto et al. (1995). In these cycles a hard power-law X-ray spectrum associated with quiescent ADAF accretion first rises in luminosity, then softens into a spectrum dominated by a modified-blackbody compononent associated with a disk, drops in luminosity, and hardens again into a power-law before fully fading back into quiescence all over a period lasting months to years (see Remillard & McClintock 2006, Ch. 2, and Figures 2.1 & 2.2). These models predict the soft state persists into lower luminosity by inverse-Compton-cooling the hot flow that threatens to evaporate and replace it – I save a more detailed discussion of these "two-phase" flows for later (Ch. 3.4) including a more careful examination of the kind we considered in Cambier & Smith (2013) – "CS13" – which is included as Ch. 6.

Although this hysteresis pattern is the most common, other BHXRBs behave much differently on these timescales which I'll elaborate in Ch. 2 and use to test theories for variability. Likewise, the physical processes involved or invoked in accretion theory are numerous, and I will discuss those that I consider most relevant in Ch. 3. These include: the variant of the two-phase flows mentioned above wherein the ADAF directly sandwiches the disk and can exchange mass, and an intriguing density- and temperature-dependent model for α (Ch. 3.5.2). To solve the viscous evolution of a disk, potentially coupled to a halo flow, for an assortment of underlying physics, I make the approximation of local thermal equilibrium to tabulate disk properties that are then referenced in an implicit method code, which I describe in Ch. 4.1. I find that difficulties the two-phase flow model faced before persist. I also find that stationary disk physics involving a density- and temperature-sensitive-α model, is qualitatively promising for capturing a wider range of observed disk behaviors, but the true physical basis and clear connection for the hard emission are wanting (Ch. 5).

Chapter 2

Longterm variability in BHXRBs is diverse

By far the most frequently seen and recognized variability patterns are transient outbursts with spectral hysteresis tracing counter-clockwise (CCW) "turtleheads" or "q's" in hardness vs. intensity diagrams (HIDs) as shown in Fig.(2.1). The overall rise and fall in luminosity is understood to be driven by the partial hydrogen ionization instability (PHII) in which adding mass to a given annulus burdens viscous dissipation too much to drain the extra mass (c.f. Ch. 3.1). The cause of hysteresis in the HID, is more debatable, though historically explained in terms of disk and ADAF limits as mentioned above.

The relative abundance of data on transients, and present difficulty in just understanding their hysteresis justifies the focus on these systems, but as Fig.(2.1) shows, there is certainly more to longterm BHXRB variability than transients and turtleheads, and comparing behaviors between these systems offers important clues and constraints. Several systems show persistent yet highly variable X-ray emission, and share a tendency to drop quickly and recover slowly in luminosity, but typically trace different hysteresis patterns. LMC X-3 has a disk blackbody

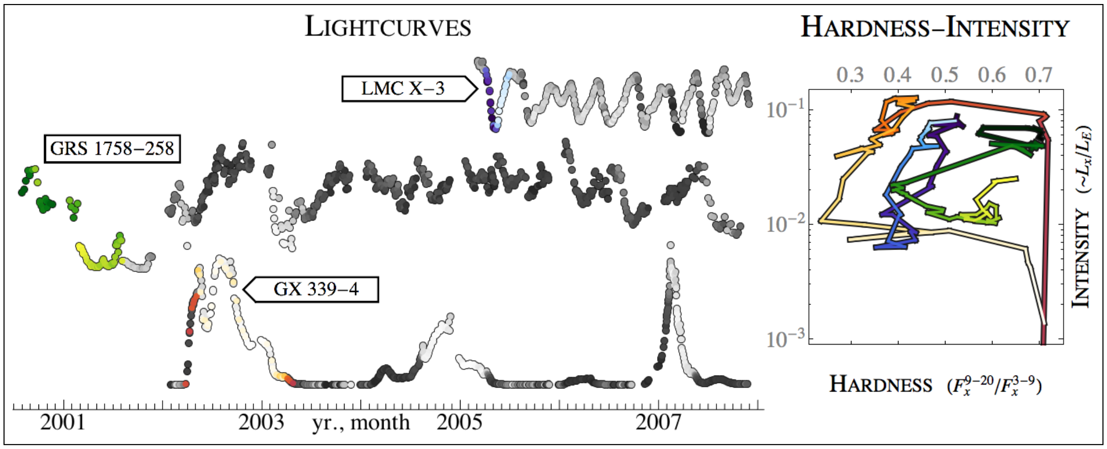

Figure 2.1: Segments of PCA data for three systems exemplifying major categories of long timescale variability in terms of: their total 3-20 keV intensity (left) with darker points for harder spectra, and their hardness-intensity cycles (right) with darker segments for earlier times. The cycles at right correspond to the colored portions in left panel. GX339-4 represents typical transient BHXRB behavior: fast rise and exponential decay associated with a "turtlehead" hysteresis loop (Ch. 2.2). LMC X-3 regularly contrasts transients with persistent emission, clockwise hysteresis, and opposite time-profile (Ch. 2.3). GRS 1758-258 represents a pair of persistent hard systems that follow a mirrored turtlehead.

spectrum at high luminosities, until a power-law component appears to herald a drop, the spectrum hardens while throughout the drop, before emission slowly softens and recovers. GRS 1758-258 and 1E 1740.7-2942 instead show harder spectra at high or increasing luminosity, and softer spectra before and during declines.

The behaviors are indeed tied to disk conditions versus some unknown property of individual systems as the transient 4U 1630-47 exhibited similar variability to LMC X-3 during a prolonged outburst while LMC X-3 recovered from its lowest, hardest state by tracing a turtlehead in the HID. Even in a well-monitored canonical transient like GX 339-4, longer outbursts are also interrupted by longterm luminosity variation reminiscent of the persistent systems. Systems reaching accretion rates even closer to Eddington, GRS 1915+105 and IGR J17091-3624, show highly chaotic longterm variability, but a vast assortment of well-defined patterns on kilosecond timescales.

This simple comparison more clearly defines the problem: I must find "machinery" which (i) leaves canonical transient outbursts alone, but (ii) "activates" when either outer accretion rates are high/steady, and/or outer surface density is high, and (iii) either becomes chaotic or insignificant at even higher supply rates or surface densities to explain GRS 1915+105 etc. It also (iv) tends to drive sawtooth lightcurves in the intermediate regime, and (v) is not fundamentally restricted to a single hysteresis pattern, though it fixes on turtleheads for transients, "p"-loops for GRS 1758-258, etc.

Before describing representative BHXRBs in Ch. 2.1, I discuss the general role astronomical parameters play viz. how inclination affects the appearance of hysteresis curves and whether it causes illusionary variability, while orbital parameters and companion type affect disk size and supply rate which can exclude variability mechanisms. I will then review specific systems as representatives of variability modes or mechanisms:

(Ch. 2.2) GX 339-4 and GRO J1655-40 represent transients; the former provides disk truncation measurements, and the latter displays strong magnetically-driven winds

(Ch. 2.4) 4U 1630-47 shows that a transient can execute clockwise (CW) hysteresis, and appears to launch magnetically-driven winds at least during the decline

(Ch. 2.3) LMC X-3 makes very persistent sawtooth cycles with CW-hysteresis in the absence of outer disk instability

(Ch. 2.5) GRS 1758-258 and 1E 1740.7-2942 also show persistent sawtooth cycles, but CCW hysteresis with a low, soft state unlike the transients and LMC X-3

(Ch. 2.6) GRS 1915+105 and IGR J17091-3624 demonstrate that longterm variability must become shredded at extreme mass supply

In Ch. 2.7, I then briefly summarize shorter timescale phenomena like those seen in GRS 1915+105, and the nature of longterm behavior for neutron star X-ray binaries. While my work doesn't address these topics directly, the kilosecond cycles resemble the longterm cycles in certain aspects, and accretion comparisons for a different compact object warrant some mention.

2.1 Expected effects of astronomical parameters

The masses of the black hole, $M_{\rm bh}$, stellar companion, $M_{\rm sc}$, and their orbital separation, a (or equivalently orbital period $P_{\rm orb}$) will set the radius at which the supply stream from the companion circularizes upon collisions with itself

$$R_{\rm circ} \approx \left(\frac{G(M_{\rm bh}+M_{\rm sc})P_{\rm orb}^2}{4\pi^2}\right)^{1/3}\left(1+\frac{M_{\rm sc}}{M_{\rm bh}}\right)\left(0.500-0.227\log\left(\frac{M_{\rm sc}}{M_{\rm bh}}\right)\right)^4 \tag{2.1}$$

where G is the gravitational constant (FKR02). The differential torque at the boundary means viscosity pushes the disk edge out a factor of 2-3 times further (FKR02).

The range of disk sizes in the systems considered here spans $\gtrsim 10^4$-$10^6 R_{\rm S}$. Within $\lesssim 10^5 R_{\rm S}$ and above $\dot{M}_d \gtrsim 0.001\dot{M}_{\rm E}$, disks become immune to the PHII. Compton-heated winds may cut off sharply this far out for sufficiently hard spectra, but otherwise continue to launch down to $\sim 3\times10^3 R_{\rm S}$ (Ch. 3.2), and likewise driving irradiation-driven warping inside this radius becomes difficult (Ch. 3.6) so these mechanisms can operate in all the systems considered.

Although our inclination to the orbital plane has no intrinsic effect, it can affect the lightcurves and spectra. Narayan & McClintock (2005) note that there is a trend for transients seen at lower inclination (more face-on) to exhibit "cleaner" lightcurves that agree quantitatively well with typical ionization-instability models while the lightcurves of systems seen at higher inclination show additional variation. This seems sensible for a number of phenomena, including a variable non-spherical corona, or mild outflow, but any mechanism producing substructure in the lightcurves must not disturb the underlying flow too severely to ruin the agreement found for low inclination systems. E.g. intense evaporation into a sandwiching ADAF flow would contradict this notion, as would strong outflows unless all BHXRBs seen at low inclination happened not to launch them. However, as a potential counter-example, GX339-4 likely has low inclination relative to us (Soria et al., 1999; Shidatsu et al., 2011) yet undergoes outbursts with and without substructure (i.e. the 2002-2003 versus 2007 outbursts in Fig.(2.2)).

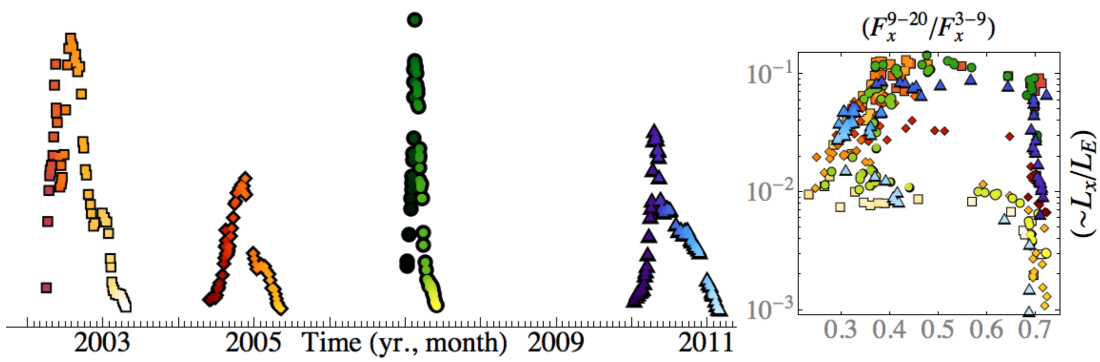

Figure 2.2: Like Fig.(2.1), but the lightcurves are specific to outbursts in GX 339-4 whose hysteresis are shown (and downsampled) in the hardness-intensity diagram at right with corresponding color schemes and symbols, and the points now run dark to light with time in *both* panels. Whatever processes drive variability can produce a range of luminosity variations in the soft state while preserving the overall turtlehead, and the luminosity at which transitions occur varies (more so for the hard-to-soft state transition).

Changing inclination, or black hole spin, also alters how gravity reprocessses spectra generated near the black hole as studied and discussed in an observational context by Muñoz-Darias et al. (2013). For face-on systems, photon trajectories from the disk to us should only be redshifted, but for greater inclination a greater fraction of the photons will reach us via blue-shifted trajectories (and beamed into a tighter cone); the spectrum will become relatively - and at some point absolutely - harder. For a varying inner disk radius, this could also affect the basic shape of hysteresis in the HID, but otherwise this effect is systematic so that gross features like CCW vs. CW remain meaningful.

2.2 Canonical transients and their variations

Both GX 339-4 (e.g. Muñoz-Darias et al. 2008) and GRO J1655-40 (e.g. Orosz & Bailyn 1997) have fairly well-measured component masses and orbital periods consistent with large PHII-susceptible disks, though GRO J1655-40 with its relatively massive companion ($\approx 2M_{\odot}$) may cut it close.

GX 339-4 in particular is popular for disk-truncation measurements: Miller et al. (2006a), Tomsick et al. (2009), Allured et al. (2013), and Plant et al. (2015) all performed measurements of the Kα fluorescence line in GX 339-4 at various total luminosities and stages of the hysteresis loop which are shown in Fig.(2.3). Plant et al. (2015) find relatively large radii with their "fiducial" spectral fit, but their measurements at $\sim 0.002L_{\rm E}$ agree qualitatively with the two-flow model for hysteresis as the radius is smaller when the system is leaving the soft state versus ascending the 'neck' of the turtlehead. However, Tomsick et al. (2009) found that the inner edge of the disk even reaches the innermost stable circular orbit (isco) while remaining in the hard state. Inner disk radii during moments of high and/or rising luminosity as found by Allured et al. (2013) further indicate that disk truncation is quite variable with respect to luminosity even accounting for stage in the hysteresis cycle, and I make a more quantitative comparison in Ch.5.1 based on the Allured et al. (2013) data which include inner disk temperatures.

GRO J1655-40 meanwhile enjoys similar fame for measurements of magnetic outflows

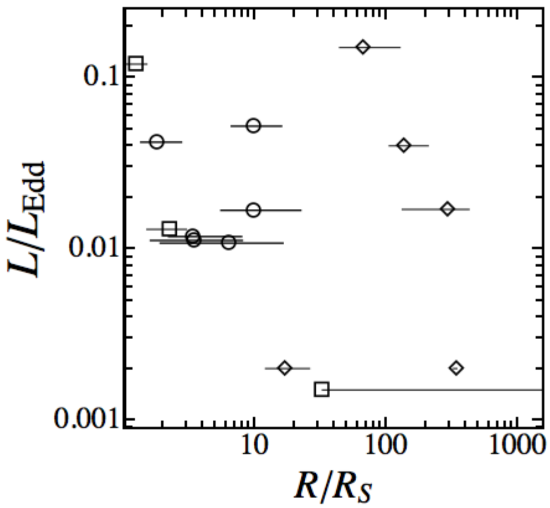

Figure 2.3: Inner radii measurements and their errors for GX 339-4 quoted from Tomsick et al. (2009) are shown as squares, Allured et al. (2013) as circles, and Plant et al. (2015) as diamonds, but note that to unify measurements reported as a ratio of $R_{\rm S}$ with ones reported in terms of the innermost stable circular orbit, I took the black hole spin to be 1 (in units of black hole mass). This does not impact the main feature of strong and varied disk survivability.

thanks to its relatively high inclination. Miller et al. (2004) only saw a "warm absorber" in GX 339-4, consistent with the low inclination inferred for GX 339-4 (e.g. Soria et al. 1999, Shidatsu et al. 2011)

Using observations with the Chandra X-ray telescope and RXTE observations of GRO J1655-40 during its 2005 outburst,Miller et al. (2006b) constrained the wind to be launched between $\sim 10 - 10^3 R_{\rm S}$ and found that a mass flux $\approx 10^{17}$ g/s best explained the degree and features of the absorption as the spectrum was too highly ionized for efficient line-driving, and Compton-heated winds (CHW) cut off this far inwards (see Ch. 3.2).

Miller et al. (2008), Kallman et al. (2009), and Kallman et al. (2009) followed up this work. Kallman et al. (2009) found lines with blueshifts implying both ~300 km/s and ~1000 km/s outflows, while Neilsen & Homan (2012) examined a Chandra observation made 20 days earlier, on March 12th, 2005, and RXTE observations, and saw no such highly blueshifted lines (as well as fewer lines in general). They eliminated changing ionization fraction as the cause behind the changing spectra, and found that a magnetically-driven wind moving inward between the observations was a real possibility. The first and second observations occur respectively during the initial rise, and a brief drop in $\dot{M}_d$ (see e.g. Sala et al. 2007). I will later refer to work showing low disk viscous transport (i.e. "low α") may be linked with magnetically-driven winds (Ch. 3.3) which lends credence to a variable α model that I investigate later as the cause of $\dot{M}_d$-drops (Ch. 3.5.2).

At the peak of especially intense outbursts, transients are seen entering an erratic "very-high" or "steep-power-law" (SPL) state where: the power-law cut off shifts to MeV energies exceeding the $\lesssim$100 keV reasonable for thermal Comptonization, and fitting with basic disk blackbody and Comptonization models imply the inner radii decreases further, blackbody temperature exceeds 1.5 keV, and flux no longer scales $\sim T^4$ (e.g. Tamura et al. 2012, Tomsick et al. 1999, Saito et al. 2006, Tamura et al. 2012). By considering Comptonization of the disk independently of the power-law component, Kubota et al. (2001) and Kubota & Makishima (2004) find the Comptonized disk emission scales quadratically with temperature while inner radius still decreases slightly and they interpret the SPL state as the manifestation of a slim disk.

2.3 LMC X-3 runs contrary to the transients

Of the known BHXRBs, LMC X-3 comes closest to realizing a steady-state Shakura-Sunyaev disk (SSD)[1]: the disk blackbody regularly dominates the spectra, and follows a Stefan-

[1]e.g. Shakura & Sunyaev 1973 or Frank et al. 2002

Boltzmann law with little scatter (see e.g. Ch.6) indicating that the inner disk geometry is fixed (i.e. neither truncated nor warped and precessing) and obscuration is low. However, the accretion rate and spectrum do vary significantly, and these behaviors have been well-sampled by RXTE. Being a "perturbed" SSD made it a logical place to start testing longterm variability theory in CS13.

Orosz et al. (2014) recently updated measurements for black hole mass, $M_{\rm bh} \approx 7M_{\odot}$, companion mass, $M_{\rm sc} \approx 3.4M_{\odot}$, and orbital period, $P_{\rm orb} \approx 1.7$ days for LMC X-3. These largely agree with previous measurements (Val-Baker et al., 2007; Soria et al., 2001), and a picture of LMC X-3 where the accretion disk is well-fed and relatively small ($\lesssim 10^5 R_{\rm S}$). This combination renders it nearly immune to the PHII, although it has transitioned to "anomalous low states" and the hard state proper on a few occasions (Wilms et al., 2001; Smale & Boyd, 2012). When recovering from the hard state, LMC X-3 executed sped-up classical CCW hysteresis which went through a much more erratic and luminous stage as shown in Fig.(2.4) alongside its typical fast-decline slow-recovery CW hysteresis.

The disk extends beyond the typical cutoff for Compton-heated winds, and the high average central X-ray luminosity should proficiently drive them. However, in CS13 (Ch.6), we showed by simple arguments that CHW, or any other severe loss or interruption in $\dot{M}_d$ at such large radii fails to explain the rapid $\dot{M}_d$-drops. We then focused on evaporation and condensation (EC) between the disk and a sandwiching ADAF means to accelerate and amplify drops in $\dot{M}_d$. Ch.6 covers this as well as the data and analysis specific to LMC X-3.

Using X-ray data from *ASM* and optical-infrared (OIR) observations of LMC X-3 by the *SMARTS* telescope, Steiner et al. (2014) performed a massive, global Monte-Carlo-Markov-chain fit to a parameterization of the X-ray and OIR lightcurves[2]. Comparing the OIR and X-ray emission, they found that the time-delay from OIR to X-ray emission increased with luminosity,

[2]The fitting includes orbital period for which they get 1.704805±3 d

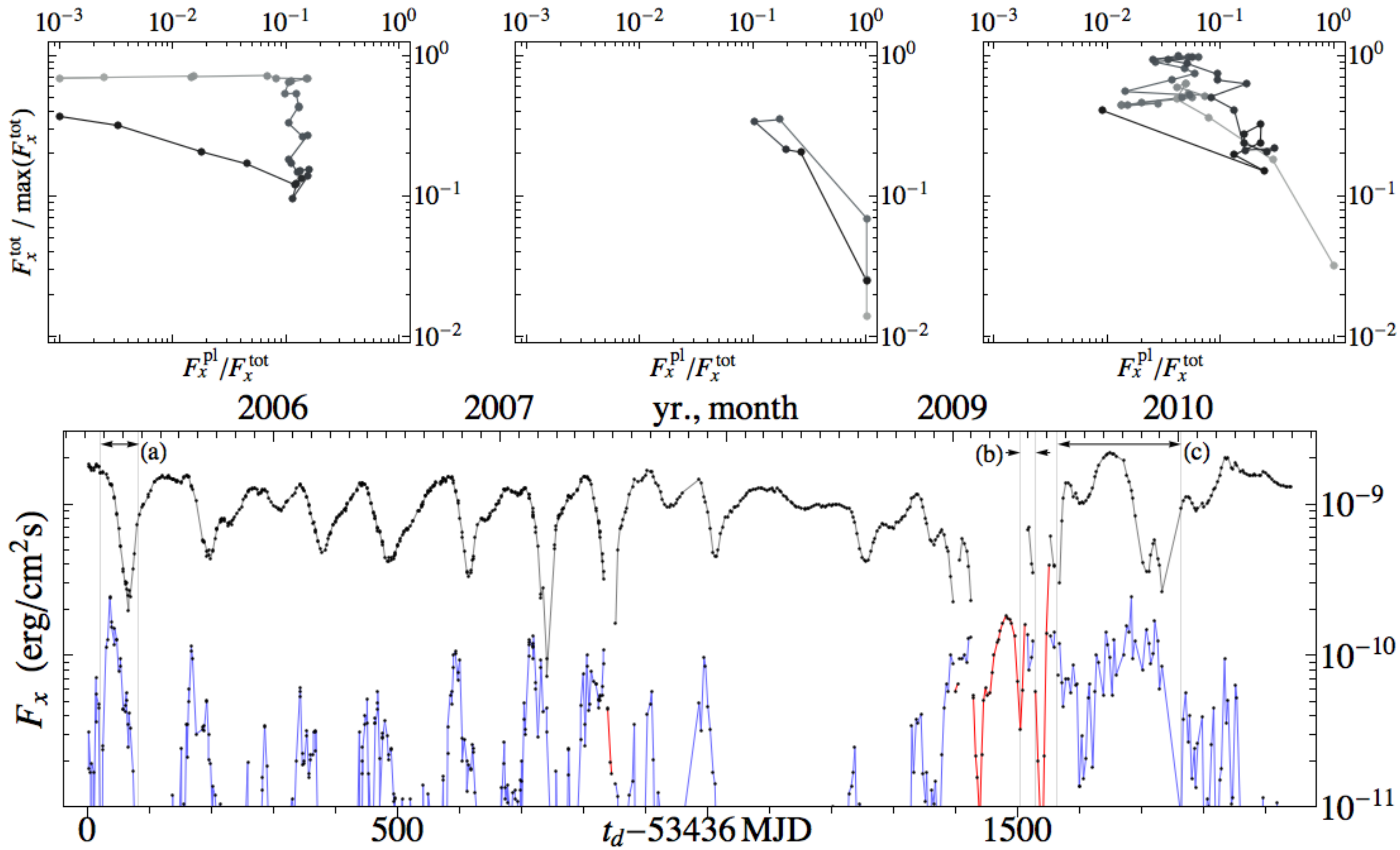

Figure 2.4: Bottom panel shows the X-ray lightcurve of LMC X-3 fit either to a sum of disk-blackbody (upper gray) and Comptonized (lower blue) components, or a pure power-law (lower red). The top panels show episodes of CW hysteresis, CCW hysteresis, and the hard-to-soft transition in LMC X-3, and the associated time intervals are marked (a–c) in the main panel. Note: power-law to total flux ratios were floored at 0.0001 for the Figures, but not the fits.

and that the magnitude of the preceding OIR flux; indicating a higher accretion rate at outer vs. inner radii. They attributed the latter to either winds and/or variation in the hot spot, and the former to α decreasing with $\dot{M}_d$. They further argued that the inverse relationship of α with the magnetic to gas pressure ratio (β) seen in shearing-box simulations (e.g. Ch. 3.5.1) could justify this claim if magnetic pressure remained relatively constant at these radii while gas pressure increased with accretion rate. The fact that β is more a proxy for poloidal magnetic flux in the simulations (Ch. 3.5.1) cited may bolster their argument if this large net flux reconnects and diffuses slowly, as the MRI may otherwise quickly adjust to maintain a particular β.

2.4 4U 1630-47 can shift between CCW & CW hysteresis

The proximity of 4U 1630-47 to the Galactic plane, a crowded and highly absorbed portion of the sky, hinders measuring the system's orbital parameters directly via optical spectroscopy, but Augusteijn et al. (2001) deduced major properties from infrared (IR) and X-ray observations during the 1998 outburst. The average X-ray luminosity suggested an orbital period greater than 13 hours, while the initial X-ray correlated decay and leveling off in IR singled out the IR counterpart and indicated a fairly bright and massive companion; $\lesssim 2M_{\odot}$. Attempts to discern the black hole mass through spectral properties by Seifina et al. (2014) give $\sim 10M_{\odot}$ which is consistent with the suggested orbital period, companion mass, and a disk of extent $\approx 1\times 10^5 R_{\mathrm{S}}$; near the threshold of the PHII. This may further account for the similarities to LMC X-3.

Regarding inclination: the system is non-eclipsing, but Kuulkers et al. (1998) and Tomsick et al. (1998) found sporadic dips in X-ray intensity lasting minutes, centered on orbital phases of $\sim$0.7-0.9, and characterized by softer spectra during the dip. The authors reasoned that clouds forming in the spillage from the supply-stream and disk collision (Frank et al.,

1987) were the most likely culprits implying an inclination $\sim 70°$ consistent with more model-dependent fitting, and interpretation of absorption lines as an equatorial wind in later work discussed below.

Individual outbursts in 4U 1630-47 differ as in GX 339-4, but recur on a nearly regular 611 day timescale (Jones et al., 1976; Parmar et al., 1995) with the exception of the sustained 2002-2004 outburst analyzed in part by Abe et al. (2005), in its entirety by Tomsick et al. (2005), and compared to the more typical 1998 outuburst by Tomsick (2006). Intense, sustained radio emission (Hjellming et al., 1999) accompanied the rapid X-ray luminosity rise in 1998 which also quickly reached the steep power-law (SPL) state. However, Hannikainen et al. (2002) periodically looked for radio emission during the 2002-2004 outburst but found none even when the system reached the SPL state in the second peak of the outburst. This lends credence to the mechanism by which the truncated inner edge accumulates poloidal magnetic flux between outbursts in the Begelman & Armitage (2014) net-flux model (Ch. 3.5.1) while also suggesting it has a limited effect on disk accretion.

It is also during this prolonged 2002-2004 outburst when 4U 1630-47 clearly traces CW hysteresis loops, and two of the radio non-detections occur at the start and middle of a disk decline. This may suggest that CW hysteresis is not driven by a process involving both build up of vertical flux and its inwards advection, but this statement is not conclusive (e.g. the flux may not reach the innermost disk to start a jet) nor necessarily remarkable if true.

Signs of strong outflows, magnetically or thermally driven, have also appear in 4U 1630-47. Kubota et al. (2007) found H-like and He-like iron absorption lines with blueshifts of $\sim$1000 km/s in *Suzaku* observations taken during the decay of the 2006 outburst. Further modeling by the authors indicated that the extent of the absorber was $\lesssim 10^4\ R_{\rm S}$. Using data taken during a more recent 2013 outburst by the *NUSTAR* X-ray satellite, King et al. (2014) find that even their lowest fit to ionization fraction suggest the wind must be launched within

400-2200 R_S, while noting that their single major absorption feature might either be a highly blueshifted (12900 km/s) He-like iron line or a moderately blueshifted (4200 km/s) H-like iron line. Unfortunately, no similar Suzaku observations took place during the 2002-2004 outburst, nor could similar absorption lines be distinguished in the RXTE spectra (Tomsick et al., 2005).

2.5 GRS 1758-258 and 1E 1740.7-2942 challenge high-soft and low-hard limits

Like 4U 1630-47, GRS 1758-258 is a heavily absorbed source making clear identification of the companion difficult. Initial uncertainties in the relative astrometry between radio, X-ray, and infrared observations left three candidates including one early-K type giant, and two stars tentatively identified as early-A type subgiants (Rothstein et al., 2002) while Smith et al. (2002) found a 18.45d periodicity in the X-ray data. Rothstein et al. (2002) noted that equating the X-ray and orbital periods, and requiring Roche-lobe overflow to explain the system's persistent X-ray emission, left only the early-K giant large enough to fill its Roche lobe. However, Muñoz-Arjonilla et al. (2010) improved the astrometry to find that only one the tentative blue subgiants falls within the refined position uncertainties. Furthermore, the X-ray periodicity has since appeared to shift slightly (Obst et al., 2013), strongly suggesting the X-ray periodicity corresponds to some superorbital period such as precession of a warped disk.

1E 1740.7-2942 lies close to the Galactic Center (famously so) so even less is understood about the companion or its orbit, but it shows X-ray spectral evolution and radio lobe morphology remarkably similar to GRS 1758-258 (Main et al., 1999). This provides some reassurance that they are both indeed galactic X-ray binaries, and some more motivation to study them, being members of a class versus one bizarre object.

Like LMC X-3, rapid-decline-slow-recovery cycles ~100d long are ubiquitous in the

X-ray luminosity of GRS 1758-258 (fig.2.5), but their duration and amplitude are more variable, and their associated hardness-intensity evolution is counterclockwise, i.e. the spectrum softens preceding and during declines, and hardens during recoveries. GRS 1758-258 also entered a ∼500d period of relatively low luminosity punctuated by a brief, mini-outburst of soft X-ray emission. This again reflects LMC X-3 somewhat, specifically the mini-outburst of hard X-ray emission during LMC X-3's own low luminosity state.

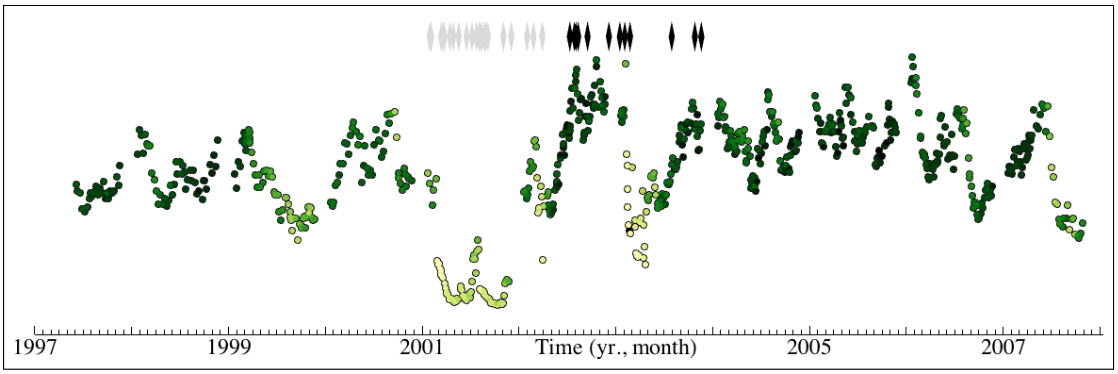

Figure 2.5: Extended GRS1758-258 lightcurve where darker points indicate harder spectra, and the gray/black diamonds show radio observations where emission was below/above noise level as listed in Soria et al. (2011).

Radio observations show that the jet is absent during the sustained low-soft state and preceding plunge, it returns once the X-ray spectrum becomes very intense and hard again, but survives well into - possibly throughout - the subsequent (and relatively deep) "p"-hysteresis cycle (Soria et al., 2011). Pottschmidt et al. (2006) find that the disk reaches temperatures and inner radii comparable to the sustained soft state during this subsequent hysteresis cycle, so disk truncation may not be strictly necessary for lauching a jet nor does it depend on or influence hysteresis in a fixed way.

Smith et al. (2007) suggest that a two-phase accretion flow could simply explain the soft-on-decline behavior if total mass supply, or total accretion rate further in, drops suddenly, as the halo flow will drain rapidly relative to the disk. Barring a very small disk, this still requires machinery at intermediate radii (besides evaporation now, evidently) to divert or arrest the accretion flow. The soft-when-dim nature of GRS 1758 also provides a complementary lower limit on how easily condensation must occur unless the seed corona is somehow kept very low.

More generally, GRS 1758-258 and the other systems together suggest that the luminosity profile in time corresponds more with whatever renders them persistent (or temporarily so for 4U 1630-47), e.g. something to do with the large accretion rate at large radii, typical surface density profile, etc., while the nature of spectral hysteresis may be tuneable with respect to the total luminosity in time - a recurring theme as we'll see.

2.6 Even wilder behavior is seen in GRS 1915+105 and IGR J17091-3624

For GRS 1915+105, a relatively clear picture of the system's properties has emerged especially due to recent work by Steeghs et al. (2013) (primarily in the optical) and Reid et al. (2014) (in the radio) which finds a more typical black hole mass of 9.6-14.14$M_{\odot}$, an orbital period of ≈34 days, an early K giant companion with mass roughly ≈0.4$M_{\odot}$, an inclination $\approx 60 \pm 5°$ derived from the radio lobes, and a system distance of 7.0–9.6 kpc. The evolved K-giant is consistent with the wide orbit and Roche-lobe overflow which may explain how the system sustains a near-Eddington average accretion rate over its observed history (especially considering how much of is likely lost to winds). However, Truss & Done (2006) find that the $\sim 10^6 R_{\rm S}$-sized disk may play the more important role by providing a reservoir ("filled up" by the PHII) large enough to sustain an outburst lasting over twenty years. Much less is known about the specific properties of the system IGR J17091-3624, but in terms of phenomenology it bears remarkable similarity with GRS 1915+105 besides at least one, relevant exception noted below.

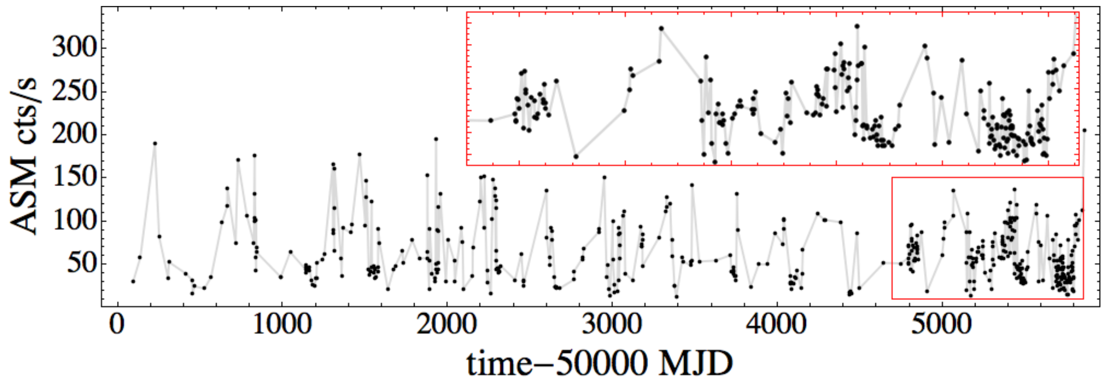

Figure 2.6: Plot of ASM count rates for GRS 1915+105 where measurements with error above 1.5cts/s and flux-to-error ratios below 5 are thrown out. The inset zooms in on the last 1000 days where sampling is more frequent and more likely to reveal ∼100d variability. No pattern in the long timecsale variability is evident.

These systems' behavior is a bizarre mix of many well-defined patterns on second-kilosecond timescales but very little order at longer timescales (see Fig.2.6). While "down-stream" of the physics I focus on here, these are at least important diagnostics though I won't be able to use them rigorously here. Many of these patterns involve rapid-decline-slow-recovery in total flux though, so they may also provide clues if analogous machinery operates at outer radii. Of these, the so-called ρ-cycles in particular are interesting as they trace CCW-hysteresis in GRS 1915+105, but CW-hysteresis in IGR J17091-3624 (Altamirano et al., 2011).

Absorption lines indicating substantial winds have also been seen in GRS 1915+105, and during ρ-cycles by Neilsen et al. (2011). The authors also find that properties of the wind beyond ionization fraction must change on comparable timescales during these cycles. However, typical velocities of ∼500 km/s implied by blueshifts place these winds at $\sim 10^5 R_{\rm S}$, i.e. well within the domain of a thermally-driven wind (Ch. 3.2) while a direct connection to magnetic winds on these timescales would be unexpected anyways.

In the following section Ch. 2.7 I mention various theoretical machinery invoked to explain the short cycles including the radiation pressure instability, and a particular model of evaporation-condensation. More generally, the different direction of hysteresis in these systems' ρ-cycles echoes the difference between GRS 1758-258 and LMC X-3 in their similar-but-longer cycles. This motivates searching for a similar mechanism with some flexibility regarding the spectral evolution.

2.7 Regarding shorter timescale phenomena and neutron stars

Although I focus here on long timescale variability in BHXRBs, I can not just dismiss shorter timescale phenomena or systems with neutron star primaries. Even in an ideal thin disk where variability has little chance to propagate upstream to large radii and timescales, the nature of variability further in constrains conditions upstream, and I have already mentioned well-established variability mechanisms (the PHII and CHW) where irradiation links inner disk conditions to the outermost flow.

At microsecond timescales, high-frequency quasi-periodic oscillations (HFQPOs) sometimes appear in black holes' X-ray emission but, so far, never in the soft, disk-dominant state - for a recent and systematic search over RXTE data we refer to Belloni et al. 2012. Where readily seen, they also tend to appear in roughly a 2:3 ratio, though more or less components at other ratios are possible, and various models can reproduce this among other features. For instance, Motta et al. (2014b,a) compare the spread of QPO frequencies observed in GRO J1655-40 and XTE J1550-564 to the relativistic nodal and vertical precession frequencies for just a test particle near a black hole and obtain fairly good agreement.

More directly addressing the absence of QPOs in the soft state: Dexter & Blaes (2014) show how the emissivity profile of a near-Eddington flow interior to the innermost stable circular orbit permitted by general relativity can both produce a steep power-law spectrum (dominating the disk component) and form a bandpass filter preferring signals at small radii like local vertical and acoustic oscillations that occur in a $\sim$2:3 ratio. Also promising and particularly relevant to models of hysteresis is the QPO model of a wave-instability trapped in the inner disk where Tagger & Varnière (2006) find that the strongest modes occur at integer multiples 2,3,...n of a common frequency, the growth rate rises with more poloidal magnetic field, and is overcome by draining in the thin-disk (i.e. disk-dominant) limit. This sensitivity to poloidal magnetic field is especially interesting in terms of jet launching, and the variability mechanisms I will discuss in Ch. 3.5.1

To address the variability at high accretion rates on intermediate - kiloseconds for BHXRBs - timescales as seen in GRS 1915+105 and IGR J17091-3624, the RPI is most typically invoked with some modification. For instance, in Nayakshin et al. (2000), the authors combine the RPI with an α that depends on temperature and density in a prescribed way (bearing considerable qualitative similarity to that in Ch. 3.5.2) and reproduce a large range of the patterns observed in GRS 1915+105 in terms of total flux, while Janiuk et al. (2002) instead consider a corona flow immersing the unstable disk and also generate lightcurves resembling some of the variability states in GRS 1915+105 in soft and hard components. Other proposed explanations include generalization of the magnetic wave instability discussed above to pumping outflows at larger radii (see e.g. Tagger et al. 2004, Caunt & Tagger 2001).

That GRS 1915+105 and IGR J17091-3624 both show ρ-cycles but with opposite directions implies the underlying physics must not tie flow conditions throughout the cycle to unique spectral states which introduces difficulties for two-phase accretion flow explanations. Again, this phenomenon warrants consideration as I try to explain behavior with similar time-profile and flexible hysteresis, but at much longer timescales. It even suggests some immediate possibilities: (i) both are driven by an intrinsic S-curve instability (c.f. Ch. 3.5.2,Ch. 5.2) with some flexible mechanism behind power-law emission, (ii) both involve magnetically-driven outflows triggered in a manner that is repeatable and tuneable.

My focus here is not on neutron stars, but they warrant a few remarks. Generally, neutron star X-ray binaries accreting via Roche lobe overflow will require smaller orbital radii and thus possess smaller disks rendering many systems immune to the PHII (Coriat et al., 2012). Some are fed at low enough rates that they exhibit the canonical fast rise and exponential decay with and without the "shoulders" sometimes seen in GX 339-4, and some (e.g. 4U1705-44) are persistent with stronger and more nuanced variability on the timescales that interest so (Done et al. 2007 - DGK07). Even the more transient-like neutron star X-ray binaries are not guaranteed to follow the turtlehead hysteresis curve (DKG07); rather Muñoz-Darias et al. (2014) find that spectral hysteresis does appear to take place but is limited to lower luminosities.

The nature of QPOs in Neutron star systems and their relation, if any, to black hole QPOs convolves two complicated asides so I refer the reader to a review by Lamb (2003). In short, there are currently enough observational distinctions between black hole and neutron star high-frequency QPOs to implicate different physics, thus avoiding contradictions with some of the interpretations for black hole HFQPOs given above.

Chapter 3

Many physical processes are involved or invoked

The longterm behavior described above involves a number of proposed or potential variability mechanisms, many already encountered, ranging from intrinsic, local effects to to the side effects of the disk warping as a whole. Here I describe prominent mechanisms that were most readily included in a one-dimensional model, as well as reviewing the ionization instability (Ch. 3.1) and Compton-heated winds (Ch. 3.2) since still play a significant role and find their way into the model.

Among the candidates are coupled two-phase accretion flows (Ch. 3.4), historically part of the transient paradigm, which I also investigated in the context of LMC X-3 as a means of evaporating disk flow at $\sim 10^3 R_{\rm S}$ to get rapid $\dot{M}_d$-declines and the coincident power-law emission (CS13, Ch.6). However, this straightforward production of the power-law emission may tie hysteresis too inflexibly to accretion rates, and an updated model for halo condensation (Ch. 4.3, Ch. 5.1) still predicts correlated, rises in blackbody and power-law flux in LMC X-3 that are not seen. Keeping the halo stationary, or having it plunge inwards without coupling to the disk subdues some of these issues, so I present these models in Ch. 3.4 also.

Magnetically-driven winds, MDW (Ch. 3.3), act to resolve multiple issues. They can subtract disk flow further inwards than CHW thereby accounting for rapid declines during persistent cycles, they may cool and stabilize disk flows otherwise expected to undergo the RPI, and they may remove halo liable to recondense. However, details for when a disk launches MDW, and predictions for how much mass they carry away remain hazy.

The efficiency of angular momentum transport, i.e. α, itself likely depends on flow conditions (Ch. 3.5). Numerous shearing-box simulations have shown α increasing with increasing net magnetic flux, so that poloidal flux generation, advection, and diffusion may alter accretion rates throughout the disk as invoked in a recent model of transient outbursts (Ch. 3.5.1). An instability akin to the PHII may also occur if the growth of the destabilizing magnetic field configuration behind the MRI cuts off sharply below relevant densities and temperatures (Ch. 3.5.2). This effect appears to arrest and release $\dot{M}_d$ further inwards for more persistent input $\dot{M}_d$ while tending to leave reservoir-driven outbursts alone, but may trigger at densities too small to be relevant.

In Ch. 3.6, I review warping of the disk, as it may affect irradiation of the disk thus influencing machinery like the PHII, and in extreme cases has been proposed to supplant all the above. I also give some background on mass transfer variation caused by accretion X-rays irradiating the donor, and summarize recent work I did on the topic which is presented more completely as Ch. 7.

3.1 The partial-hydrogen ionization instability (PHII) can drive overall outbursts

As hinted above, the PHII occurs when adding mass burdens dissipation due to an opacity transition. I'll give a heuristic review of the argument in FKR02 here as some key features reappear in other instabilities (Ch. 2.7,Ch. 3.5.2) considered in this work.

For a standard thin disk in thermal equilibrium, all of the following hold

$$\frac{T_{dc}^{7/2}}{\Sigma\kappa(\Sigma, T_{dc})} \approx \frac{T_{dc}^{4}/H_d}{\Sigma\kappa(\Sigma, T_{dc})} \sim T_{ds}^{4} \sim \nu_d \Sigma \sim \dot{M}, \tag{3.1}$$

where Σ is surface density, T_{dc} and T_{ds} are central (midplane) and surface temperatures, H_d is the disk scaleheight, and κ is opacity (FKR02). For $\dot{M}$ to rise and carry away an extra bit of mass of requires radiating away more energy. If κ depends very weakly on T_{dc}, then a slight increase in T_{dc} can raise cooling to reach a new equilibrium, or if κ grows rapidly enough with T_{dc}, then a slight decrease in T_{dc} boosts radiative cooling without a net drop in viscous dissipation ($\nu\Sigma$). Between these is an awkward range of temperature-dependence where lowering T_{dc} boosts radiative cooling at the expense of accretion while raising T_{dc} leads to runaway heating rendering extra accretion at thermal equilibrium impossible. More formally, for opacities of the form:

$$\kappa \sim \rho T_{dc}^{n} \tag{3.2}$$

the above argument implies instability for $7/2 < n < 13/2$. Disks encounter this awkward range of temperature dependence around ∼6500 K where, with increasing temperature, the dominant opacity mechanism shifts from encounters with negative hydrogen ions to free-free and free-bound absorption (e.g. Fig.3.1).

In terms of actual time dependent behavior, this burdened annulus will follow a limit cycle along an 'S'-curve (fig.3.2). It will first heat up in response to extra mass on a thermal

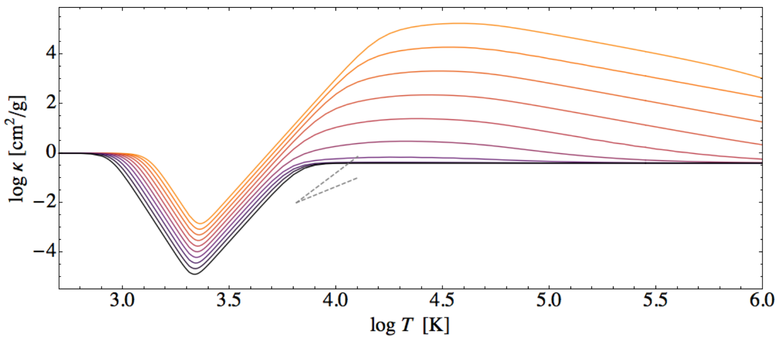

Figure 3.1: An approximation to Rosseland mean opacity (details in Ch. A) where log is $\log_{10}$ (throughout this work) and the curves span $\log(\rho/T_6^3)$ from 0 (orange) to -8 (purple). The left 'shelf' is where grain opacity dominates, which then drops as grains dissociate and molecular opacity dominates, quickly rises due to partial hydrogen ionization, and finally shifts from Kramer's-law to Thomson opacity. The gray wedge shows range of slopes yielding classic PHII.

timescale and thus quickly cross the opacity transition and once more accrete at thermal equilibrium at a greater rate and higher temperature along the so-called "hot" branch. This should quickly drain the annulus, but it can continue to drain below the transition surface density so long as the opacity allows a higher-temperature equilibrium. At some point, density and temperature drop enough that instability sets in again, and the annulus is back on the lower, "cold" branch.

In reality, the annulus may not be strictly limited to radiative dissipation, and placing it back into a disk will modify the criterion through advection, differential torques affecting the net accretion rate, etc. For conditions in the outer disk where this opacity transition can occur though, heating by X-ray irradiation due to the inner accretion flow has the greatest impact and can mitigate or shut off the PHII (Lasota, 2001; Coriat et al., 2012). Accounting for irradiation, and provided that α is large somehow on the hot branch, the overall PHII model works quite well, and work by Hirose et al. (2014) might now account for the jump in α as well. Their

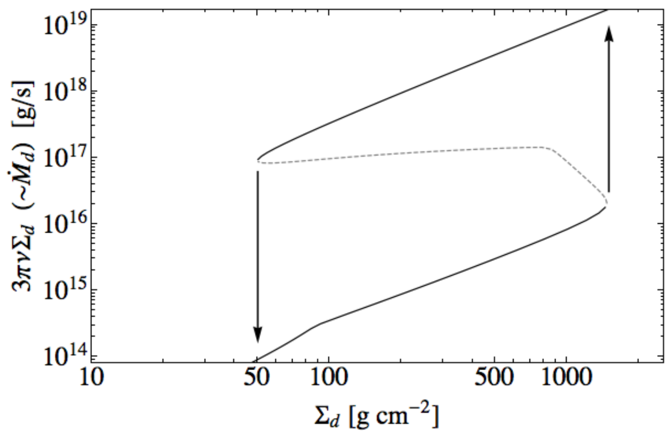

Figure 3.2: An example plot of Σ_d versus steady-state $\dot{M}_d = 3\pi\nu\Sigma_d$ for a non-irradiated annulus at $10^5 R_S$ with "cold" and "hot" α of 0.001 and 0.1. If this were the outermost annulus fed at an average rate of 10^{16}g/s, then it would accumulate mass until $\Sigma_d \gtrsim 1000$ g/cm^2 so that it jumped to the upper track where it would then have to drain mass faster than it is supplied mass, so that it eventually falls back onto the lower track.

simulations showed that weak radiative transport spurs convection which can "knead" up net vertical magnetic flux thus enhancing α (Ch. 3.5.1).

3.2 Compton-heated winds (CHW) affect the outer flow

Begelman et al. (1983) noted that accretion generated X-rays striking the outer disk can also deposit energy in the base of the outer disk's atmosphere, creating a pressure gradient that can launch a wind. The effect preferentially affects the outer disk where tidal gravity is weaker, and is strongly suppressed inside a radius R_{iC} where the virial temperature approaches the Compton temperature, T_{iC}, at which point X-ray irradiation can no longer provide the energy to escape. The average energy transfer per Compton scattering for an electron at temperature

T_e is roughly:

$$\epsilon_\gamma \left(\frac{4k_{\rm B}T_e - \epsilon_\gamma}{m_e c^2} \right) \tag{3.3}$$

where $k_{\rm B}$ is the Boltzmann constant, ϵ_γ the photon energy, m_e the electron mass, and c the speed of light (Rybicki & Lightman, 1986). The average photon energy in terms of the X-ray luminosity L and its energy distribution L_ϵ

$$\langle \epsilon_\gamma \rangle = \frac{1}{L} \int \epsilon_\gamma L_\epsilon \tag{3.4}$$

then determines

$$T_{iC} \equiv \langle \epsilon_\gamma \rangle / (4k_{\rm B}) \rightarrow 0.68 T_{bb} \tag{3.5}$$

for a blackbody spectrum of temperature T_{bb}, and often 10^7–10^8K for the frequently harder spectra of BHXRBs. This then sets

$$R_{iC} \equiv \frac{GM_{\rm bh}\mu}{k_{\rm B}T_{iC}} \approx (9.8 \times 10^{10}{\rm cm}) \left(\frac{M_{\rm bh}}{10M_\odot} \right) \left(\frac{10^8{\rm K}}{T_{iC}} \right) \tag{3.6}$$

with μ the molecular mass of the gas.

Simulations by Woods et al. (1996) later confirmed the Begelman et al. (1983) analytical theory and provided an amended prescription for CHW wind losses per area, $\dot{m}_w$. The prescription scales with radius, point-source luminosity, and mass in terms of $\xi = R/R_{iC}$, $\eta = L/L_{\rm E}$, $m_1 = M_{\rm bh}/M_\odot$:

$$\dot{m}_w = \frac{3 \times 10^{-5}}{m_1} \frac{\eta}{\xi^2} \left\{ \begin{array}{ll} 1 & : \eta \leq 0.1 \\ 0.707/\eta & : \eta > 0.1 \end{array} \right\} \left\{ \begin{array}{ll} 1 & : \xi \leq \xi_{\rm tr} \\ \xi/\xi_{\rm tr} & : \xi > \xi_{\rm tr} \end{array} \right\} \exp\left[\frac{-1}{2\xi} \left(1 - \left(1 + 0.25/\xi^2\right)^{-1/2} \right)^2 \right] \tag{3.7}$$

where

$$\xi_{\rm tr} = \left\{ \begin{array}{ll} 6 & : \eta \leq 0.01 \\ 6 + 5.4 \log(\eta/0.01) + 4.1 \log(\eta/0.01)^2 & : \eta > 0.01 \end{array} \right\}$$

For the inner disk around a black hole, the appropriate, effective X-ray luminosity to use would be diminished by a factor of $\cos i$ except for the strong gravity bending much of the flux back down towards the disk. Following Sanbuichi et al. (1993), I approximate the redirected flux from the inner disk as a fraction, 0.18, of that from a point source and scale L accordingly. Fig.(3.3), shows CHW losses for a couple values of T_{iC} can remove significant mass at high L, but becomes inefficient within a few thousand R_{S}.

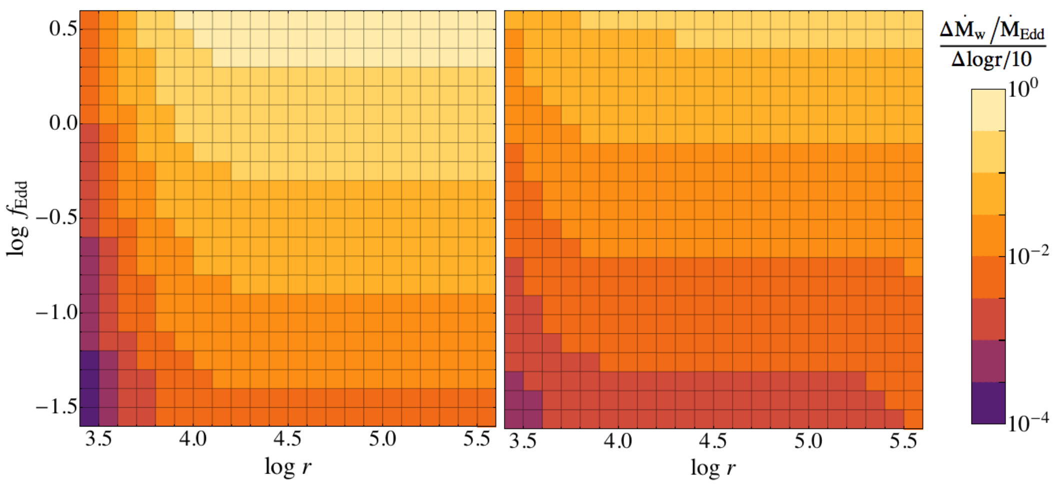

Figure 3.3: Wind-loss histogram in bins of $\log r$ ($r = R/R_{\mathrm{S}}$) versus log-bins in effective central luminosity as a fraction of Eddington luminosity (f_{Edd}). The tile color indicates mass loss in a tile as a fraction of $\dot{M}_{\mathrm{E}}$, and left/right panels show T_{iC} of 2.35×10^7K / 5×10^7K.

3.3 Magnetically-driven winds (MDW) are likely crucial

In describing systems like 4U 1630-47 and GRS 1915+105, I noted the observational evidence for outflows which thermal driving (e.g. CHW) can not explain, but magnetic driving can. For convenience, I summarize the basic heuristic picture below, as covered nicely by Spruit (1996) who also provides further detail and more references.

Barring intense currents or severe reconnection at the disk surface, any poloidal field threading the disk will try to remain rooted in it, and magnetic pressure will dominate thermal pressure immediately above the disk so that gas will slide along the field lines more than it drags. Still, as the lines try to rotate with the disk and fling out their mass load at high altitudes, they must bend back to some degree forming spirals for the mass to follow out in a magnetocentrifugal wind. Maintaining this shape further outwards eventually becomes impossible as magnetic tension fails to keep up with the increasing momentum of the gas (defining the Alfvèn point). Instead, a large coil of toroidal field builds up, also capable of driving outflow through toroidal magnetic pressure. The innermost tightly-wound "cones" in such a picture may form, or at least collimate, a magnetically-driven jet. As the gas slips away, it effectively extracts angular momentum from the system.

Blandford & Payne (1982) obtained a steady-state analytical solution for such a magnetocentrifugal wind including the minimal, perhaps ideal, 60° inclination to launch the jet. At lower inclinations tidal gravity trumps the centrifugal force along field lines, while higher inclinations may be unstable. This general principle holds in simulations, and accounts for the preferential detection of such winds in systems with high inclination.

Uncertainty in how much angular momentum a magnetic wind extracts versus disk viscosity complicates building simple analytical models with both. For example, works like Pudritz & Norman (1983) assume the wind is essentially responsible and work from there, while Li & Begelman (2014) consider an upper bound based on the disk properties, specifically that the Alfvèn velocity of magnetic field just poking out of the disk sets a maximum speed for the outflow (Ch. 4). Resolving this issue has the been the focus of recent efforts to either extend MRI shearing-box setups to scales large enough to study outflows, or use global magnetohydrodynamic (MHD) simulations that so far only partially resolve the inner disk MRI.

So far, such work indicates that MRI activity does not strictly inhibit outflow, but typically dominates angular momentum transport (Fromang et al., 2013) unless magnetic resistivity separately suppresses the MRI in the disk midplane (Bai & Stone, 2013b). In the case of protoplanetary disks including both Ohmic resistivity, strongest in the midplane, and ambipolar diffusion Bai & Stone (2013b) see especially fast (radial velocity several percent the local c_s), laminar wind-driven accretion flows form above and below the disk, acting like a “cold” halo flow in the two-phase flow models.Io & Suzuki (2014) largely agree, but also consider different global equations of state, from adiabatic index of 5/3 to isothermal (index of 1), which also serve as a proxy for increasing cooling efficacy. Doing so, they find that the more adiabatic cases lead to formation of a hot corona, and more stable and massive magnetic outflows.

This issue also has important consequences for inner disk stability as these winds may allow accretion with less local dissipation, thus keeping the flow cool enough to avoid triggering the radiation pressure instability - the specific application Li & Begelman (2014) had in mind. It may also banish the threat of a recondensing (accreting) corona. Finally, massive magnetically-driven winds would also have the simple and obvious effect on disk accretion rates of removing mass.

3.4 Two-phase accretion flows generalize disk and ADAF extremes

Since a thin disk can explain a blackbody component, while any hot ($\gtrsim 10^9$K) electrons present can Compton up-scatter the blackbody photons - or their own less luminous bremsstrahlung and synchroton radiation - into a hard power-law component, these were obvious elements to consider in modeling BHXRB spectra. The latter of these is generally labeled as a “corona” or “halo” and can take various forms in the different models. For example, to address observations of the persistent, wind-fed BHXRB Cygnus X-1, Ichimaru (1977) proposed a compressively-heated, radiatively-inefficient portion of the flow as the source of these hot electrons while Galeev et al. (1979) argued that a magnetic-carpet corona could exist whenever buoyant magnetic loops could poke out of the disk before reconnecting.

To also account for long-lived low-hard states in BHXRBs, Esin et al. (1997) generalized the virial component of the flow in Ichimaru (1977) to an ADAF and assumed the accretion flow picked the ADAF solution whenever possible. This implies a radially segregated flow requiring some disk truncation during any substantial power-law component emission which conflicts with observations (Ch. 2.2). Earlier, Chakrabarti & Titarchuk (1995) supposed instead that viscosity dropped with height, and explored the consequences for some seed halo with low angular momentum sandwiching the outer disk. This halo flow falls more than it viscously drains until it approaches its circularization radius where centrifugal force piles it up and it shocks if viscosity fails to drain it enough. The resulting hot "centrifugally-supported boundary layer (CENBOL)" serves as the corona and may evaporate a weak disk component.

Earlier still, but in the context of white dwarf accretion, Meyer & Meyer-Hofmeister (1994) - hereafter MMH94 - noted that thermal electron conduction in a hot corona embedding a disk could evaporate the disk if it failed to radiate this extra heat. They also assumed this corona possessed similar α-viscosity to the disk so that it heated and drained quickly inward thus "siphoning" the disk onto the white dwarf. Those authors, among many others pursued this concept in the context of BHXRBs and state transitions including Różańska & Czerny (2000), Janiuk et al. (2002), Meyer et al. (2007), Liu et al. (2007), Mayer & Pringle (2007), and Bradley & Frank (2009) - hereafter RC2000, JCS2002, MLMH07, LTMHM07, MP07, and BF09. These exemplify what I denote as the evaporation-condensation (EC) models which further subdivide into primarily analytical or numerical models.

LTMHM07 and BF09 follow MMH94 by partitioning the disk-corona transition layer into a thin radiative skin just above the disk, and regions above dominated by electron thermal conduction where electrons and protons are coupled, and then density drops such that they quickly decouple. RC2000, JCS2002, and MP07 instead assume the transition layer is a single zone of constant pressure where ion temperature rises linearly with height and density is then inversely proportional to ion temperature. Under these assumptions, Różańska and Czerny numerically solve the energy transport equation as a continuous function of height.

Of these, JCS2002 and MP07 also study time-dependence, and MP07 do so for radii and timescales of prime interest here. Indeed, this work relating to EC is arguably the spiritual successor of MP07. In CS13, we solved a time-dependent disk flow in combination with the LTMHM07 prescription for EC and crudely modeled the corona as an instantaneous stream. The model offered a solution for the behavior of LMC X-3 given only the assumption of small pulses of corona flow at $\sim$100d intervals: evaporation amplified this seed flow, peaking around 10^2–$10^3 R_\mathrm{S}$ so that drops in $\dot{M}_d$ at the inner edge took on the order of 10 days, while recovery required the full viscous timescale. The corona flow itself Comptonizes disk emission so that we would observe a pulse in the power-law component whose rise anticipated a rapid drop in disk rate. Ch.6 provides details, and also describes the problem of excessive recondensation at temperatures $\gtrsim$1 keV, frequently encountered in LMC X-3, where the inverse-Comptonization creating the power-law component also cools the corona enough for much of the evaporated flow to recondense thus predicting substantial, correlated rises in both disk-blackbody and power-law components. MP07 also encountered this "sympathetic" mode, but LMC X-3 does not exhibit such behavior.

We speculated on possible remedies to the issue, and examined EC models more carefully. For instance, in LTMHM07, the authors make an approximation that allows the maximum electron temperature in the transition layer to drop below the coupling temperature at large radii which BF09 address and repair, but in BF09 the authors do not consider inverse-Compton cooling. These prescriptions also admit evaporation rates exceeding the viscous energy budget, and their common use of Spitzer electron thermal conduction loses validity. I quantify this further and describe corrections in Ch.4.3, but these fixes still do not provide strong and selective suppression of recondensation in conditions relevant to LMC X-3.

In Liu et al. (2002) and Liu et al. (2012), the authors applied the same conduction and cooling processes in the above EC models, but to a static corona of emerging magnetic flux tubes and powered by large-scale reconnection, thus updating aspects of the Galeev et al. (1979) picture. However, these models still tends to generate correlated rises in disk and power-law emission without additional energy injection (or other modifications to corona dissipation), for which Liu et al. (2012) invoked more heating by buoyant and reconnecting fields that remain "available" even at lower accretion rates in contrast to the Galeev et al. (1979) model.

Meanwhile, tension still exists between this modified prescription and the disk truncation measurements in GX 339-4 (Ch. 2.2) which I show in Ch. 5.1. This further indicates that EC models, if viable, require some additional physics to explain varying recondensation efficiency.

3.5 Perhaps the α-constant isn't

3.5.1 Net magnetic flux may boost α

One simple and widely replicated experiment involving α has been to impose some net magnetic flux in shearing box simulations, either poloidal (e.g. Bai & Stone 2013a, Sai et al. 2013), toroidal (e.g. Simon & Hawley 2009), or both (e.g. Lesur & Longaretti 2009). Net magnetic flux in either direction simply tends to increase α.

Beyond the importance of this dependence in general, Begelman & Armitage (2014) apply this specifically towards a proposed scenario for hysteresis. Using the fact that poloidal flux will tend to diffuse outward through the disk unless advected inward (Lubow et al., 1994), and supposing that reconnection at the inner truncated edge of a disk can build up field stochastically by reconnection, they argue that the pre-outburst disk will drain down loaded with poloidal magnetic flux which will seed launching of a magnetic jet and raise α. If advection and diffusion can remove the flux, α will drop explaining the return at lower luminosity. The substructure in transient outbursts, and alternate hysteresis patterns may pose a challenge. The concept of moving magnetic flux affecting the disk state is important regardless.

I included a simple single-donor-cell diffusion model of magnetic flux transport approximating Lubow et al. (1994) with plans to better test the model. Guilet & Ogilvie (2012) find the situation is more complicated, though still perhaps amenable to a simple transport, but I did not pursue this aspect in more detail. To describe the dependence of α on vertical flux in general, I specifically follow the scaling found by Bai & Stone (2013a), and I assume that this enhancement of α is trumped by increased reconnection as introduced in the next section.

3.5.2 Non-ideal MHD effects may branch α (PBα)

A more stringent, microscopic cause of varying α may result from the increasing difficulty of magnetic reconnection when small-scale ("microscopic") viscosity responsible for bringing opposing field lines together, ν_m, is small relative to the microscopic diffusivity (or resistivity) η_m responsible for reconnecting fields, i.e. small magnetic Prandtl number $\mathcal{P}_m = \nu_m/\eta_m$. Lesur & Longaretti (2007) examine this numerically and find where α quenches in terms of fluid and magnetic Reynolds numbers, $\mathcal{R}_h = H^2\Omega/\nu_m$ and $\mathcal{R}_m = H^2\Omega/\eta$:

$$\mathcal{R}_h \lesssim \max\left(10^2, 10^5/\mathcal{R}_m\right) \tag{3.8}$$

Balbus & Henri (2008) and Potter & Balbus (2014) consider a simpler dependence on $\mathcal{P}_m$ alone (i.e. α quenches below $\mathcal{P}_m = 1$), but place this dependence in an actual BHXRB context. For this reason, I labeled this the Prandtl-branching-α, "PBα", model, but I will consider the non-simplified form too. Potter & Balbus (2014) additionally considered time-dependence, and radiative viscosity (ν_r) versus Spitzer viscosity (ν_S) alone, while basing their diffusivity on Spitzer resistivity alone (ν_S):

$$\mathcal{P}_m = \frac{\nu_m}{\eta_m} = \frac{\nu_S}{\eta_S} + \frac{\nu_r}{\eta_S} \tag{3.9}$$

Since the only resistivity in the net-field simulations of Bai & Stone (2013a) was a numerical hyper-resistivity turned on just to dissipate simulation-crippling patches of extremely high magnetic field, I will assume that the Potter & Balbus limitation takes precedence when combining the models.

In practical terms, the PBα model operates much like the classical PHII prescription in which there are critical surface density profiles - increasing as power-laws in radius - where α jumps in value, except the transitions take place much further in, and it directly affects α versus viscosity as a whole via opacity.

However, while Oishi & Mac Low (2011) obtain similar results, they argue that the range of magnetic Reynolds number necessary to quench α are not realized in X-ray binary accretion disks, i.e. they are simply never resistive enough to experience this effect.

Initially ignorant to the objections of Oishi & Mac Low (2011), and interested in a model that independently explained rapid decline and slow recovery in the disk component, I pursued the idea and found that variants of the model can generate disk light curves qualitatively similar to 4U 1630-47 and LMC X-3 (including the state transitions), but with smaller timescales and accretion rates, motivating further investigation. For example, if the effective resistivity due to small-scale electric fields generated within the plasma is orders of magnitude larger than the Spitzer resistivity used, or if turbulence enhances magnetic diffusivity to a similar degree, then the PBα model may apply. I examine and quantify this a bit more in Ch. 5.2.

How (or if) this effect connects to power-law emission is also uncertain. The notion that magnetic loops survive to buoyantly rise when reconnection is slow in the disk suggests that the power-law component should correlate with the high α_d, thus high T_d state, posing an obvious problem.

3.6 Warping of the outer disk may strongly affect some systems

Various asymmetric forces might warp and tilt the disk out of the orbital plane, and even subtle deformations may drive noticeable variability by coupling with other processes. For example, the irradiation-sensitive PHII can amplify effects of self-shadowing or increased exposure of the outer disk to X-rays. Also, more of the supply stream can flow past the rim of a precessing disk or even strike its faces for larger tilts which may set the seed halo flow in two-phase flow models besides changing how the disk obtains mass. This effect may also explain modulation on timescales both slightly below and above the orbital period in Cataclysmic Variable (white dwarf as the primary) systems (Wood et al., 2011). In complementary work, I even find that the shadow of a precessing and warped disk may modulate supply rate on orbital timescales as it alternately shutters irradiation patches on the companion (Ch. 3.7).

The asymmetry of the Roche lobe potential may supply the appropriate force to grow vertical perturbations into a tilted, precessing disk, though Lubow (1992) found that (i) the lowest practical mode requires $M_{sc}/M_{bh} \lesssim 0.25$ or a circularized disk fits well inside the 3:1 orbital resonance necessary to drive the mode, and (ii) the growth rate of higher order modes decreases rapidly. Later work including Larwood et al. (1996), and Larwood (1998) used SPH simulations to study the shape and evolution of the disks for parameters matching observed systems (also confirming the overall conclusions of Lubow 1992). Although BHXRBs fed by Roche-lobe overflow tend to have low mass ratios, GRS 1758-258 and 4U 1630-47 may meet the requirements for significant tidally-driven warping and precession, while LMC X-3 fails by having too massive a companion.

Radiation flux may also apply asymmetric force on outer annuli given some perturbation in either (including warping of the inner disk by general relativistic effects mentioned below). Pringle (1992) did exploratory modeling (based on work in Papaloizou & Pringle 1983 for a generic driving force), followed up with simulations for relevant BHXRB parameters in Wijers & Pringle (1999). Wijers & Pringle found that the picture of discrete, discernible modes in previous analyses (e.g. Maloney et al. 1996 and Maloney et al. 1998) did not carry over well, but did recover the scaling and approximate timescale for growth of a global warp

$$t_{iw} \approx \frac{10\eta}{\epsilon r^{1/2}} t_{\nu} \tag{3.10}$$

where ϵ again stands for matter-to-luminosity efficiency (∼10% for a disk) and η is the ratio of vertical to radial shear viscosity which they took to be 1. Foulkes et al. (2010) also obtained similar results with a smoothed particle hydrodynamics (SPH) code. Direct simulations of irradiation driven warping also confirm and resolve how more severe warps limit themselves through self-shadowing.

The gravitational potential near a spinning black hole is also asymmetric and the possibility of this raising warps subject to (Lense-Thirring) precession in the misaligned inner disk has been recognized since Bardeen & Petterson (1975). More recently, Nixon et al. (2012) use SPH simulations to study this effect at larger radii, and communicated further outward by viscosity, and conclude that tearing of the disk may be possible, and Nixon & Salvesen (2014) propose this may drive hysteresis entirely. However, grid-based MHD simulations by Sorathia et al. (2013) disagree on the extent of the effect which the authors attribute the non-isotroptic nature of MRI viscosity captured in their simulations.

This does not exhaust the ways in which a warp might form (e.g. Montgomery &

Martin 2010, or the p-modes of the inner disk mentioned in Ch. 2.7), but summarizes some widely recognized and well-studied ones. In CS13, I supposed that irradiation-driven warping in LMC X-3 might drive overall cycles in conjunction with evaporation-condensation as (i) a warp grows in the soft, high state, (ii) more of the stream overshoots the disk edge (per orbit) or strikes its face providing more virialized halo to seed the corona, which (iii) evaporates disk material and produces the power-law spectral component. However, for parameters relevant to LMC X-3, Wijers & Pringle (1999) found the warp might take ~60 days to grow, and longer for non-isotropic viscosity, putting some pressure on this mechanism. Furthermore, this relies on the assumption that the virialized spillage from the hot spot can promptly undergo the MRI to become an ADAF-like flow sandwiching the disk.

If warps attains very large amplitudes or if the disk tears completely, more frequent dipping in X-ray light curves should be seen - especially if such tearing is a necessary ingredient for hysteresis. If dramatic warping at large radii due to the Bardeen-Petterson effect is vindicated though, then perhaps black hole spin is finely aligned with the orbital plane in BHXRBs (or at least the sources we see and recognize as such). Unfortunately, even fairly basic treatment of large warps requires 3D simulations so I do not implement them.

3.7 Irradiating the donor star may modulate the total supply-rate (SRM)

Besides striking the outer disk, some of the X-ray flux can irradiate the donor star. The possible consequences have been investigated at least as early as Anderson (1975) where the vicinity of the inner Lagrange point "nozzle" is directly irradiated and the mass transfer rate, $\dot{M}_s$, varies strongly[1] with incident luminosity. More of the early history is summarized in

[1]up to the 3/8 power of the ratio of incident to intrinsic luminosity

the introduction of Cambier (2015); included as Ch. 7. Eventually, Viallet & Hameury (2007) performed simple 2D hydrodynamic simulations (focused on companions in Cataclysmic Variable systems), and confirmed that shading of the nozzle by the disk gives ample time for gas to cool and subdue the dramatic luminosity dependence predicted before, while deflection of the gas both into and away from the nozzle region by strong coriolis forces complicates the variation.

Modeling changes to mass transfer with more detail is ideal even if it simply constrains the boundary conditions in the present context, but it may have broader implications. For example, if significant, systematic irradiation-boosted mass transfer occurs in systems like GRS 1915+105, then this may prolong the outburst, or supplant it for extreme enhancement. As with Compton-heated winds, variations in $\dot{M}_s$ will undergo viscous dampening, and possibly by the full extent of the disk this time. However, Kunze et al. (2001) find that the transfer stream may deposit mass further inwards when $\dot{M}_s$ suddenly rises, and mass transfer with more modulation for a given longterm average supply rate may still trigger outbursts for the PHII more easily.

This motivated updating and extending updated the model of Viallet & Hameury (2007) to include a robust hydrodynamics scheme, a better approximation of the Roche lobe geometry, and a sink term which includes coriolis lift force and indicates the immediate, ballistic trajectories the gas will follow. I applied the model to study how a warped, precessing disk's shadow would affect mass transfer in several types of systems including LMC X-3 and GRS 1915+105 analogs. So long as the Coriolis force or existing weather does not interfere, I found that the shadow drove cycles in $\dot{M}_s$ where: the disk shades one irradiation patch, ambient gas pools into the newly low-pressure region, and then gets squeezed between the edge of the returning irradiation patch and the other patch.

A more general lesson from the LMC X-3 simulations is that the high intrinsic surface temperature of the companion leaves little contrast between irradiated and un-irradiated regions, so supply-rate modulation is likely small barring MHD effects not accounted for in the simulations. When the companion is cooler, and the maximum North/South extent of the shadow is greater (so that more mass is pooled and pushed per cycle), modulation can become substantial. The cool companion and long orbital period in GRS 1915+105 presents a fairly extreme case, and $\dot{M}_s$ varies by $\sim$2 here. Systems with less favorable conditions, and more gradual changes to irradiation should produce weaker variability, so based on the hydrodynamic model this constrains variation in $\dot{M}_s$. See Ch. 7 for details on the results and methods.

Chapter 4

Implementing this physics in a single, simplified model

The many mechanisms of Ch. 3, and quite likely their interactions, may be responsible for the longterm variability posed by the data in Ch.2. This motivates building a numerical model that can include these mechanisms operating together, even at a simplified level. This still sets fairly harsh requirements: it must cover the full extent of the disk, from X-ray generation to input conditions, and it must somehow cope with draining timescales at the innermost disk while addressing behaviors spanning hundreds of days. Addressing two-phase accretion introduces another accretion flow with a stiff coupling term, and an innermost timescale orders of magnitude smaller than the disk's.

The timescale problem is the most severe, and demands using techniques like adaptive time-stepping, or an implicit method which I use here. I also make the following major assumptions

(i) I assume local thermal equilbrium (LTE)

(ii) I drop radial energy advection is small in the standard disk

(iii) I assume ions in the halo maintain virial temperatures

(iv) I approximate rotational velocity as Keplerian

(v) I assume vertical hydrostatic equilibrium

(vi) I neglect self-gravity

While assuming LTE and negligible radial advection of energy does simplify the transport problem, my primary motivation is practical pre-tabulation of disk properties to address so many possible models. E.g. there is no fundamental obstacle to including an arbitrary heating/cooling term in the tabulation to associate with advection effects, but it adds another dimension to the table.

Negligible self-gravity, vertical hydrostatic equilibrium describe the flow quite well, as does Keplerian rotational velocity for most of the disk (FKR02). For a draining[1] halo flow the assumption of Keplerian rotational velocity is not very good as the flow has virial temperature so that:

$$\frac{v_{\mathrm{R}}}{v_{\mathrm{K}}} \approx \frac{\nu}{R v_{\mathrm{K}}} \approx \alpha \left(\frac{c_{\mathrm{s}}}{v_{\mathrm{K}}}\right)^2 \lesssim \alpha \tag{4.1}$$

The general, vertically-averaged, time-dependent conservation equations for mass, angular momentum, and energy in an accretion disk in terms of: horizontal radius, R, local scaleheight, H, radial velocity, v_R, specific angular momentum, l, specific internal energy and enthalpy, e and h_e, net mass source per area, $\dot{\Sigma}$, radiation and other (e.g. buoyancy) energy

[1] i.e.: this isn't the drastically sub-Keplerian flow of the Chakrabarti & Titarchuk (1995) model

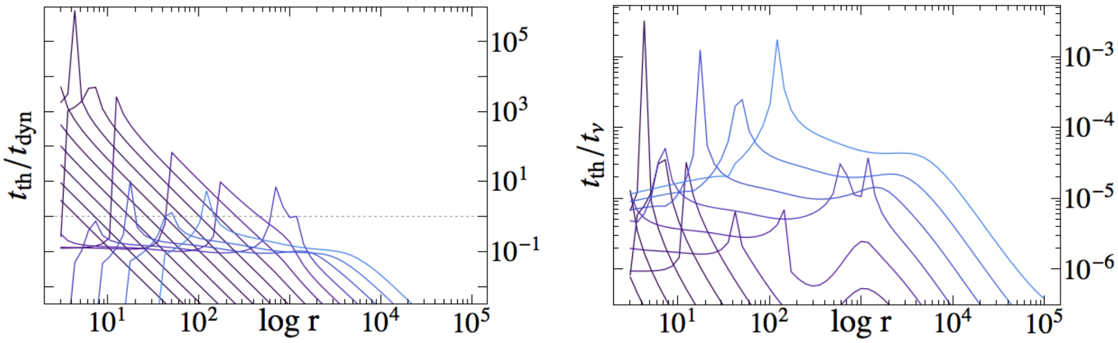

Figure 4.1: Left and right panels respectively show the ratio of thermal to dynamic and viscous timescales for an example PBα model, taking the highest temperature solution wherever it branches. Curves of higher surface density run from dark purple to light blue, and jumps (spikes) occur near cold-hot transitions. The viscous timescale surpasses the thermal and dynamical ones everywhere, but at low densities and large radii, t_Ω exceeds the thermal timescale.

fluxes F^-, and viscous stress tensor τ, read:

$$\partial_t \Sigma = -\frac{1}{2\pi R}\partial_R \dot{M} + \dot{\Sigma}_S \tag{4.2}$$

$$\partial_t\left(\Sigma l\right) = -\frac{1}{2\pi R}\partial_R(\dot{M}l) + \frac{1}{2\pi R}\partial_R\left(R \cdot 2\pi R 2H\tau_{R\phi}\right) + 4\pi R \cdot l\partial_R \dot{M}_w \tag{4.3}$$

$$\partial_t\left(\Sigma e\right) = \left\{-\frac{1}{2\pi R}\partial_R\left(\dot{M}h_e\right)\right\} + \left\{2H \cdot R\tau_{R\phi}\frac{d\Omega}{dR} + 2(F^-_{\rm rad} + F^-_{\rm etc})\right\} + e\dot{\Sigma}_S \tag{4.4}$$

where the assumption of radial centrifugal and pressure balance is also used, and the wind is 100% efficient at removing angular momentum here (see e.g. Knigge 1999 for a generalization). The left of the terms in braces in eqn.(4.4) represents the contribution of advection and pressure work and is dropped except in the case of the slim disk and halo flow where it is included by prescription (see below). Because the analytical EC models assume that the electron thermal conduction flux is deposited in a radiative layer between corona and disk, I do not include residual heating as MP07 did with their alternate EC model.

As usual, I take

$$\tau_{R\phi} = \alpha H p_{\mathrm{X}} \frac{\partial \ln \Omega}{\partial \ln R}, \tag{4.5}$$

where p_{X} may be gas or total pressure, and α may now depend on other variables[2].

I label the grid such that cell midpoints are tagged by index m, and sit between faces tagged f and $f+1$, A is the annular area of a given cell, and M the total disk/corona mass in that cell. Letting variables $\dot{M}_x$ stand for radial disk or corona mass fluxes; $\dot{M}_z$ for EC mass exchange taken such that evaporation is positive; $\dot{M}_{wx}$ for wind losses, and $\dot{M}_{sx}$ for other sources or sinks, then the discretized form of eqn.(4.2) for both flows are:

$$\partial_t M_{d,m} = \dot{M}_{d,f} - \dot{M}_{d,f+1} - \dot{M}_{z,m} - \dot{M}_{wd,m} + \dot{M}_{sd,m} \tag{4.6a}$$

$$\partial_t M_{c,m} = \dot{M}_{c,f} - \dot{M}_{c,f+1} + \dot{M}_{z,m} - \dot{M}_{wc,m} + \dot{M}_{sc,m} \tag{4.6b}$$

Wind losses present some ambiguity: does one remove mass directly from the disk, or only after any accreting corona is exhausted, or some fraction from each? The typical domain of substantial evaporation-produced corona is exclusive to strong Compton-heated winds so in this case I subtract wind directly from the disk by default. For strong winds at smaller radii, though, the matter becomes more important, but strong enough outflows should preclude an independently accreting corona so by default I will also subtract magnetically-driven wind from the disk or note otherwise.

For either flow the discretized flux at a face depends on the differential of torques,

$$G = 2\pi R^3 \nu \Sigma \partial_R \Omega, \tag{4.7}$$

as well any effective wind torque via:

$$\dot{M}_f \partial_R l_m = \partial_R G_m + l_f \partial_R \dot{M}_w. \tag{4.8}$$

[2] Abramowicz et al. (1996) also argues for replacing the radial shear index with the ratio of shear to vorticity index in agreement with Nauman & Blackman (2014). This doubles the strain in the strict Keplerian approximation and has larger impact for non-Keplerian flow

The simplest discretization is then:

$$\dot{M}_f = \left([G]_{m-1}^{m} + l_f \left[\dot{M}_w \right]_{m-1}^{m} \right) / \, [l]_{m-1}^{m} \tag{4.9}$$

while further choosing to discretize

$$[l]_{m-1}^{m} \rightarrow \left(\frac{\partial \ln l}{\partial \ln R} \right) R_f \Delta \ln R \tag{4.10}$$

yields second-order accuracy for a logarithmic grid and Keplerian flow (Krumholz & Forbes, 2014).

For the implicit method I will then split the flux terms $\dot{M}_f = \dot{M}_f^+ + \dot{M}_f^-$:

$$\dot{M}_f^{\pm} = \left\{ \begin{matrix} (G_m + l_f \dot{M}_{w,m}) / \, [l]_{m-1}^{m} \\ -(G_{m-1} + l_f \dot{M}_{w,m-1}) / \, [l]_{m-1}^{m} \end{matrix} \right\} \tag{4.11}$$

4.1 Constructing the overall implicit scheme

The implicit scheme starts with Taylor-expanding the flow equations

$$\begin{aligned} \frac{\Delta M_{d,m}}{\Delta t} = & \left[\dot{M}_{d,f} - \dot{M}_{d,f+1} - \dot{M}_z - \dot{M}_{wd} \right] + \dot{M}_{sd,m} - \left(\frac{\partial \dot{M}_z}{\partial M_c} \right) \Delta M_{c,m} - \left(\frac{\partial \dot{M}_z}{\partial M_d} \right) \Delta M_{d,m} \\ & + \left(\frac{\partial \dot{M}_{d,f}^{+}}{\partial M_{d,m}} - \frac{\partial \dot{M}_{d,f+1}^{-}}{\partial M_{d,m}} \right) \Delta M_{d,m} + \left(\frac{\partial \dot{M}_{d,f}^{-}}{\partial M_{d,m-1}} \right) \Delta M_{d,m-1} - \left(\frac{\partial \dot{M}_{d,f+1}^{+}}{\partial M_{d,m+1}} \right) \Delta M_{d,m+1} \end{aligned} \tag{4.12}$$

$$\begin{aligned} \frac{\Delta M_{c,m}}{\Delta t} = & \left[\dot{M}_{c,f} - \dot{M}_{c,f+1} + \dot{M}_z - \dot{M}_{wc} \right] + \dot{M}_{sc,m} + \left(\frac{\partial \dot{M}_z}{\partial M_c} \Delta M_{c,m} + \frac{\partial \dot{M}_z}{\partial M_d} \right) \Delta M_{d,m} \\ & + \left(\frac{\partial \dot{M}_{c,f}^{+}}{\partial M_{c,m}} - \frac{\partial \dot{M}_{c,f+1}^{-}}{\partial M_{c,m}} \right) \Delta M_{c,m} + \left(\frac{\partial \dot{M}_{c,f}^{-}}{\partial M_{c,m-1}} \right) \Delta M_{c,m-1} - \left(\frac{\partial \dot{M}_{c,f+1}^{+}}{\partial M_{c,m+1}} \right) \Delta M_{c,m+1} \end{aligned} \tag{4.13}$$

which includes the original zeroth-order fluxes in square brackets, pure source terms, and corrections that involve the changes in local and neighboring disk and corona masses being sought.

I arrange these into a tri-diagonal matrix in terms of 2×2 sub-matrices, and 2×1 vectors of the mass differences $\Delta \mathbf{M}_m$ and combined source terms $\mathbf{S}_m$:

$$\begin{bmatrix} ... & & & \\ & D_{m-1} & U_{m-1} & \\ & L_m & D_m & U_m \\ & & L_{m+1} & D_{m+1} \\ & & & ... \end{bmatrix} \begin{bmatrix} ... \\ \Delta \mathbf{M}_{m-1} \\ \Delta \mathbf{M}_m \\ \Delta \mathbf{M}_{m+1} \\ ... \end{bmatrix} = - \begin{bmatrix} ... \\ \mathbf{S}_{m-1} \\ \mathbf{S}_m \\ \mathbf{S}_{m+1} \\ ... \end{bmatrix} \tag{4.14}$$

which can then be solved by the Thomas algorithm (e.g. Ch.5 in *Numerical Methods of Astrophysics*). To be absolutely clear, I record the sub-matrices below

$$D_m = \begin{bmatrix} \left(\frac{\partial \dot{M}^+_{d,f}}{\partial M_{d,m}} - \frac{\partial \dot{M}^-_{d,f+1}}{\partial M_{d,m}} \right) - \frac{\partial \dot{M}_z}{\partial M_d} - \frac{1}{\Delta t} & -\frac{\partial \dot{M}_z}{\partial M_c} \\ +\frac{\partial \dot{M}_z}{\partial M_d} & \left(\frac{\partial \dot{M}^+_{c,f}}{\partial M_{c,m}} - \frac{\partial \dot{M}^-_{c,f+1}}{\partial M_{c,m}} \right) + \frac{\partial \dot{M}_z}{\partial M_c} - \frac{1}{\Delta t} \end{bmatrix} \tag{4.15}$$

$$L_m = \begin{bmatrix} +\frac{\partial \dot{M}^-_{d,f}}{\partial M_{d,m-1}} & 0 \\ 0 & +\frac{\partial \dot{M}^-_{c,f}}{\partial M_{c,m-1}} \end{bmatrix} \tag{4.16}$$

$$U_m = \begin{bmatrix} -\frac{\partial \dot{M}^+_{d,f+1}}{\partial M_{d,m+1}} & 0 \\ 0 & -\frac{\partial \dot{M}^+_{c,f+1}}{\partial M_{c,m+1}} \end{bmatrix} \tag{4.17}$$

Regarding flux derivatives - for fluxes in R, while prescribing or tabulating the thermodynamics of a zone I can also compute $\Gamma_d \equiv \partial \ln G_d / \partial \ln \Sigma_d$ and thus estimate

$$\frac{\partial G_d}{\partial M_d} = \frac{\partial G_d}{\partial A \Sigma_d} = \{\Gamma_d\}_{\text{tab}} \frac{G_d}{\Sigma_d} \tag{4.18}$$

meanwhile for a nearly virial ADAF-type corona flow,

$$\frac{\partial G_c}{\partial M_c} = \Gamma_c \frac{G_c}{\Sigma_c} \approx \frac{G_c}{\Sigma_c} \tag{4.19}$$

For the term associated with the basic wind model, $\dot{M}_{mw} = f_{\text{w}} \rho c_s / \beta^{1/2}$ giving

$$\frac{\partial \dot{M}_{wd}}{\partial M_d} \approx \frac{\Omega f_{\text{w}}}{A \beta^{1/2}} \tag{4.20}$$

For tabulated evaporation-condensation fluxes, the tabulation of $\dot{M}_z$ is done in terms of $\log(r) \times \log(n_c) \times \log(T_{ds})$ so I can use

$$\frac{\partial \dot{M}_z}{\partial M_c} = \left[\frac{\Delta \dot{M}_z}{\Delta \log n_c}\right] \frac{1}{M_c \ln(10)} \frac{\partial \ln n_c}{\partial \ln M_c} = \left[\frac{\Delta \dot{M}_z}{\Delta \log n_c}\right] \frac{1}{M_c \ln(10)} \tag{4.21}$$

$$\frac{\partial \dot{M}_z}{\partial M_d} = \left[\frac{\Delta \dot{M}_z}{\Delta \log T_{ds}}\right] \frac{1}{M_d \ln(10)} \frac{\partial \ln T_{ds}}{\partial \ln \Sigma_d} \tag{4.22}$$

where the square-bracketed terms are found by differencing table entries if $\dot{M}_z$ is tabulated, and $\partial \ln T_{ds}/\partial \ln \Sigma_d$ (normally 1/4) may also be tabulated for more complicated disk thermodynamics (like irradiation, the advective branch, etc.).

4.2 Tabulating disk thermodynamic (equilibrium) properties

The disk physics can be handled either via purely analytical prescriptions that involve simplifying and patching together physics (i.e. opacity, possibly α, etc.), or by tabulating solutions for more detailed physics beforehand and performing interpolations in the code which has its own disadvantages. For my purposes, the latter eventually proved essential, so I will limit my description to the procedure for tabulating disk thermodynamics.

Defining $\mathcal{R}(\Sigma_d, T_{dm}, ...)$ as the ratio of cooling to heating for a given annulus, thermal equilibrium is then wherever $\mathcal{R}(\Sigma_d, T_{dm}, ...) = 1$. I can take the implicit derivative to find

$$\frac{d\Sigma_d}{dT_{dm}} = \frac{-\partial \mathcal{R}/\partial T_{dm}}{\partial \mathcal{R}/\partial \Sigma_d}. \tag{4.23}$$

So long as I can reliably find one particular root, then I can numerically integrate eqn.(4.23) to find $\Sigma(T_{dm})$ [3] and numerically invert it as well (a branch at a time if necessary).

[3] and I want to work with $\Sigma(T_{dm})$ as it will be single valued

I consider $\mathcal{R}$'s of the general form:

$$\mathcal{R} = \left(\frac{2F^{-}_{\text{rad}} + (f_{\text{adv}} + f_{\text{mdw}})Q_{\text{vis}+}}{Q_{\text{vis}+} + Q_{\text{irr}+}} \right), \tag{4.24}$$

where $Q_{\text{vis}+}$ and $Q_{\text{irr}+}$ are viscous and irradiation heating, and I express advection and wind cooling as fractions f_{adv}, f_{mdw} of the viscous heating rate.

This advection term is one in Bjoernsson et al. (1996):

$$f_{\text{adv}} \approx \xi h^2 / \left(\left| \frac{d \ln \Omega}{d \ln R} \right| \frac{l}{1 - l_{\text{ISCO}}} \right) \tag{4.25}$$

where h is disk height over radius, and the parameter $\xi \approx 0.01 - 1$. Note: this term is specific to the thin disk and only becomes signficant for radiation-pressure-dominant conditions near the transition. I warn the reader that I do not fully incorporate a slim-disk solution by including this term. It serves to rescue RPI-susceptible models at high $\dot{M}_d$ with a stable branch that at least approximates a proper slim disk.

For the wind term and using the "upper-bound" model of Li & Begelman (2014), comparing estimates for the specific energy carried away per area by this wind, $\dot{m}_w c_s^2$, to the viscous dissipation in the column underneath it, $\alpha \rho c_s^2 \Omega H$, implies a scaling:

$$f_{\text{mdw}} = f_w \alpha^{-1} \beta^{-1} \tag{4.26}$$

parameterized by some strength $f_w \lesssim 1$. Scalings for models with more detailed prescriptions for the ratio of radial to azimuthal magnetic field can also be derived.

To avoid tabulating over reliably-uninteresting regions in $\log \Sigma_d$, I define a tilted density centered around the large-r Shakura-Sunyaev surface density profile:

$$\tilde{\Sigma}_d \equiv \Sigma_d / (\Sigma_0 r^{-3/4}) \tag{4.27}$$

to use instead. Although $\log T_{\text{irr}}$ appears to necessitate irregular gridding, an irradiation temperature of order 1–10 K has little practical effect so I simply use this as a lower bound and grid uniformly in log-space. Finally, many of the models depend on magnetic field which I roughly characterize by β_d. Thus, in general I tabulate solutions over $\log r \times \log \tilde{\Sigma}_d \times \log \beta_d \times \log T_{\rm irr}$.

Additional issues include how to identify particular branches, or how to avoid this problem altogether. In short, I found one way to label branches "morphologically" which fails for low resolution tables by finding more "branches" than the four the code can handle. Thus, I also built a backup method for table and code that just takes the coldest and hottest branches at each table coordinate to define a global "cold" and "hot" branch with a system of enforced hysteresis: whenever interpolation for each branch yields temperatures within some ϵ, the cell is in "neutral" and free to choose the branch based on smallest temperature difference, but once the branches become numerically distinct the code raises a flag forcing the cell to follow its current branch until the branches merge again.

4.3 Prescribing corrected evaporation-condensation rates

Again, both tabulation or analytical prescription are possible options: involved models of the transition layer motivate tabulation, but $\dot{M}_z$ is a signed quantity prone to possess steep gradients in flow variables favoring analytical solutions. I have implemented and experimented with each, but here I will describe an analytical prescription based on BF09 and LTMHM07 that corrects issues with temperature crossings, exceeding the energy budget, and the breakdown of Spitzer electron thermal conduction.

As a reminder, these first assume the disk-corona transition itself divides into three layers: the thinnest and lowest of these a radiative skin to the disk where most radiation takes place, while thermal electron conduction F_c trumps radiation in the layers above and transports heat from viscous dissipation in the corona downwards. The latter is subdivided based on the point where ions will begin efficiently transferring energy to the electrons determined by:

$$q_{\rm ie} > q_{\rm vis,i} + q_{\rm pdV} = (1 + (\beta_c + 1))\, \alpha_c n_c \left(\frac{k_{\rm B} T_{\rm ion}}{\mu_i} \right) \Omega \tag{4.28}$$

where n_c is corona number density, β_c the ratio of gas to magnetic pressure there, μ_i the mean molecular weight of ions, and $q_{\rm pdV}$ is compressive heating taken by MMH94 and following work to be $q_{\rm vis,i}(1 + \beta_c)$ [4]. I also approximate ion-electron energy exchange as they do

$$q_{\rm ie} \approx k_{ie} n_c^2 T_{\rm ion} T_e^{-3/2} \tag{4.29}$$

with $k_{ie} = 1.67 \times 10^{-16}$ erg/K$^{1/2}$cm^{3}s. This yields the coupling temperature

$$T_{\rm cpl} = \left((2\beta_c + 1) \frac{\mu_i}{k_{\rm B} \alpha_c n_c \Omega} \right)^{2/3} \tag{4.30}$$

Between the corona density scaleheight and this coupling temperature, the thermal electron conductive flux obeys

$$F_c = -\, \kappa_{ec}(T_e) \frac{dT_e}{dz} \tag{4.31}$$

$$\frac{dF_c}{dz} = -\, q_{\rm ie} \tag{4.32}$$

where κ_{ec} is the conduction coefficient. Most of the models assume Spitzer-Härm conduction

$$\kappa_{SH} = \kappa_0 T_e^{5/2} \approx 10^{-6} T_e^{5/2} \tag{4.33}$$

For steep enough temperature gradients though, electrons leave a given zone before colliding enough to settle on a local Maxwell-Boltzmann distribution as Spitzer-Härm assumes and instead electron thermal conduction saturates (a.k.a the free-streaming limit). Like Różańska (1999) I consider a form of κ_{ec} due to Balbus & McKee (1982):

$$\kappa_{SH} / \left(1 + |F_{c,SH}/F_{c,SC}|\right) \tag{4.34}$$

[4] Note if making direct comparisons that their "β" is the ratio of gas to *total* pressure

where $F_{c,SC}$ and $F_{c,SH}$ are the Spitzer-Härm and saturated fluxes. Then following Bale et al. (2013), I approximate the ratio of saturated over predicted Spitzer-Härm flux to the Knudsen number $\mathcal{K}_n$, and that to the ratio of electron mean-free path λ_e to the thermal conduction lengthscale of interest: $\Delta T_e/\nabla T_e$. Thus, in terms of local corona properties I define an effective conduction coefficient:

$$\kappa_{\text{eff}} \approx \kappa_0 \left(1 + \left(\frac{2200 T_{\text{em}}^2}{n_c H_c}\right)\right)^{-1} \tag{4.35}$$

where T_{em} refers to the electron temperature maximum somewhere near the top of the transition layer.

Combining equations (4.31) and (4.32), and integrating with the boundary condition $F_c \to 0$ in the corona gives

$$0 - F_c^2 = -k_{ie}\kappa_{\text{eff}} n_c^2 T_{\text{ion}} \left(T_{\text{em}}^2 - T_e^2\right) \tag{4.36}$$

and assuming it is reached at the corona scaleheight H_c:

$$\frac{H_c}{\sqrt{2}} - z_{cpl} \equiv z_m - z_{cpl} = \left(\frac{\kappa_0}{k_{ie} n_c^2 T_{\text{ion}}}\right)^{1/2} \int_{T_{\text{cpl}}}^{T_{\text{em}}} \frac{T_e^{5/2} dT_e}{\sqrt{T_{\text{em}}^2 - T_e^2}} \tag{4.37}$$

Defining $y = T_{\text{cpl}}/T_{\text{em}}$ one can write

$$\frac{H_c}{\sqrt{2}} \approx \left(\frac{\kappa_{\text{eff}}}{k_{ie} n_c^2 T_{\text{ion}}}\right)^{1/2} T_{\text{em}}^{5/2} \int_y^1 \frac{x^{5/2} dx}{\sqrt{1 - x^2}} \tag{4.38}$$

Here I correct a small error in MMH94 and descendants by restoring the full $5/2$ power to T_{em} on the right hand side. The first terms in series expansion of the integral on the right go like

$$\approx 0.71889 - 2y^{7/2}/7 \ldots \tag{4.39}$$

which BF09 approximate as $0.71889(1 - y)$ but taking $0.71889(1 - y^{5/2})$ proves both more accurate and convenient in deriving a new T_{em} for the Spitzer-Härm case:

$$\begin{aligned} T_{\text{em}}^{(\text{SH})} =& T_{\text{cpl}} \left(1 + \mathcal{F}\right)^{2/5}; \\ \mathcal{F} =& \frac{H_c}{0.71889\sqrt{2}} \left(\frac{k_{ie} n_c^2 T_{\text{ion}}}{\kappa_0}\right)^{1/2} T_{\text{cpl}}^{-5/2} \end{aligned} \tag{4.40}$$

Using the proper series expansion with the free-streaming $T_{\rm em}$ dependence in $\kappa_{\rm eff}$ does not yield a closed form solution. Taking the root numerically in `Mathematica` though, I can do so and find relatively evaporation at higher n_c (fig.4.2) except where $T_{\rm em}$ is limited by inverse-Compton cooling according to the prescription of LTMHM07.

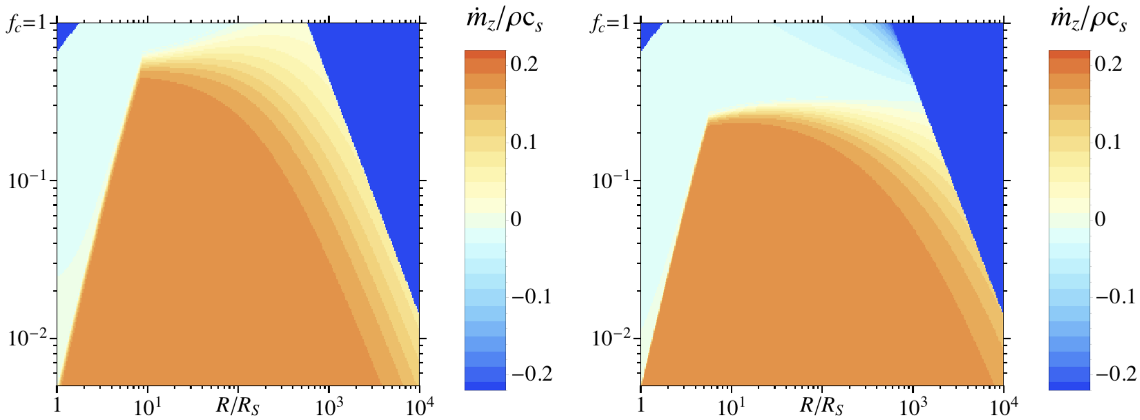

Figure 4.2: The panels show $\dot{m}_z$ scaled by $\rho_c c_{\rm sc}$ versus radius and corona density, again as a fraction of its value for an ADAF with $\dot{M}_c = \dot{M}_{\rm E}$. Both are for a standard $T_{\rm eff,d}$ profile with peak temperature 0.48keV and include the energy-budget limit (see text, and Fig. 4.4), but the one at left includes the free-streaming limit which leads to continued evaporation at higher n_c, but has little effect on direct inverse-Compton cooling of the corona at small r.

In LTMHM07, the authors treated the effects of inverse-Compton cooling $q_{\rm C}$ by finding the electron temperature $T_{\rm ec}$ below which electrons' inverse-Compton energy losses will be balanced by the ions heating them ($q_{\rm C} = q_{\rm ie}$), and restricting $T_{\rm em}$ to be less than $T_{\rm ec}$. I use the same, simple treatment, but note that the same authors updated this "Compton-or-conduction" approach to a sum of the two processes in Taam et al. (2008). For mildly-relativistic electrons, in a corona of low optical depth

$$q_{\rm C} \approx \frac{1}{2}\left(\frac{4k_{\rm B}T_e}{m_e c^2}\right) n_c \sigma_{\rm T} \cdot 4\sigma_{\rm SB} T_{\rm eff,d}^4 \tag{4.41}$$

and I find

$$T_{\rm ec} = 1.58 \times 10^8 \left(\frac{n_c T_{\rm ion}}{T_{\rm eff,d}^4} \right)^{2/5} \tag{4.42}$$

Thus, the ultimate $T_{\rm ec}$ used is the minimum of these limits. Under conditions more extreme perhaps than MMH94, LTMHM07, and BF09 imagined, further temperature crossings involving $T_{\rm cpl}$ are possible which ruin the underlying picture of the transition layer so I apply some additional rules (fig.4.3). First, the simplified estimate of $T_{\rm cpl}$ can cross $T_{\rm ion}$ which a more accurate $q_{\rm ie}$ clearly fixes, but this also serves as a useful indicator for when the corona should succumb to cooling and recondensation. Second, $T_{\rm cpl}$ may cross $T_{\rm ec}$ soon after $T_{\rm em}$ does, which implies that the disk can now effectively Compton cool the ions via the electrons, so in this case especially I consider rapid recondensation the most physical prescription. Finally, I note

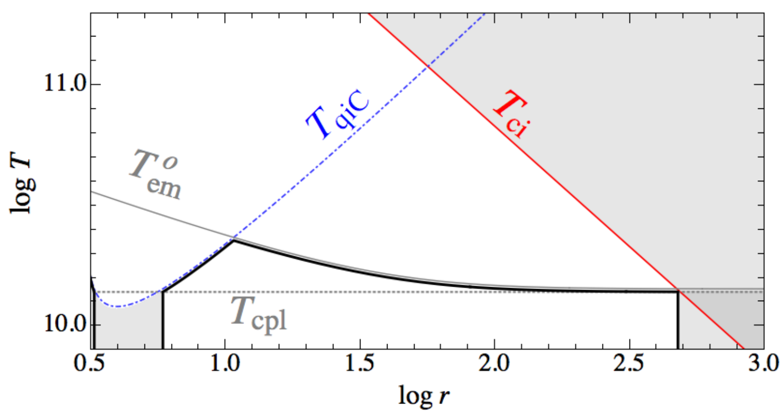

Figure 4.3: Example coronal ion ($T_{\rm ion}$), ion-electron coupling ($T_{\rm cpl}$), predicted peak electron ($T^0_{\rm em}$), and inverse-Compton-limited ($T_{\rm qiC}$) temperatures versus radius for a steady-state corona flow of $\dot{M}_c \approx 0.01 \dot{M}_{\rm E}$ and $\dot{M}_d \approx 0.3 \dot{M}_{\rm E}$ with inner disk temperatures steepened to exaggerate crossings. The black solid line indicates the final, maximum corona electron temperature allowed. Wherever it would cross $T_{\rm ion}$ or $T_{\rm cpl}$ (and plunges in the figure), the corona should cool and condense rapidly until there is no such crossing (or no corona).

that the "raw" evaporation rates predicted in previous models – with or without or saturated thermal conduction and other modifications – often convert cool disk to hot corona at a rate that requires energy input, i.e. $\dot{m}_z(c_{\rm sc}^2 - c_{\rm d^2}) \approx \dot{m}_z c_{\rm sc}^2$, far beyond the viscous-dissipation budget of $\alpha_c \rho_c c_{\rm sc}^3$ as shown in Fig.(4.4). Thus, after computing the raw predicted rates in their fashion, I

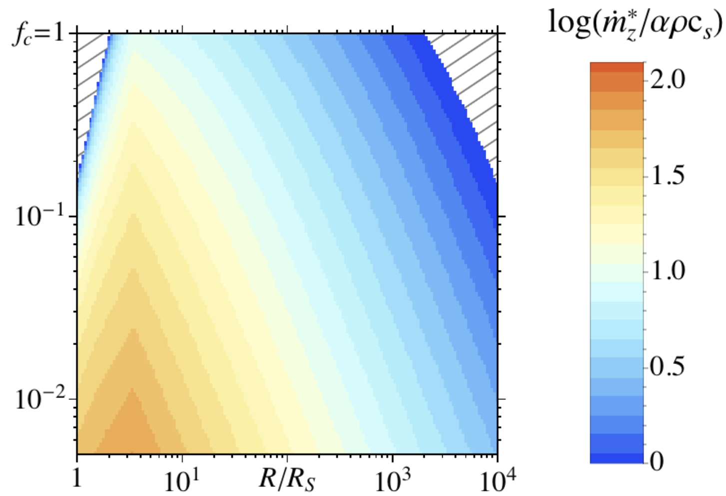

Figure 4.4: A plot of the "raw" predicted evaporation rate versus the rate set by the viscous-dissipation budget for a peak disk temperature of 0.4keV where axes are identical to Fig.(4.2). Hashing shows the domain of condensation.

enforce a limit on evaporation based on some fraction of this budget (e.g. 0.2). Besides plugging in a different $T_{\rm em}$, $\kappa_{\rm eff}$ for κ_0, and applying the limiter afterwards, the predictions for mass flux per unit area ($\dot{m}_z^{\rm raw}$) otherwise follow the same form as in BF09. Defining

$$\mathcal{C}_{EC} \equiv \frac{k_{ie}\kappa_{\rm eff}}{\pi}\left(\frac{\beta_c}{1+\beta_c}\frac{n_c T_{\rm cpl}}{F_c(T_{\rm cpl})}\right)^2 \tag{4.43}$$

where $\mathcal{C}_{EC}$ greater (less) than unity implies condensation (evaporation), and letting $\epsilon = T_{\rm cpl}/T_{\rm ion}$, they are:

$$\dot{m}_z^{\rm raw} = \left(\frac{2\beta_c}{8+5\beta_c}\frac{\mu m_p}{k_{\rm B}}\frac{F_c(T_{\rm cpl})}{T_{\rm ion}}\right)\begin{Bmatrix} \left(1-\frac{\epsilon}{2}-\left(\epsilon^2/4+(1-\epsilon)\mathcal{C}_{EC}\right)^{1/2}\right) & \mathcal{C}_{EC}<1 \\ \epsilon(1-\mathcal{C}_{EC}) & \mathcal{C}_{EC}>1 \end{Bmatrix} \tag{4.44}$$

To give a broader sense of the dependence, I plot EC rates for select peak disk temperatures and temperature profiles in Fig.(4.5).

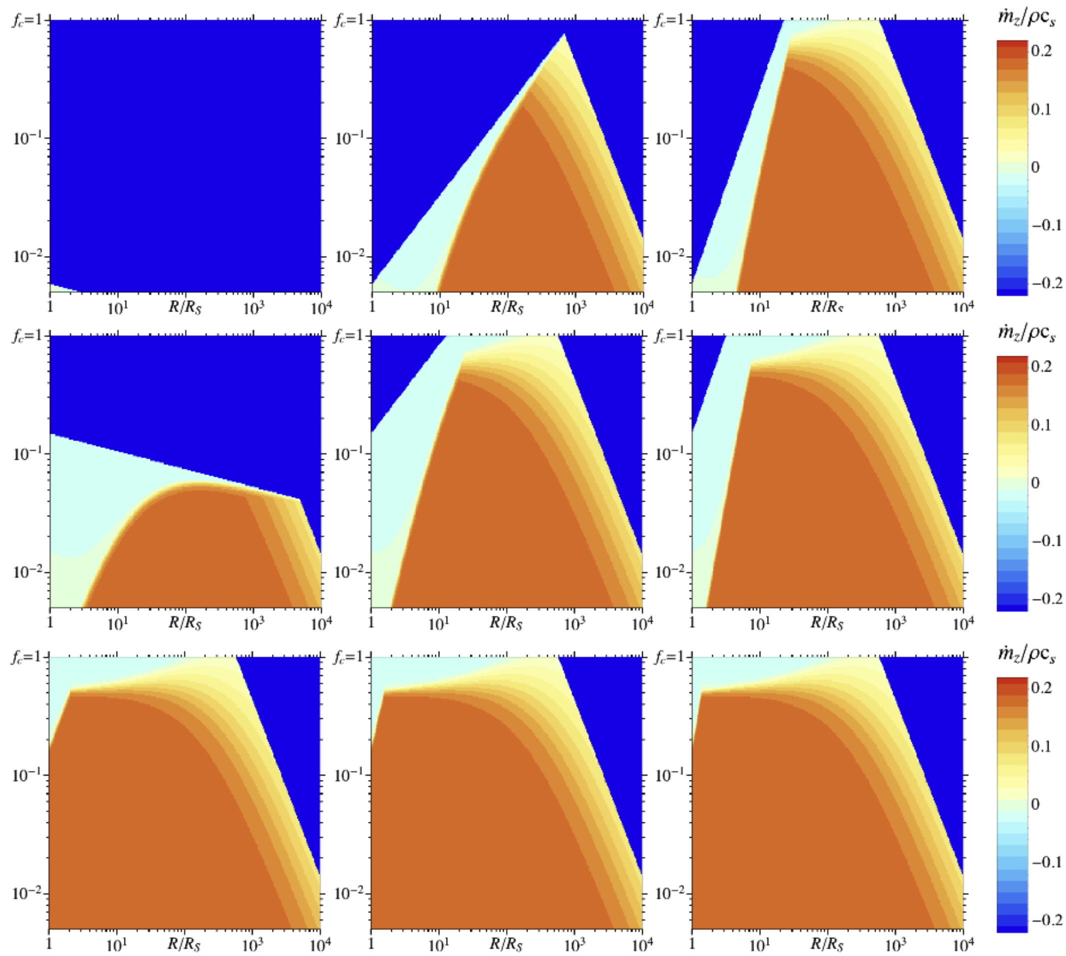

Figure 4.5: Similar to Fig.(4.2), but all panels are for saturated conduction. From bottom to top, $\dot{m}_z$ are plotted for peak disk temperatures of 0.3, 0.7, and 1.2 keV, and from left to right for radial power-law indices of -0.6, -0.75 (Shakura-Sunyaev) and -0.9.

4.4 A simple vertical magnetic flux transport module

To explore the evolution of net vertical magnetic flux at a late stage in the code, I treated the flux as a pollutant advected according to a simple single-donor-cell scheme:

$$\partial_t \Phi_{M,m} = [v_{\rm eff} B_z + S_{\Phi,m}] \tag{4.45}$$

where $v_{\rm eff}$ is the net advective/diffusive velocity, $S_{\Phi,m}$ is the sum of source terms, and the Courant condition for the flux evolution gets included in limits to the overall timestep. Both the Begelman & Armitage (2014) net-flux mechanism ("BANF") and convective-flux generation (Ch. 3.1; Hirose et al. 2014) sources take the form of a difference between a "desired" Φ^*_M and the current value divided by a relevant timescale (softened by $\Delta t_{\rm sim}$). For the BANF mechanism:

$$\begin{aligned} S_{\rm BANF} &= \frac{\Phi_M(\beta_{\rm min}) - \Phi_M(t_0)}{\Delta t_{\rm sim} + \Delta t_{\rm gen}}, \\ \Delta t_{\rm gen} &= (k_{\rm dyn}/\Omega)\,(\beta(t_0)/\beta_{\rm min})\,(N_{\rm BA}/f_{\rm esc}) \end{aligned} \tag{4.46}$$

in which $N_{\rm BA}$ is some prescribed maximum number of magnetic patches, $f_{\rm esc}$ is their fraction of patches escaping, and $k_{\rm dyn}/\Omega$ is the dynamo timescale ($k_{\rm dyn} \approx 100$). Begelman & Armitage (2014) note that $N_{\rm BA}/f_{\rm esc} \lesssim 100$ is necessary to build up significant net flux during quiescence.

For the convective generation of flux, I first compute an $\alpha^*(T)$ that generalizes the (asymmetric) jump from cold α_c to hot α_h around the PHII transition temperature as found by Hirose et al. (2014),

$$\alpha^*(T_{dm}) = \alpha(t_0) + \max\left[0, \frac{\alpha_h + \alpha_c - \alpha(t_0)}{1.80}\left(\tanh\left(\frac{\log T - 3.91}{0.05}\right) - \tanh\left(\frac{\log T - 3.48}{0.30}\right)\right)\right] \tag{4.47}$$

where $\alpha_h \approx 0.2$ and $\alpha_c \approx 0.01$ correspond to their specific results, and . I then convert this to a desired $\beta^*(\alpha^*)$, which implies β_d and thus Φ^*_M! To prevent the source term from reducing flux from an already outbursting (or heavily-threaded) annulus, I also manually forbid the term from decreasing flux:

$$S_{\text{conv}} = \frac{\Phi_M^* - \min\left(\Phi_M^*, \Phi_M(t_0)\right)}{\Delta t_{\text{sim}} + k_{\text{dyn}}/\Omega} \tag{4.48}$$

The source terms may be further softened via $(\Phi_M^* - \Phi_M) \to \min(\max(\Phi_M^* - \Phi_M, -1.2\Phi_M), +1.2\Phi_M)$ etc.

4.5 Quick tests and further caveats

The most basic check to perform on the code is a comparison with the Lynden-Bell & Pringle (1974) analytical solution for the evolution of a disk with viscosity linear in radius:

$$\nu = \nu_0(R/R_0) \tag{4.49}$$

and I follow the specific implementation of Krumholz & Forbes (2014). The analytical solution for surface density with time (t), in terms of scaled radius, $x = R/R_0$, and the viscous timescale there, $t_\nu^0 = R_0^2/3\nu_0$, reads

$$\Sigma_{\text{LPB}} = \left(\frac{\dot{M}_0}{3\pi\nu_0}\right) \frac{\exp(-x t_{\nu 0}/t)}{r(t/t_{\nu 0})^{3/2}} \tag{4.50}$$

The authors define boundary torques based on the solution plugged into eqn.(4.7)

$$G \to -R_0 \cdot (R\Omega) \cdot \dot{M}_0 \frac{\exp(-r t_{\nu 0}/t)}{x(t/t_{\nu 0})^{3/2}}, \tag{4.51}$$

they start the simulation at $t/t_{\nu 0} = 1$ for a nearly isothermal equation of state, and they cover a domain of 0.1-20R_0 with a maximum change of 10% permitted in cell quantities. I use a similar domain size, and these same initial and boundary conditions: applying the above torques in ghost cells just outside the solution domain so that they inform the $\dot{M}_d$ calculation at the inner- and outer-most cell walls. To test conditions similar to actual runs, I use ν_0 of 10^{14} cm^2/s in physical units, and $R_0 = 10^{2.5} R_{\text{S}}$ for a $10 M_\odot$ black hole. I also perform the test using a table with resolution of $\Delta \log r \approx 0.1$ and $\Delta log(\Sigma/\Sigma_0(R)) \approx 0.067$ – typical of other tables used.

I show the relative error for the case where viscosity is set directly in Fig.(4.6) at $t/t_{\nu 0}$=0.064, 1, 2, 3, and 4 to facilitate comparison with Krumholz & Forbes (2014). The error is larger, but roughly consistent with their backwards-Euler (i.e. fully-implicit) test case. The relative error in the tabulated-viscosity test differs from the set-viscosity by no more than a factor of 10^{-3} at $t/t_{\nu 0} = 4$. The test indicates that the method with the above tolerance, table

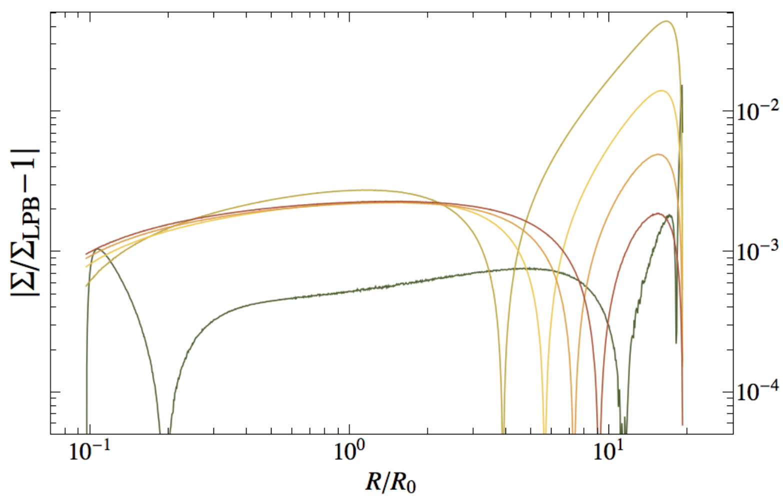

Figure 4.6: The relative error in the Lynden-Bell & Pringle test at $t/t_{\nu 0}$=0.064, 1, 2, 3, and 4, starting with the lowest, darkest green curve, peaking around $t/t_{\nu 0}$=1 (light green), and then running yellow-red.

resolution, etc. is sufficient for immediate, general tests to constrain the "model"-space, which can then be followed up with higher-resolution tables, lower tolerances, or more sophisticated simulations.

Chapter 5

Results since Cambier & Smith (2003)

For an assessment of EC, I refer to Ch.6 for further details on the original dilemma, and back to Ch. 4.3 for the detailed description of corrections and updates to the model which still do not explain how a corona flow could be responsible for $\dot{M}_d$-drops and the power-law emission in LMC X-3 without recondensing. Here (Ch.5.1), I will describe how this model also requires additional freedom to explain a range of disk truncation measurements for GX 339-4, and raise other points motivating the search for other mechanisms. In Ch. 5.2 I examine models where non-ideal MHD effects may cause quenching of the underlying MRI, including simple, general experiments on the consequences of another instability triggered at densities and temperatures intermediate to those where the PHII and RPI operate (Ch.5.2.2). These may alleviate the burden on EC for explaining $\dot{M}_d$-drops in persistent systems, but also tend to predict flares, and their relevancy to BHXRBs is not fully clear.

5.1 EC remains problematic

For the EC prescription updated here, as seen in Fig.(4.2), a strip of strong condensation remains at small radii where electron temperatures fall below the coupling temperature, but the problem of recondensation further outwards is alleviated. This reduces the domain over which additional physics must selectively suppress condensation at higher $\dot{M}_d$.

Over these radii, toroidal flux emerging from the disk preferentially at high $\dot{M}_d$ per the Galeev et al. (1979) picture could conceivably buoy up the settling corona. To roughly quantify this possibility, I can estimate the deceleration recondensing gas experiences over a local dynamical timescale due to the pressure gradient, $\nabla p_{\rm M}$, of a magnetic carpet via

$$\partial_t(\rho_c c_{\rm sc})t_\Omega \approx \nabla p_{\rm M} t_\Omega \approx \frac{p_{\rm M}}{H_d} t_\Omega \tag{5.1}$$

I can then write the recondensation flux as a factor, $f_{\rm cnd}$, times $\rho_c c_{\rm sc}$, define $f_{\rm GRV}$ as the fraction of emerging disk magnetic field, and ask when this fraction can be decelerated within t_Ω: $t_\Omega\, \partial_t(\rho_c c_{\rm sc}) > f_{\rm cnd}$, which leads to the condition:

$$\left(\frac{\Sigma_c}{\Sigma_d}\frac{c_{\rm sd}}{c_{\rm sc}}\frac{f_{\rm cnd}}{f_{\rm GRV}}\beta_d\right) < 1 \tag{5.2}$$

Values of $\Sigma_d \approx 10^4 {\rm g/cm^2}$, $\Sigma_c \approx 10^1 {\rm g/cm^2}$ and $c_{\rm sd}/c_{\rm sc} \approx 100$ appropriate to an inner disk at $0.1\dot{M}_{\rm E}$ with a corona fraction of 1%, and $\beta \approx 100$, $f_{\rm cnd} = 0.1$, and $f_{\rm GRV} = 1$, marginally satisfy the criterion. Of course, if this ad-hoc carpet exists simultaneously, it may be patchy enough to let gas recondense regardless, among other potential issues.

EC models also face difficulty in accounting for the observed variability in disk truncation. Fig.(5.1) provides an example using just the data points from Allured et al. (2013) for which disk temperature estimates were also available so that the corona density (expressed as $\dot{M}_c(R)/\dot{M}_{\rm E}$) can be estimated separately. Several of the observations indicate a wide range of inner disk truncation radii for comparable $\dot{M}_c$ which could correspond to the contours of nearly-constant $\dot{M}_c$ in Fig.(4.5) where evaporation rates jump. However, picking α_c so that this boundary goes through the points (its position is not sensitive to disk temperature over the range of values spanned by these points) leaves one measured disk radius well within a region where the EC model predicts the inner disk should readily evaporate (even for a seed corona $10^{-8}\dot{M}_{\rm E}$ at $200R_{\rm S}$).

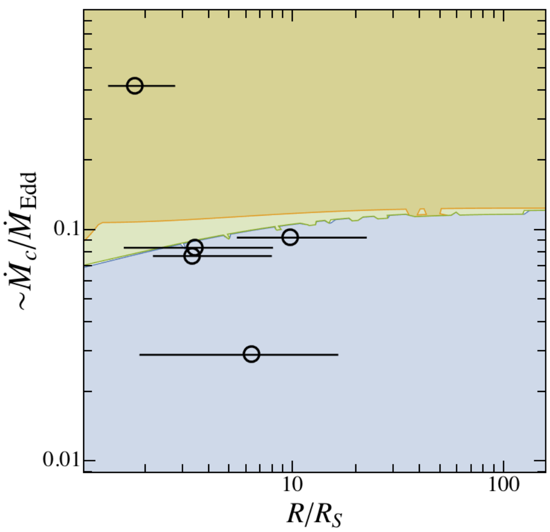

Figure 5.1: Here the points in Allured et al. (2013) have been plotted in terms of radius and corona Eddington fraction assuming a constant ADAF radiative efficiency of 0.1. The blue region shows where evaporation is strong for $T_d \approx 0$ while the thin green, and overlaid green-orange regions above it respectively show conditions for the corona to recondense at the highest and lowest T_d in the set of points with $\dot{M}_c/\dot{M}_{\rm E} \approx 0.1$. Resolving the variation in truncation radii at similar $\dot{M}_c$, "strands" a radius measurement (lowest point) where the model predicts evaporation.

Thus, substantial variation in thermal electron conduction, and/or α_c are required to resolve contradictions with the data in transient systems as well. Taam et al. (2008), working with the LTMHM07 model updated to include conduction-cooling in the Compton-cooling-dominant regime, also come to a similar conclusion. They make the important point that the evolving (and uncertain) geometry of truncated disk and corona can also account for some variation in Compton-cooling and the $\dot{M}_d$–T_d relation (as the corona irradiates the inner disk). However, they prefer variation in α_c based on the variation in luminosity and disk temperature in observations where Miller et al. (2006a) and Tomsick et al. (2008) find similar covering fractions (i.e. the angular extent of the inner disk relative to the corona).

Alternatively, the underlying picture of an independently dissipating, virialized accretion flow sandwiching a disk may break down. Instead, this picture may mimic the high altitude channel flows in Io & Suzuki (2014) and Fromang et al. (2013) in which dissipation is concentrated at high altitudes. I also note that models like Chakrabarti & Titarchuk (1995) where the halo beyond $\sim 10R_\mathrm{S}$ does not interact with the disk, and does not drain so much as fall, could circumvent this particular problem.

5.2 PBα and related models are intriguing

As noted, disk instabilities like the RPI and PHII drive cycles similar to the sawtooth wave in persistent BHXRBs with the exception of the flaring peak. Thus, a similar instability operating at intermediate radii and densities may work if it somehow dodges the flaring state, and permits canonical transient hysteresis cycles. Early modeling with a simplified version of the PBα model where the critical surface densities for transitions grew with radius indeed behaved like the other instabilities. However, the numerical simulations for dynamo quenching given some Reynolds' numbers input directly into the equations suggest a more complicated dependence on disk properties which changes the critical surface densities.

Given this ambiguity, I conducted additional simple experiments that explore a variety of general, arbitrary forms of branching in α to see what behaviors are possible, but find that it is difficult to obtain sawtooth variability on long timescales and avoid flares (Ch. 5.2.2). I then address their physical basis: I discuss how PBα might be reconciled with the domain of dynamo quenching found in simulations, and note how flux-dependent α may mimic the positive aspects of these models while avoiding their faults (Ch. 5.2.3).

5.2.1 Extending and scrutinizing PBα

As Fig.(5.2) shows, the original transition, computed using the more detailed opacity approximation and central-to-surface-temperature relation confirms that it will affect the disk at peak T_{ds} near 10^7K, and that in the full calculation the branches tend to rejoin at large R.

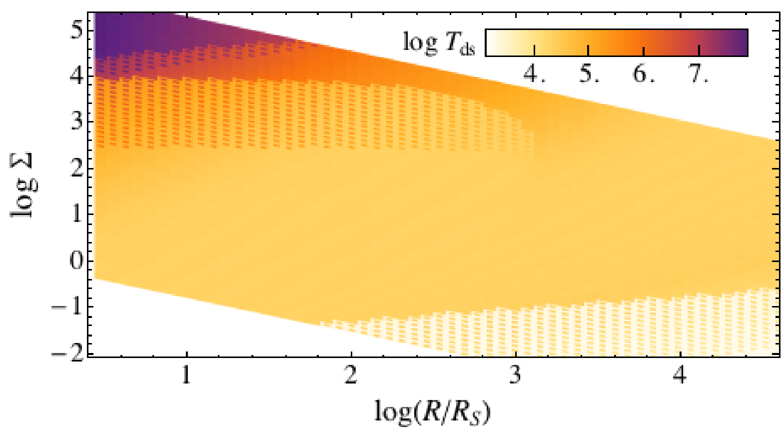

Figure 5.2: Plot shows heatmap of tabulated T_{ds} solution(s) in R and Σ_d (with $T_{\rm irr} = 0$) for the basic Potter & Balbus (2014) criterion. Regions where the solution is two-valued are indicated by plotting every other tile for the high branch (the "hatching"): the RPI causes such overlap in the upper-left corner, the PHII in the lower-right corner, and the PBα instability is behind the thick, intermediate overlapping zone.

However, trading the simple $\mathcal{P}_m < 1$ criterion for dynamo quenching with an approximation to the kind of fluid and magnetic Reynolds' numbers' dependence found by Lesur & Longaretti (2007), and Oishi & Mac Low (2011) renders the transition irrelevant. Based on the microscopic viscosity and diffusivity estimates in PB14, BHXRB accretion disks live in the far upper right corner of Fig.(5.3) which illustrates how I implement the $\mathcal{R}_h$- and $\mathcal{R}_m$-dependence. If the actual diffusivity were greater, or the critical $\mathcal{R}_m$ somehow larger, then quenching near the original PBα prediction becomes possible again. Fig.(5.4) shows that the transition only reappears at comparable Σ_d after $\mathcal{R}_m$ has been divided by $\sim 10^5$ (or the critical $\mathcal{R}_m$ raised this high).

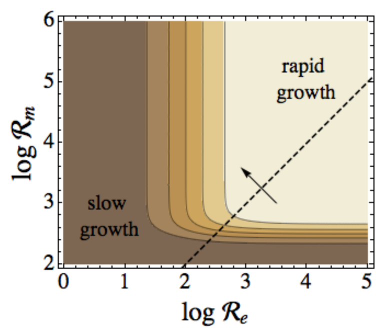

Figure 5.3: The plot shows the implementation of the α-"quenching" criterion in Lesur & Longaretti (2007) where α is 1 at high $\mathcal{R}_h$ & $\mathcal{R}_m$, and 0.001 where quenched in this particular example, and the contours trace steps of $\Delta \log \alpha = 0.5$. For comparison, the dashed line ($\mathcal{P}_m = 1$) and arrow shows the location and direction of the cold-to-hot transition according to the Potter & Balbus (2014) criterion.

While computing tables for different parameters, I made one using an incorrect opacity function, and ran a simulation with it which is remarkable for qualitatively imitating a range of BHXRB behavior: a fast-rise and exponential decay, followed by an outburst which quickly encountered the RPI followed by sawtooth $\dot{M}_d$ (fig.5.5). Among other effects, the reduced opacity effectively raises the transition $\mathcal{P}_m$ above unity (where radiative viscosity dominates Coulomb viscosity) so that α branches under more relevant disk conditions.

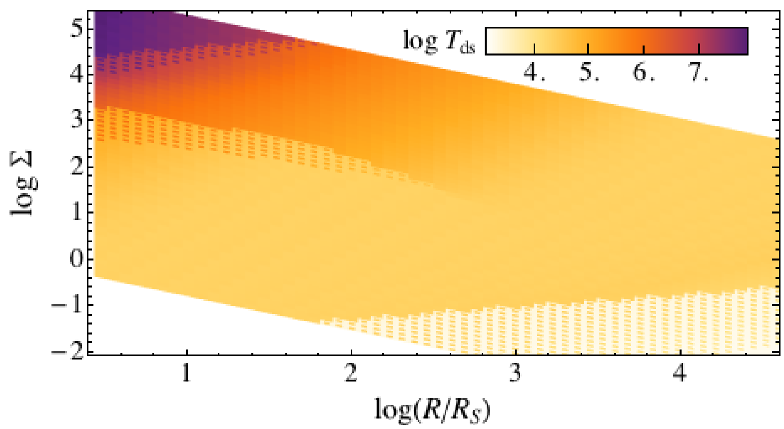

Figure 5.4: Similar to Fig.(5.2), but for the detailed dynamo dependence where the ratio of $\mathcal{R}_m$ to the cutoff value has been divided by $3{\times}10^5$.

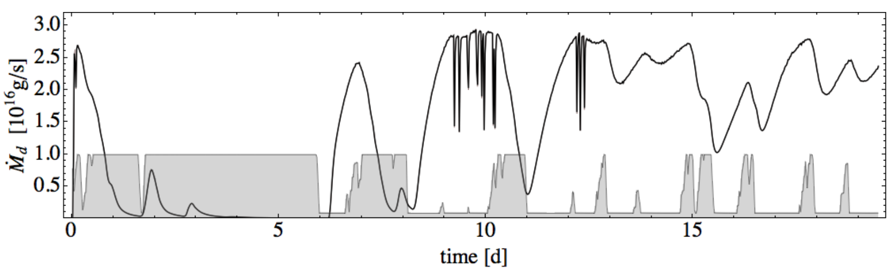

Figure 5.5: A run using the errant disk table (fig.5.6) where the solid curve tracks inner $\dot{M}_d$ and the gray filled curve tracks α averaged about $\approx 10^3 R_{\rm S}$ and suggestively flipped such that α_h is 0. Starting from the globally-high disk state, the disk decays with a few secondary outbursts, goes quiescent, but recovers and traces a persistent sawtooth pattern with sudden jagged dips indicating where it also reaches the slim disk state. Accretion rates and timescales are woefully small though.

5.2.2 Simple experiments exploring branch dynamics

Testing if the "errant" viscosity hints at a real solution motivated simple tests restoring more realistic disk physics by using the standard SSD solution, but introducing arbitrary branches in α to first see what behaviors are possible with them.

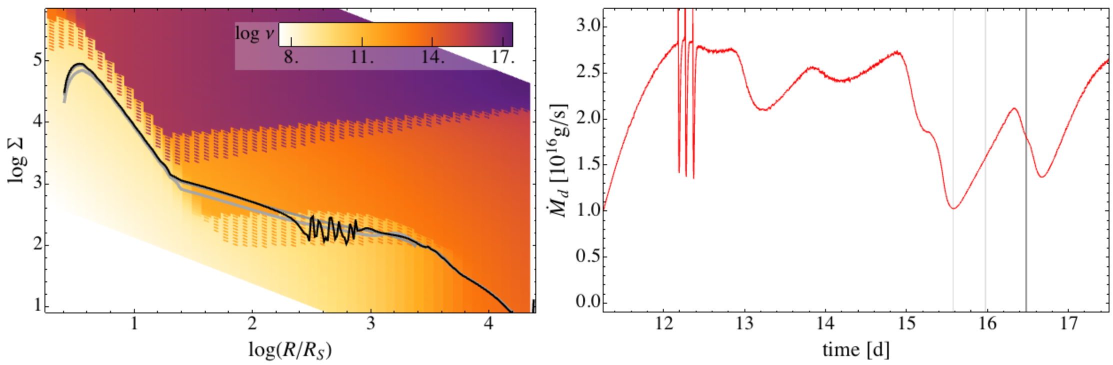

Figure 5.6: A heatmap of viscosity (left) in the errant table showing branch overlaps in the manner of Fig.(5.2) along with surface density profiles that run darker with time. The right panel shows a segment of the inner $\dot{M}_d(t)$ with gridlines showing times sampled for the Σ_d curve.

To focus on behavior near the threshold of instability, I chose mean supply rates appropriately, a larger initial disk mass to sweep over higher input rates as this excess mass drained away, and I injected a very conservative amount of variability: ∼10% drops every 8 days.

For reference, I include a case with a truncated, transition zone where the critical Σ_d for both the low-to-high and high-to-low increase with radius. Besides cycles of outbursts, it also shows fast, brief dips associated with jumps triggered in the transition region that will appear in later cases discussed below. In this case, the of the region means only a small, brief fast-drop-slow-recovery that doesn't lead to a catastrophic drop is possible.

Tilting the boundaries of the transition region to more closely follow tracks of constant $\dot{M}_d$ subdues, but does not eliminate, flares as shown in Fig.(5.8). Otherwise, it regularly generates the kind of $\dot{M}_d$-drops desired, but without quite so gradual a recovery. As Fig.(5.4) shows, such tilting is plausible if α drops sharply below a specific $\mathcal{R}_m$.

The sawteeth in the errant table can be replicated for more realistic opacities and accretion rates, but they are still too brief in the examples like Fig.(5.9) shown here. Although the drops are produced at radii with long viscous timescales, they are produced by fluctuations in

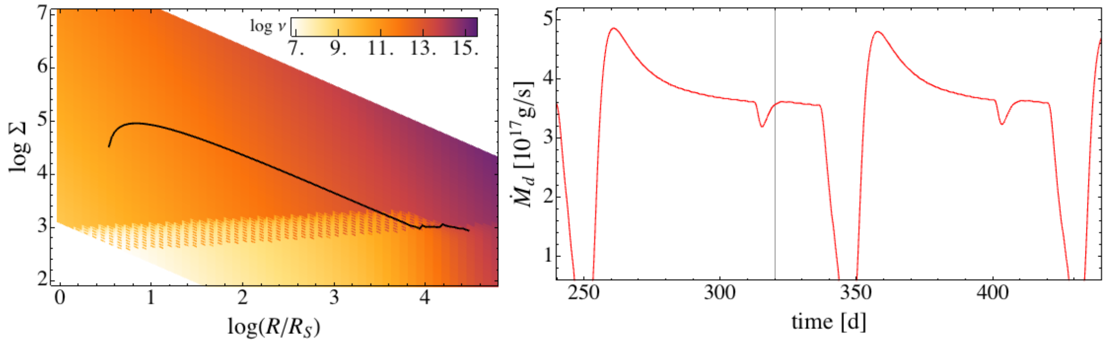

Figure 5.7: Like Fig.(5.6), the left panel shows the viscosity table and branches overlaid with Σ_d profiles for times indicated on lightcurve. A small portion of Σ_d dropped below the critical density, but exterior Σ_d remains just high enough to survive until the major decline later.

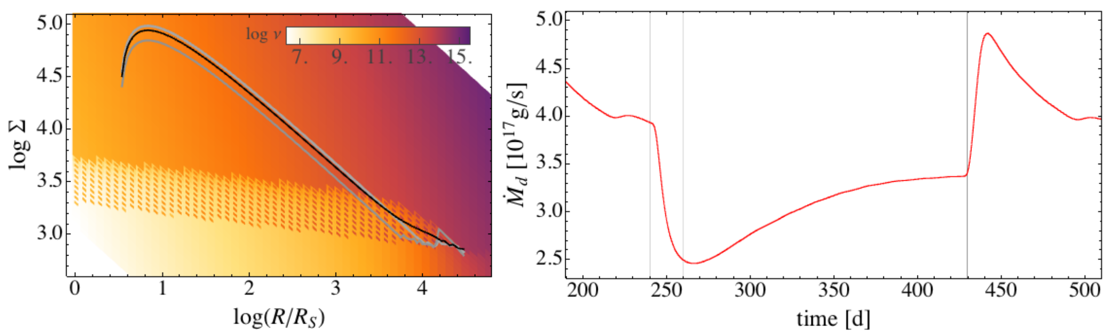

Figure 5.8: Like Fig.(5.7), but for a viscosity profile where the critical Σ_d increase with radius. The light-to-dark gray Σ_d curves show how a small drop in Σ_d at large radii triggers a rapid drop in $\dot{M}_d$ further inwards by crossing the hot-to-cold Σ_d.

Σ_d jumping rapidly between the transition surface densities. Greater separation in the transition surface densities could increase the sawtooth duration, but this also risks more complete drops and flares, and requires ever steeper dependencies in the mechanism underlying the transition. The mix of $\dot{M}$-behavior from the errant table at comparable timescales and magnitudes owes more to the decays in questions being decays of the inner versus full disk, but a simple, broad, truncated transition region growing with radius (fig.5.8) indicates that an intermediate branch

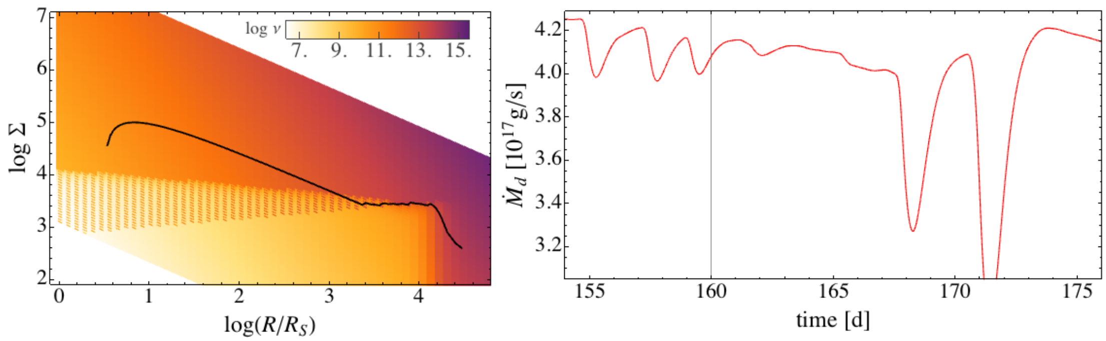

Figure 5.9: Like Fig.(5.7) but for a viscosity profile with mixed ascending/descending profiles for the critical high-to-low and low-to-high Σ_d which is conducive to rapid, low-amplitude sawtooth variability.

in α could at least amplify $\dot{M}$-drops in a way that helps explain observations.

5.2.3 What may explain or mimic these transitions?

As mentioned, a relevant PBα model can be reconciled to the Reynold's-numbers' dependence from simulations if magnetic diffusivity or the $\mathcal{R}_m$-cutoff for the dynamo is larger by factors $\gtrsim 10^5$, which diffusivity due to turbulence itself may accomplish. Based on Subramanian (1999), Schober et al. (2015) give a simple expression for the additional effective diffusivity

$$\eta_{\text{eff}} = \frac{1}{3}\tau(k)\frac{B^2/8\pi}{\rho} = \frac{4}{3}\tau(k)\frac{c_s^2}{\beta} \tag{5.3}$$

where the eddy-turnover time $\tau(k)$ varies with the wavenumber k, turbulence power-law index ϑ, driving scale k_L, and turbulent velocity v_t via

$$\tau(k) = \left(\frac{2\pi}{kv_t}\right)\left(\frac{k}{k_L}\right)^{\vartheta} \tag{5.4}$$

Taking $v_t \approx c_s$, $k_L \approx 2\pi/H_d$, and writing the scale of interest as a fraction f_H of the scaleheight gives $\tau(f_H) \approx f_H^{\vartheta+1}/\Omega$ and

$$\eta_{\text{eff}} \approx \frac{c_s^2}{\Omega}\frac{f_H^{\vartheta+1}}{\beta} \sim \frac{\nu_d}{\alpha}\frac{f_H^{\vartheta+1}}{\beta} \tag{5.5}$$

Comparing this to Spitzer resistivity for a temperature profile of

$$T_d = 1.0\mathrm{keV} \times (\dot{m}/0.2)^{1/4} r^{-3/4}$$

gives a ratio of

$$\frac{\eta_{\rm eff}}{\eta_{\rm S}} \approx 10^8 \left(\frac{M_{\rm bh}}{M_\odot}\right) \frac{\dot{m}^{5/8}}{r^{3/8}} f_H^{\vartheta+1} \tag{5.6}$$

i.e. quite substantial at large scales. For $\dot{m} = 0.10$, and $r = 10^3$ – where we are looking to preserve the PBα transition – and taking $\vartheta = 1/3$, the ratio stays above 10^5 down to $0.02H_d$. If the field is built up at much smaller scales, then this effect may not help much.

The pros and cons of the branching models also offer some hints for alternative mechanisms. In particular, advection of externally-supplied poloidal flux, enhancing accretion rate via boosted α and/or a MDW, might increase with outer accretion rate. A drop in accretion rate after a period of persistent accretion could then propagate quickly inwards. The accretion rate could then recover and build up flux without also crossing some density threshold that mandates a jump in accretion rate as in the α-branching models.

Chapter 6

Early work: Cambier & Smith (2013)

The Astrophysical Journal, 767:46 (13pp), 2013 April 10 doi:10.1088/0004-637X/767/1/46
© 2013. The American Astronomical Society. All rights reserved. Printed in the U.S.A.

PROTOTYPING NON-EQUILIBRIUM VISCOUS-TIMESCALE ACCRETION THEORY USING LMC X-3

Hal J. Cambier[1] and David M. Smith[1,2]
[1] Physics Department, University of California, Santa Cruz, CA 95064, USA
[2] Santa Cruz Institute for Particle Physics, University of California, Santa Cruz, CA 95064, USA
Received 2012 October 8; accepted 2013 February 21; published 2013 March 22

ABSTRACT

Explaining variability observed in the accretion flows of black hole X-ray binary systems remains challenging, especially concerning timescales less than, or comparable to, the viscous timescale but much larger than the inner orbital period despite decades of research identifying numerous relevant physical mechanisms. We take a simplified but broad approach to study several mechanisms likely relevant to patterns of variability observed in the persistently high-soft Roche-lobe overflow system LMC X-3. Based on simple estimates and upper bounds, we find that physics beyond varying disk/corona bifurcation at the disk edge, Compton-heated winds, modulation of total supply rate via irradiation of the companion, and the likely extent of the partial hydrogen ionization instability is needed to explain the degree, and especially the pattern, of variability in LMC X-3 largely due to viscous dampening. We then show how evaporation–condensation may resolve or compound the problem given the uncertainties associated with this complex mechanism and our current implementation. We briefly mention our plans to resolve the question, refine and extend our model, and alternatives we have not yet explored.

Key words: accretion, accretion disks – black hole physics – X-rays: binaries

1. INTRODUCTION

The X-ray spectrum of black hole X-ray binaries (BHXRBs) often shows variability in intensity and hardness on timescales of the order of the viscous timescale, but much larger than the innermost orbital period, including the well-known "q"-diagram hysteresis patterns traced by transient BHXRBs (Fender et al. 1999; Homan & Belloni 2005; Done et al. 2007; see Figure 1). The properties of such variability may also evolve over multiple viscous-timescale cycles. The high-soft (but sub-Eddington) and quiescent intensity–hardness limits are understood as manifestations of the thin-disk (Shakura & Sunyaev 1973) and radiatively inefficient advection-dominated accretion flow (ADAF; Narayan & Yi 1995a) accretion limits while states between are typically understood as some evolving combination of disk and ADAF flows (Chakrabarti & Titarchuk 1995; Esin et al. 1997; Nandi et al. 2012). Theoretical work has begun in this regime, but still cannot fully explain observations, especially regarding viscous timescales where detailed simulations prohibitively require many time steps and steady-state assumptions lose validity. This motivates us to develop theory in more detail starting with a system like LMC X-3, whose behavior is more constrained than that of the transients, but still exhibits substantial variability that is quantitatively challenging to explain.

In the current paradigm, transient BHXRBs are those systems where the outer disk reaches temperatures low enough to trigger the partial hydrogen ionization instability (PHII) in which accretion proceeds via cycles as viscosity alternately concentrates mass into rings and diffuses it inward (see Cannizzo 1998 and Lasota 2001 for a review). The part of the cycle where viscosity concentrates mass leads to the quiescent phase where any emission is presumably powered by some fraction of the flow that escapes the viscosity trap. Eventually, density increases enough to raise disk temperature above the transition point in viscosity, and the sudden jump in accretion rate leads to a rise in luminosity (often several orders of magnitude) while still in the hard state, followed by a softening of the spectrum at this same peak luminosity (the vertical and horizontal shifts by the dashed line in Figure 1). Jet emission is seen to shut off as the system enters the extreme high-soft state (Fender et al. 1999). Afterward, the system typically makes partial transitions in hardness (with small, erratic shifts in luminosity) on sub-viscous timescales and associated with intermittent jet emission on top of a secular decline in luminosity. Eventually the system transitions completely back to the hard state and then finishes fading back into quiescence.

There are a handful of persistent BHXRBs and black-hole-candidate X-ray binaries that do not execute such extreme quiescence–flaring cycles, and consistent with the transient paradigm they appear to avoid the PHII through an appropriate combination of disk size, luminosity (for disk irradiation), and mass supply rate (Coriat et al. 2012). Despite the label, these systems may still show significant variability and a variety of behaviors. Cygnus X-1 appears to slide between canonical high-soft and low-hard states with some scatter but no clear hysteresis (Smith et al. 2002, hereafter SHS02). The black hole candidates GRS 1758−258 and 1E 1740.7−2942 exhibit transient-like hysteresis but seldom reach the soft or quiescent limits (SHS02). LMC X-3 is typically bright in soft X-rays, but shows some hysteresis that circulates in the opposite direction to transients (see Figure 1), and does occasionally transition completely to the hard state (Wilms et al. 2001; Smale & Boyd 2012).

Accounting for irradiation of the outer disk, LMC X-3 accretes at rates high enough to usually avoid the ionization instability completely (Coriat et al. 2012), though the outer disk likely becomes susceptible for the deeper drops in disk luminosity, and almost certainly for rare, complete state transitions. Such high accretion rates are explained via Roche-lobe overflow (RLO); optical measurements of the companion's spectral type that take disk irradiation into account indicate B5IV (Soria et al. 2001) or B5V (Val-Baker et al. 2007) spectral type. Such a star will fill the Roche lobe for a 1.7-day orbit around a black hole with mass equal to the recent 9.5 $M_\odot$ lower bound (Val-Baker et al. 2007). Furthermore, Soria et al. (2001) have argued that feeding the observed X-ray luminosities via winds would lead to column densities far higher than measured. Although its distance precludes direct measurement or exclusion of radio jets, the jet quenching observed in transient BHXRBs

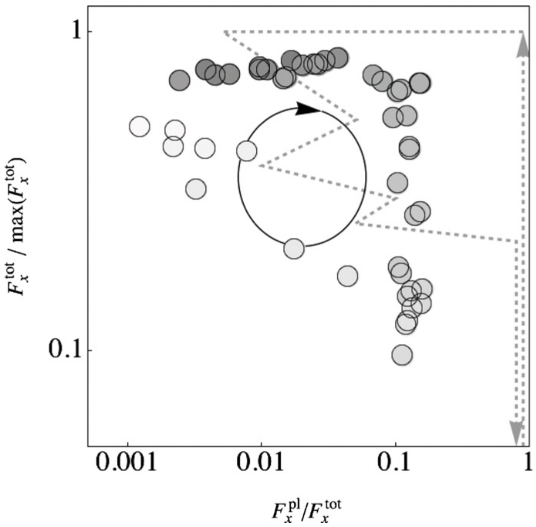

Figure 1. Shaded points show a typical spectral evolution cycle of LMC X-3 (first episode in Figure 5) with darker points corresponding to earlier observations, showing that it winds around in the opposite sense of typical transients' cycles shown schematically in the gray, dashed "q" or "turtle-head."

as they approach the high-soft state also suggests that LMC X-3 does not usually possess strong jets (Fender et al. 1998). Thus, if LMC X-3 shares similar variability mechanisms with transients, while being far less prone to the ionization instability and jet outflows, then LMC X-3 provides a more controlled setting to study such mechanisms. Below we list the major mechanisms we have considered so far in modeling LMC X-3, also summarized in Figure 2.

For RLO systems like LMC X-3, hard X-rays from the inner accretion disk can lead to supply-rate modulation (SRM) from the companion by inflating the companion's atmosphere to increase the density of gas at the L1 Lagrange point, as well as the area and pressure behind the nozzle (Lubow & Shu 1975; Meyer & Meyer-Hofmeister 1983). We elaborate in Section 3.1.

As the stream of gas from the companion dissipates energy and spirals onto the circularization radius, it may encounter the edge of the viscously spreading disk and from this point the flow can undergo disk–corona bifurcation (DCB) as some fraction can efficiently shock, cool, and join the disk while some fraction may stream past the thin disk edge and maintain its virial temperature (Hessman 1999; Armitage & Livio 1998).

Warping of the outer disk, whether driven by irradiation (Pringle 1992; Ogilvie & Dubus 2001; Foulkes et al. 2010) or a lift force (Montgomery & Martin 2010), can affect the accretion flow by changing the density profile that the disk presents to the RLO stream (Section 3.2), and by varying how the companion is exposed to or shadowed from inner disk X-rays. For LMC X-3 specifically, Ogilvie & Dubus (2001) and Foulkes et al. (2010) predict that the system is potentially unstable to irradiation-driven warping. Because the dominant long-term effects of warping are through bifurcation, and because we will lump them together as a boundary condition in our simulations, we combine our discussion of them into Section 3.2.

X-rays from the inner disk can Compton heat gas in the disk atmosphere and any corona at large radii above the local virial temperature thus driving a Compton-heated wind (CHW), discussed in Section 3.3, which is not only important for removing gas, but for removing hot corona that might otherwise help evaporate the disk or condense further inward (item (EC) below). As noted, for large enough disks and insufficient irradiation, a finite strip in the outer disk becomes susceptible to the PHII. For now, we do not treat it in any detail, but discuss the likely extent and manner of its effects in LMC X-3 in Section 3.4.

If the disk and corona are coupled thermally, then the disk and corona may exchange mass through evaporation and condensation (EC). Mayer & Pringle (2007, hereafter MP07) provide a thorough introduction and numerical treatment, and Liu et al. (2007, hereafter LTMHM07) and Meyer-Hofmeister et al. (2009) discuss more applications and provide the steady-state prescription for our modified method. Through EC, extant disks will tend to preserve the soft state down to lower luminosities via Compton-cooling-driven condensation, providing a natural explanation of why BHXRBs return to the hard state at lower luminosity and thus show hysteresis (Meyer-Hofmeister et al. 2009 focus on this aspect). We discuss other interesting effects possible in Section 3.5.

We will restrict our focus to an alpha-viscosity prescription for the disk. For the present work describing long-timescale variability over accretion rates typical to LMC X-3 where uncertainties regarding conventional mechanisms still loom large, we consider this perfectly adequate, but acknowledge the possibility of more intrinsic variability mechanisms (Section 5).

In Section 2 we review key features of LMC X-3's accretion behavior, summarize how we infer the innermost disk and corona/ADAF accretion rates from the X-ray data (additional details are provided in the Appendix), and critically examine the qualitatively simple bifurcation-only model in Smith et al. (2007, hereafter SDS07). The latter motivates Section 3, in which we furnish additional detail on the mechanisms as listed above, including estimated constraints on their effects and their

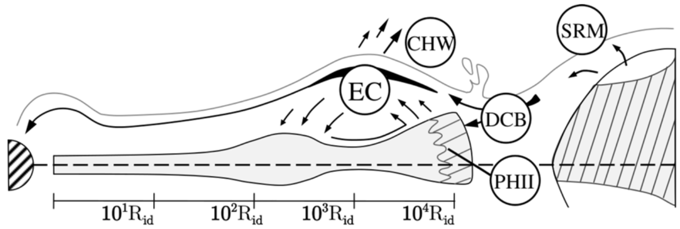

Figure 2. Primary mechanisms considered for driving long timescale changes observed in inner disk and corona accretion rates. These are supply-rate modulation (SRM; Section 3.1) from the companion, disk–corona bifurcation (DCB; Section 3.2) at the disk's edge, where disk warping may affect SRM and DCB, the partial hydrogen ionization instability (PHII; Section 3.4), Compton-heated winds (CHW; Section 3.3) at large radii, and evaporation and condensation (EC; Section 3.5) exchanging mass between disk and corona.

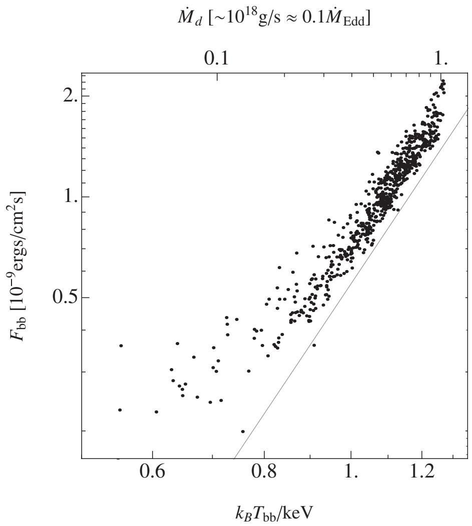

Figure 3. Fitted blackbody-component fluxes plotted against fitted temperature with a pure T^4 curve in faint gray for comparison.

current level of implementation in our modeling. In Section 4.1 we argue that a model including mechanisms besides EC cannot explain the data, but does best when given an unreasonably small disk radius and very large variations in corona–disk ratio at this boundary. We then show in Section 4.2 how EC may effectively recreate such seemingly ad hoc conditions, but how it may also imply behavior inconsistent with observations, including an extremely easily triggered "sympathetic" mode where the innermost disk and corona accretion rates rise and fall simultaneously. We briefly review the results and caveats of the current model, and state our current plans to resolve the question in Section 5.

2. LMC X-3 AS PROTOTYPE

Besides simplifying initial modeling as discussed above, LMC X-3 offers additional practical advantages. The *Rossi X-ray Timing Explorer* (*RXTE*) monitored LMC X-3 for over 16 years, and at least 5 of those include observations each about a kilosecond long taken roughly twice a week, thus providing a long, uninterrupted history of accretion with sufficient resolution at the timescales we seek to study. Also, the X-ray blackbody component, when present, tracks the Stefan–Boltzmann law fairly well (see Figure 3) indicating that inner disk geometry (i.e., truncation, warping) changes fairly little, and that the corona optical depth, τ_c, is small, simplifying estimates of the inner corona accretion rate, $\dot{\mathfrak{M}}_c$. Unless specified otherwise, we will use symbols $\dot{\mathfrak{M}}_d$ ($\dot{\mathfrak{M}}_c$) as shorthand for disk (corona) accretion rates at the inner disk radius, $R_{\rm id}$, and reserve the italic-face for general, local accretion rates $\dot{M}_d = \dot{M}_d(R, t)$, $\dot{M}_c = \dot{M}_c(R, t)$. Also, unless otherwise indicated, we will use the following system parameters: black hole mass, $M_{\rm bh} = 10\,M_\odot$, companion mass $M_* = 5\,M_\odot$, orbital period $P_{\rm sys} = 1.705$d, inclination $i = 67^{\rm o}$ and system distance, $d_{\rm sys} = 48$ kpc (van der Klis et al. 1985; Val-Baker et al. 2007), which also imply a circularization radius of $R_{\rm circ} = 2.7 \times 10^{11}$ cm.

We first fit individual *RXTE* spectra with a disk blackbody and a power law of fixed photon index, $\Gamma_{\rm pli} = 2.34$ (as in SDS07) with total absorption of fixed column density $n_{\rm H} = 3.8 \times 10^{20}$ cm^{-2} (Page et al. 2003), using the `wabs*simpl*diskbb` models in XSPEC (Arnaud 1996). To systematically identify transitions to the low-hard state we looked for cases where the first fitting gave reduced $\chi^2 > 1.1$, and refit these with a `wabs*(plaw)` model where the power-law index is not frozen. Reassuringly, spectra identified this way were fit better with fewer parameters, and are also typically preceded by obvious declines in the blackbody component (Figure 4).

For low τ_c one can describe the flows qualitatively by taking $\dot{\mathfrak{M}}_d(t) \sim T_{\rm bb}^4$ and $\dot{\mathfrak{M}}_c(t)$ proportional to the ratio of power-law to blackbody count fluxes (as in SDS07, though there the disk central temperature was confused with the effective temperature giving $\dot{\mathfrak{M}}_d(t) \sim T_{\rm bb}^{20/6}$). We obtain absolute normalization for $\dot{\mathfrak{M}}_d$ by fixing $R_{\rm id}$ and comparing observed and predicted fluxes in the high state where agreement should be best, while for $\dot{\mathfrak{M}}_c$, we obtain an estimate based on the simple τ_c and a typical ADAF solution, and check this against a more detailed calculation. We relegate the details to the Appendix to focus on a general description of accretion behavior (Figure 5).

From Figure 5, one can see that the $\dot{\mathfrak{M}}_c$ "turns on" in pulses (referring to the secular month-long features and not the jagged week-long sub-pulses) roughly a viscous timescale apart and slightly shorter in duration, and that these pulses tend to anticipate drops in $\dot{\mathfrak{M}}_d$. This trend was already noted in Smith et al. (2007) based on inferred qualitative accretion rates, and led the authors to posit a "bifurcation-only" model where a fairly constant total supply rate ($\dot{M}_s$) is split far from the black hole between non-interacting, quickly draining corona and slowly draining disk components. Our normalization estimates for $\dot{\mathfrak{M}}_c(t)$ suggest that for any given episode there is generally insufficient total mass in a $\dot{\mathfrak{M}}_c(t)$ pulse to explain the associated $\dot{\mathfrak{M}}_d$ drop. Even if our overall normalization is off, we still found that scaling $\dot{\mathfrak{M}}_c$ to conserve mass for one episode does not work very well for other episodes. This mass-conservation problem motivated considering mechanisms that can adjust the total supply rate, remove mass, and/or exchange it between disk and corona flows.

The secular evolution of the episodes on super-viscous timescales also lends itself to interpretation as multiple mechanisms acting on similar timescales effectively generating "beat-frequency" behaviors. The simple alternative of some mechanism(s) acting on super-viscous timescales coupled to viscous-timescale variability mechanisms lacks good candidates for the former. Nuclear evolution is too slow, we do not expect significant magnetic cycles from a companion with a radiative outer envelope (but keep the possibility in mind regarding other systems), and the inferred mass ratio in LMC X-3 is too high for slowly growing tidal resonances to be significant (Frank et al. 2002). Furthermore, based on the observed inclination, the warps would have to reach heights of 30$^{\rm o}$ relative to the orbital plane, and survive the severe drops in $\dot{\mathfrak{M}}_d$, to exhibit precession effects if irradiation-driven, which poses difficulties if LMC X-3 is only marginally unstable to irradiation-driven warping as Ogilvie & Dubus (2001) suggest.

The disk component in LMC X-3 tends to fall and recover more rapidly for larger drops than for shallow drops, a trend quantified in SDS07 and recently over an expanded data set in Smale & Boyd (2012). This aspect is qualitatively consistent with a bifurcation-only model given sufficient variation in the

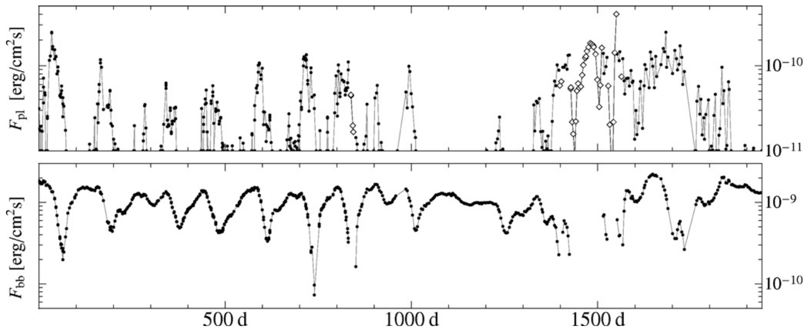

Figure 4. Fitted power-law (top panel) and blackbody (bottom panel) components of LMC X-3's X-ray flux since 53436.1 MJD. Diamond points in the top panel mark observations categorized as the pure hard state by the criteria in Section 2.

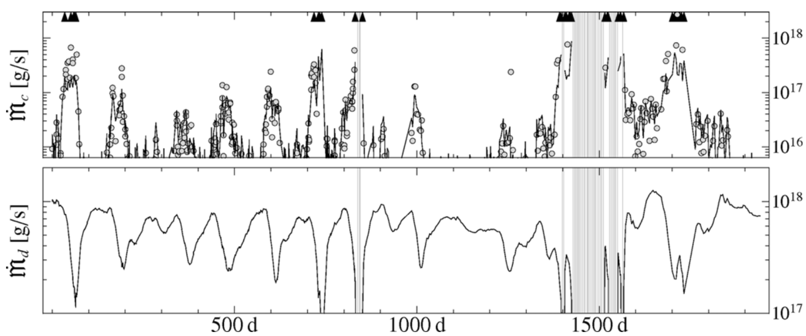

Figure 5. Inferred accretion history since 53436.1 MJD, barring times LMC X-3 was observed in the low-hard state (gray vertical lines) where inferring accretion rates is more ambiguous. Note that the vertical labels refer to inner accretion rates here. In the top panel, solid trace shows simple, direct estimate of $\dot{\mathfrak{M}}_c$ as well as results (points) of a more detailed method and arrowheads indicate points where the detailed method required abnormally high $\dot{\mathfrak{M}}_c$ (see the Appendix). Overall, one can see a trend for $\dot{\mathfrak{M}}_c$ to pulse "on" quasi-periodically and anticipate episodic drops in $\dot{\mathfrak{M}}_d$.

amplitude and duration of a drop at the outer edge—sensitivity to duration for a single input amplitude can be seen in Figures 7 and 8 of Zdziarski et al. (2009). However, using their analytical machinery, with and without crude representation of SRM and outflow effects, we will later show that rough quantitative agreement with observations of LMC X-3 requires inputs that are extremely unlikely without additional physics (Section 4.1). An interesting exception to the usual trend of $\dot{\mathfrak{M}}_c$ pulses heralding steep $\dot{\mathfrak{M}}_d$ drops is the small drop in $\dot{\mathfrak{M}}_d$ at 1100 d into Figure 5 not associated with any $\dot{\mathfrak{M}}_c$ pulse above the typical noise level.

Inferring accretion rates in the absence of the disk component introduces additional parameters and uncertainties, but we wish to make a few relevant observations while we work on a more definitive analysis of the hard state. The disk component drops and recovers on timescales of days in transitions into and out of the hard state, and tends to return more quickly than it decays when LMC X-3 is at its "hardest" in our data, circa the 1500 d mark in bottom of Figure 5, consistent with the notion of an extant inner disk preserving itself through condensation. Also, the power-law component tends to increase before failed and successful disk restarts, which may physically correspond to the inner edge of a truncated disk moving inward to provide more and hotter seed photons, and/or rapid condensation.

3. VARIABILITY MECHANISMS CONSIDERED

Though the basic physics of companion irradiation and streaming are simple, the dynamics are potentially complicated to initialize and implement in detail, especially if the outer disk warps. However, we can estimate bounds on both mechanisms individually, and because they sit at the edge of the accretion flows, we can lump them into a manual boundary condition for now and still derive meaningful results. CHWs can be launched a bit further inward, but can be described fairly well by simple analytical functions of radius and X-ray luminosity assuming that the corona is easily replenished, and thus we can quickly obtain upper bounds on CHW losses.

Evaporation–condensation can depend sensitively on disk and corona conditions at all radii making it the least amenable to simple estimates, and as noted earlier this same strong dependence on the system's state can naturally engender hysteresis. EC also allows the disk component to vary more substantially and more rapidly by evaporating disk material interior to the circularization radius, but this evaporated disk material can also condense further inward much faster than inner disk conditions change, potentially to the point that $\dot{\mathfrak{M}}_d$ rises and falls simultaneously with $\dot{\mathfrak{M}}_c$. This "sympathetic" accretion mode can be seen in the more detailed simulations of Mayer and Pringle (their Figure 8) and in many cases we simulated (e.g., Figures 8, 11, and 12), but is effectively absent (or negligible) in our observations of

LMC X-3, and thus primarily poses a challenge to our basic EC model.

3.1. SRM Estimates and Remarks

The total supply rate of mass through the L1 nozzle $\dot{M}_s$, will scale with the product of local gas density $\rho_{\rm L1}$, speed at which gas streams through the nozzle (roughly the local sound speed c_s), and area of the nozzle A_n where the latter has width and height roughly equal to the isothermal scale height in the local tidal field, $H_{\rm L1}^2 \approx c_s^2/\Omega_{\rm orb}^2$ (Lubow & Shu 1975). Under X-ray irradiation, each layer of the atmosphere will tend to heat up until it emits the intrinsic stellar flux plus the incident X-ray flux at that altitude. Due to the very steep transition in density at the photosphere, we find most of the X-ray energy is deposited in a thin layer there, which we will take to be infinitesimally thin for now. Thus, the modulation with respect to a given reference state as a function of stellar temperature $T_\star$, effective incident X-ray luminosity $L_{x,\rm eff}$, gravity-darkened stellar luminosity $L_{\star,\rm eff}$, and distance between L1 and the photosphere $d_{L1} - d_{\rm ph}$ is given by Meyer & Meyer-Hofmeister (e.g., 1983):

$$\frac{\dot{M}_s}{\dot{M}_s^{\rm ref}} = \left(\frac{T_\star}{T_\star^{\rm ref}}\right)^{3/2} \exp\left[\left(\frac{d_{L1} - d_{\rm ph}}{H_{\rm L1}^{\rm ref}}\right)^2 \frac{T_\star^{\rm ref} - T_\star}{T_\star^{\rm ref}}\right] \quad (1)$$

where

$$\frac{T_\star}{T_\star^{\rm ref}} = \left(\frac{L_{x,\rm eff} + L_{\star,\rm eff}}{L_{x,\rm eff}^{\rm ref} + L_{\star,\rm eff}}\right)^{1/4}. \quad (2)$$

Short of solving the structure of the stellar envelope in the Roche-lobe potential under time-varying irradiation, we can estimate the extent of SRM by computing the ratio of effective incident-to-intrinsic luminosity. One can make a simple estimate by computing the effective gravity at a point sitting about halfway between the nozzle and the pole of the companion giving $L_{*,\rm eff}/L_* \approx 0.68$, and also use the inclination of this point relative to the inner disk to get the fraction of X-rays emitted into this latitude, $\cos\beta_x = 0.28$, yielding

$$\begin{aligned}\max(L_{x,\rm eff}) &\lesssim 0.3 L_{\rm Edd} \times \cos\beta_x \times \frac{(\pi)(4.0\,R_\odot)^2}{4\pi a^2} \\ &\lesssim 10^6\,L_\odot \times 0.28 \times 0.02 \approx 100\,L_\odot. \quad (3)\end{aligned}$$

The companion's effective stellar luminosity falls within $\sim$500–1000 $L_\odot$ based on the reported bolometric stellar luminosity 800–1600 $L_\odot$ (Soria et al. 2001). More carefully integrating the incident-to-intrinsic ratio over the irradiated face (again, with gravity darkening) agrees closely with this simple estimate as the projected area and fraction of disk flux fall concurrently with (and faster than) the effective gravity toward L1.

For irradiation operating alone, choosing the maximum observed luminosity as the reference point in Equation (1) would permit drops to $\approx$50% of the observed maximum and only if the X-ray source were turned off completely, but this estimate is still fairly sensitive to companion temperature. Harder and more isotropic X-ray flux from a hot corona may enhance modulation, but for LMC X-3 the maximum observed power-law flux is barely a fifth that of the disk, roughly equal to the projection factor reducing inner-disk flux onto the companion. However, even if much deeper drops are possible, and irradiation-driven warping or some other mechanism were included to prevent the system from settling into a permanent steady high-soft state, the fact that SRM affects the flow at the very boundary means that any changes it introduces will suffer severe viscous dampening (Section 4.1). Altogether, this suggests that SRM is significant, but certainly cannot explain the steep $\dot{\mathfrak{M}}_d$ declines by itself.

Furthermore, we consider this simple model's predictions of the SRM magnitude an upper bound in light of as detailed two-dimensional hydrodynamic simulations of the envelope by Viallet & Hameury (2007). They find that irradiation will still drive gas toward the nozzle, but the gas will also have ample time to cool down as it crosses the disk's shadow. They note that because they do not solve for perpendicular velocity it may exceed their estimates near the nozzle, and we remark that warping of the outer disk might reveal more of the companion's equator and nozzle and negate the effects of cooling. For our disk/corona simulations, we ignored the delay between irradiation and changes in $\dot{M}_s$ since we estimated the sound-crossing time of the envelope near L1 to be $\approx$16 hr, far less than the viscous timescale. However, in the case Viallet & Hameury (2007) studied they found that some of the gas may take longer, up to several system orbital periods, to reach the nozzle.

3.2. Bifurcation (DCB) and Warping Estimates

Matter streaming from the L1 point typically collides with the edge of the disk, which usually sits outside the circularization radius due to viscous spreading. Because the disk is relatively cold at this radius, the collision is highly ballistic (Armitage & Livio 1998). The fraction of matter streaming around the disk instead of immediately joining it can then be estimated simply by finding the altitudes at which the vertical disk and stream (both roughly Gaussian) density profiles match, and supposing (Hessman 1999) that all the stream within this range immediately joins the disk while matter outside may stream further in. This yields a streaming fraction,

$$f_s(t) = \mathrm{erfc}\left[\left(\frac{\ln(\rho_{d0}/\rho_{s0})}{1 - (H_s/H_d)^2}\right)^{1/2}\right], \quad (4)$$

where ρ_{d0} and ρ_{s0} are disk and stream densities at $z = 0$ and the stream scale height H_s will not differ much from $H_{\rm L1}$—we also refer to Hessman (1999) for fits to the results of Lubow & Shu (1975).

Irradiation-driven warping of the outer disk may also affect the streaming fraction. Again, Ogilvie & Dubus (2001) and Foulkes et al. (2010) suggest warping is possible in LMC X-3, and the latter work specifically finds a disk tilt of 10º likely for LMC X-3. However, both use an isotropic central luminosity, and the latter use an Eddington ratio in luminosity for LMC X-3 comparable to our derived maximum Eddington ratio in $\dot{\mathfrak{M}}_d$, so we consider their results an upper bound on warping.

We generalize the $f_s(t)$ estimate to a stream that scans the edge of a disk tilted by an angle $\vartheta_d(t)$ above the orbital plane. Here, the vertical density centroid follows $z_0 = R_d\,\sin(\vartheta_d(t)\cos(\Omega_{\rm syn}t))$ where R_d is the radius of the disk edge, and $\Omega_{\rm syn} = \Omega_K(R_d) - \Omega_{\rm sys}$ is the beat frequency between the Keplerian frequency at the disk edge and the system orbital frequency. The finite travel time of the stream should add a roughly constant delay of the order of the local free-fall time, and for now we ignore this effect. Assuming $d\vartheta_d/dt \ll \Omega_{\rm syn}$, the altitudes of equal density are

$$\frac{z_\pm}{H_s} = \frac{z_0 H_s \pm H_d\sqrt{z_0^2 + \left(H_s^2 - H_d^2\right)\ln(\rho_{d0}/\rho_{s0})}}{H_s^2 - H_d^2}. \quad (5)$$

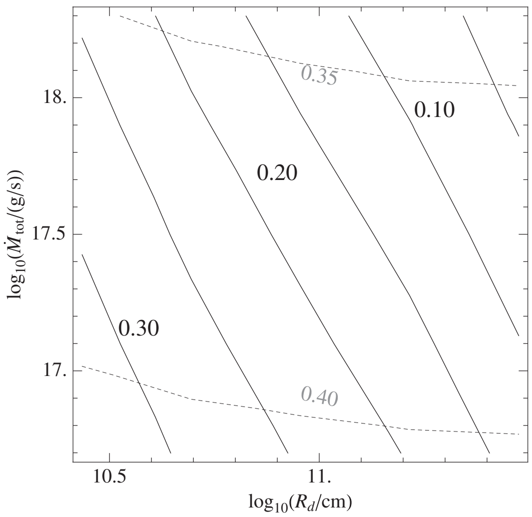

Figure 6. Solid and dashed contours show $\langle f_s \rangle$ for a disk edge tilted by 0° and 10°, respectively, for a gas temperature of 16,500 K, and range of relevant $\dot{M}_{\rm tot}$ and outer disk radius. Tilting the disk edge generally increases $\langle f_s \rangle$, but can also substantially change its dependence on the parameters, with the greatest effects at large R_d and $\dot{M}_{\rm tot}$.

We will see that EC can depend very non-linearly on $f_s(t)$ at the boundary, but for now we use the orbit-averaged $f_s(t)$ as a gauge of plausible DCB strength:

$$\langle f_s(t) \rangle = \frac{1}{2}\left\langle 1 + \mathrm{erf}\left[\frac{z_-}{H_s}\right] + \mathrm{erfc}\left[\frac{z_+}{H_s}\right]\right\rangle_\phi . \qquad (6)$$

We plot $\langle f_s \rangle$ at the outer boundary for relevant ranges of total supply rate, $\dot{M}_{\rm tot}$, and R_d, and for ϑ_d of 0° and 10° in Figure 6. For an untilted disk, the contours are explained by the drop in disk scale height with radius and much slower drop with accretion rate, while for a tilted disk, the scanning greatly washes out the R_d dependence leaving accretion rate as the dominant factor. Our simple estimate also does not resolve the fate of the surviving stream beyond the edge (Foulkes et al. 2010 do, but unfortunately not for LMC X-3 in particular), but should bound the fraction of mass diverted.

3.3. CHW Prescription and Estimates

In Begelman et al. (1983), the authors considered an optically thin corona subject to Compton heating/cooling (ignoring bremsstrahlung and other heating/cooling mechanisms) and pointed out that accretion X-rays can heat the corona at all radii up to a temperature, $T_{\rm iC}$, at which inverse-Compton heating and cooling equilibrate. Whether a wind is launched at a given radius then depends mostly on whether this $T_{\rm iC}$ is greater or smaller than the local virial temperature, $T_{\rm vir}$, and the authors define a radius $R_{\rm iC}$ by where the temperatures are equal, as well as a critical luminosity, $L_{\rm cr} \approx L_{\rm Edd}/33$ at which the gas can be Compton-heated to the virial temperature within the sound-crossing time of the local corona's scale height. Because the tidal gravitational field falls off faster than the source luminosity, gas flows out most easily at large radii. Though primarily a function of source X-ray luminosity and radius, the shape of the source spectrum can affect the mass-loss rate slightly but we ignore this effect. Begelman et al. (1983) computed mass-loss rates for total $\dot{M}_w \lesssim \dot{M}_{\rm tot}$, while later work addresses dynamics and wind limit cycles (Shields et al. 1986).

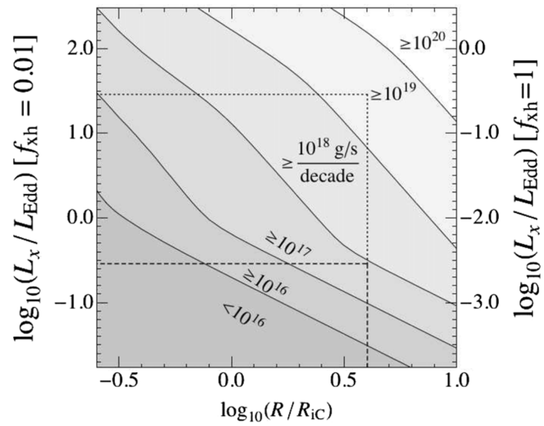

Figure 7. Prescription $\dot{M}_w$ losses per decade in $R/R_{\rm iC}$ with left (right) vertical axis showing Eddington ratio when irradiation efficiency f_{xh} is 0.01 (1). The dashed (dotted) lines show a radial extent of $2R_{\rm circ}$ and luminosity range for LMC X-3 with (without) reduced f_{xh}.

Woods et al. (1996) performed simulations to test the previous analytical prescription and amend it slightly—mostly by noting a shift in the location of $R_{\rm iC}$ and providing corrections for low luminosities that do not immediately concern us. We take their fitting formula for wind losses per unit area

$$\frac{d\dot{M}_w}{dA} = \dot{m}_{\rm ch}\eta^{2/3}\left(\frac{1 + (0.125\eta + 0.00382)^2/\xi^2}{1 + (\eta^4(1 + 262\xi^2))^{-2}}\right)^{1/6} \times \exp[-(1 - (1 + 0.25\xi^{-2})^{-1/2})^2/2\xi], \qquad (7)$$

where the normalization $\dot{m}_{\rm ch}$ is the ratio of corona pressure to sound speed at $R_{\rm iC}$, $\xi = R/R_{\rm iC} \approx 2R/R_{\rm circ}$, and their $\eta = L/L_{\rm cr}$. We then also introduce a factor f_{xh} in $\eta \equiv f_{xh}L/L_{\rm cr}$ for how well X-ray luminosity from an inner disk Compton heats the outer corona compared to the point source considered in the references. Although the outflow geometry may permit parts of the outflow to eventually reach low inclinations relative to the inner disk, the chief hurdle is heating the gas when it is sitting deepest in the tidal gravity field. Integrating $\cos i$ over the solid angle subtended by the outer corona versus half the disk's sky gives $f_{xh} \approx 0.025$. This factor suppresses CHW considerably, while $f_{xh} \approx 1$ implies CHW will have significant effects at the maximum observed luminosities (Figure 7). Furthermore, the f_{xh} for depleting disk flow is likely different and smaller than the corona as the X-rays will have to reach higher inclination, and heat conduction from a transition layer will be competing with advection by the wind.

Winds may also be driven by other means, i.e., magneto-centrifugal and line driving, but extensive simulations by Proga (2003) with parameters relevant to LMC X-3 indicate that these losses in LMC X-3 will be at most a few percent of the total accretion rate.

To gauge CHW self-screening, or screening the companion, consider a wind carrying away 10^{19} g s^{-1} (total, half this per disk face) at the local sound speed at $R_{\rm iC}$. If the density did not fall off with radius, the Thomson optical depth would be

$$n\sigma_{\mathrm{T}}\Delta s \approx \frac{0.5\times 10^{19}[\mathrm{g\,s^{-1}}]/m_p}{R_{\mathrm{iC}}^2(10^8[\mathrm{K}]k_{\mathrm{B}}/m_p)^{1/2}}\sigma_{\mathrm{T}}(a - R_{\mathrm{iC}}) \lesssim 0.15, \quad (8)$$

where a is orbital separation. That this extremely generous upper bound gives marginal absorption indicates that the Compton wind will not screen the companion. Instead, CHW and SRM will likely dampen each other's contribution to $\dot{M}_{\mathrm{tot}}$-variability seen at inner radii as additional X-ray luminosity simultaneously increases $\dot{M}_s$ supplied by the companion and $\dot{M}_w$ lost to space. However, their interaction could enhance the scaling of $\dot{M}_d/\dot{M}_c$ with L_x at large radii.

3.4. PHII Limits and Discussion

The PHII is fundamental to the picture of transient BHXRBs and thus to future extension of our work, but the physics itself is not trivial to implement let alone fully understood as the (60 page) review by Lasota (2001) attests. However, for LMC X-3, the strong, persistent disk emission should generally stabilize the disk within at least $1R_{\mathrm{circ}}$, and we will later show (Section 4.1) that even drastic disk variability outside $R_{\mathrm{circ}}/25$ is still too viscously dampened to explain observations, though the PHII may still contribute to the magnitude of disk variability, and likely plays an important role during complete state transitions.

Taking either the mean or median of $\dot{\mathfrak{M}}_d(t)$ over our data set as a suitable proxy for supply rate gives $\langle \dot{M}_s\rangle \approx 0.1\dot{M}_{\mathrm{Edd}}$, and while the disk beyond $\sim R_{\mathrm{circ}}/3$ will be cool enough to experience the PHII absent irradiation at $0.1\dot{M}_{\mathrm{Edd}}$ (e.g., Figure 1 of Janiuk & Czerny 2011), irradiation can stabilize more and possibly all of the outer disk (Coriat et al. 2012). Work by Dubus et al. (1999) indicates that LMC X-3's disk would become susceptible to instability just beyond R_{circ} at 10^{18} g s^{-1} for typical values of α (0.1) and an overall accretion to irradiation efficiency factor $\mathcal{C}$, originally fit to light curves of the BHXRB A0620-00 and roughly consistent with simple calculations based on an annulus-to-annulus irradiation geometry (see discussion in Kim et al. 1999 and comparison at the end of Dubus et al. 1999 to King et al. 1997).

Because we do not see $\dot{\mathfrak{M}}_d(t)$ decay on R_{circ}-viscous timescales in LMC X-3, it appears that the PHII would also lack a large span of starved inner disk for a heating front to propagate through. After the long, complete state transition of Figure 5, however, the disk recovery is flare-like, consistent with the notion that the PHII can play a significant role in LMC X-3 at low enough disk blackbody flux.

3.5. EC Background and Implementation

As stated in Section 1, EC may occur if the disk and corona are thermally coupled—if the disk cannot efficiently radiate away corona heat conducted onto it, or sufficiently cool the corona via inverse-Compton cooling, then it will experience net heating and evaporate, but otherwise it cools the corona which then condenses onto it. Thus the mass-exchange, or "EC" rate $\dot{M}_z$, is sensitively dependent on the balance of heating and cooling, and the very different scalings of heating and cooling mechanisms involved make possible a wide variety of behaviors. At present, several EC models incorporate viscous and compressive heating, bremsstrahlung, and inverse-Compton cooling in the accretion flow including LTMHM07 and MP07.

Besides separating the thresholds for disk formation/destruction normally degenerate under a bremsstrahlung-only density criterion via inverse-Compton cooling, and thus engender hysteresis (Meyer-Hofmeister et al. 2009), it is also possible to evaporate the outer disk but condense it back onto the inner disk rapidly enough to drive correlated rises (and falls) of $\dot{\mathfrak{M}}_d$ with $\dot{\mathfrak{M}}_c$ (again, Figure 8 of MP07 and prominently in the left panel of our Figure 11). It is also possible to preferentially evaporate the middle of a disk to the point of destroying it as visible in Meyer et al. (2007), MP07, and several of our simulations.

For our initial EC implementation, we do the following. We assume azimuthal symmetry for the accretion flow and divide it into 45 logarithmically spaced radial zones with a single virtual corona zone associated with each disk zone (i.e., the code is 1.5D). We evolve the disk by solving mass fluxes with the standard viscous-disk equations (Frank et al. 2002) and a simple donor-cell scheme. Meanwhile we assume that the local corona properties and EC rates match those of the steady-state corona and $\dot{M}_z$ solutions from LTMHM07 for the same local accretion rate and evolve the corona working inward from the outer boundary condition.

More specifically, for each disk zone we compute zone-boundary ($j \pm 1/2$) velocities

$$(v_d)_{j+\frac{1}{2}} = \frac{3((\nu\Sigma R^2\Omega_K)_j - (\nu\Sigma R^2\Omega_K)_{j+1})}{2R^2\Omega_K\Delta R} \quad (9)$$

with a viscosity based on a standard thermal equilibrium thin disk solution assuming Kramer's opacity as in Frank et al. (2002):

$$\nu_d = 2.13\times 10^9\left(\frac{M_{\mathrm{bh}}}{M_\odot}\right)^{5/7}\alpha_d^{8/7}\left(\frac{3R}{R_S}\right)^{15/14}\Sigma_d^{3/7}. \quad (10)$$

The overall disk and corona evolution is then governed by

$$\Delta(\Sigma_d\Delta A)_j/\Delta t = (\dot{M}_d)_{j-\frac{1}{2}} - (\dot{M}_d)_{j+\frac{1}{2}} - \left(\dot{M}_z^{\mathrm{Rx}}\right)_j \quad (11)$$

and

$$(\dot{M}_c)_{j-\frac{1}{2}} = (\dot{M}_c)_{j+\frac{1}{2}} + \left(\dot{M}_z^{\mathrm{Rx}}\right)_j, \quad (12)$$

where ΔA_j is the zone area. The fluxes are also limited so as not to draw mass from a disk zone or the corona flow than is physically available, and the "Rx" emphasizes that we are plugging in the EC rates of LTMHM07 as a function of radius, and local $\dot{M}_c$ and effective disk temperature. If $\dot{M}_c$ and $\dot{M}_z$ are anywhere comparable (of the same order of magnitude) to the viscous disk fluxes, then the computations are performed only once. Otherwise, the latter two steps are relaxed further, and allowed to change Σ_d but not $\dot{M}_d$, until their iterations converge within a given tolerance (or exceed an iteration limit). We note that large $|\dot{M}_z|$ can lead to oscillatory behavior with this simple scheme, which can be subdued but not fundamentally fixed with smaller time steps and tolerances. This can be seen in the results of our simulations (Figures 11–13) as small sudden jumps in $\dot{M}_c$ (and somewhat in $\dot{M}_d$ when EC is strong at small radii), but by changing time step and tolerance we have found that this does not impact the general, longer timescale features that immediately concern us. We also explored small changes in the number of radial zones, obtaining similar results with 40 or more grid points, but our results diverged very quickly for coarser grids.

For steady input conditions, we confirm that our method does well reproducing cases considered by LTMHM07 (treating the disk fully lets it spread viscously to larger sizes mildly enhancing condensation). To test our method's treatment of

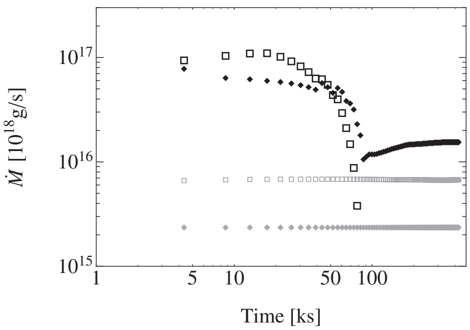

Figure 8. The larger, darker empty squares and filled diamonds show $\dot{\mathfrak{M}}_d$ and $\dot{\mathfrak{M}}_c$, respectively, at the inner boundary for a run with modified heat conduction fluxes (see text Section 3.5), and the smaller, lighter symbols show the corresponding $\dot{\mathfrak{M}}_d$ and $\dot{\mathfrak{M}}_c$ for default parameters—here we plot time logarithmically for more direct comparison with Figure 8 of MP07.

dynamic behavior, we looked at the same case MP07 studied: a disk spanning 3000 Schwarzschild radii around a $10\,M_\odot$ black hole with fixed boundary corona fraction f_s of 0.1 and mass supply rate of 10^{-3} times Eddington $\dot{M}_{\rm Edd}$. Their time-dependent method evolves the corona self-consistently on its dynamical timescale making it more physically realistic, but this also requires many more time steps. We found that with default parameters and physics our code never evaporates any part of the disk, while MP07 predict the formation of a gap that eats its way inward. However, we also found that if we scaled up the heat-conduction fluxes predicted by LTMHM07 for zones where inverse Compton cooling does and does not set the electron temperature by a factor of three and five, respectively (adjusting the formula identifying the zones accordingly) then we do obtain good agreement with MP07 (see Figure 8, and their Figure 8). By preferentially scaling up heat fluxes in the zones where inverse-Compton cooling limits electron temperature, we obtained more rapid evaporation starting further inward while doing the same for heat fluxes in non-Compton zones led to increased stability. In this particular case, we saw little change when lowering the gas-to-total pressure ratio, β_c, a global constant in LTMHM07, from 0.8 to 0.1.

Both the models of LTMHM07 and MP07 necessarily neglect, or precede, some additional physical effects that may be relevant to our early results so we discuss them here (and summarize in Figure 9) to motivate our more exploratory simulations (Section 4.2 and Figure 12). In both models, condensation is a smooth, unresolved flow, but applying the results of Wang et al. (2012) shows that the corona is liable to clump at radii greater than roughly $100R_{\rm id}$ under typical conditions for LMC X-3. Such clumping potentially increases cooling (thus condensation) efficiency. Both LTMHM07 and MP07 use Spitzer electron conduction throughout the problem domain, and both suspect that the effective thermal conduction coefficient κ may be significantly smaller. Although the degree of tangling in the magnetic fields of the transition zone is far harder to constrain, it is amenable to parameterization. Meanwhile, Cao (2011) provides a recent calculation for how much the ordered component of field shifts from predominantly poloidal outside $\sim 10R_{\rm id}$ to predominantly toroidal inside. Lastly, neither model includes mechanisms to spontaneously produce corona, a point MP07 especially emphasize. Indeed, since Galeev et al. (1979) derived that within a certain radius, the buoyancy of magnetic loops formed within the disk can outpace their reconnection leading to a carpet of buoyant loops, this solar-like corona has often been invoked as a partial or complete source of corona. For LMC X-3, the condition on radius in Galeev et al. (1979) gives $R \lesssim 300(\dot{M}_{\rm Edd}/\dot{\mathfrak{M}}_d)R_S$. It is hard to imagine this mechanism alone generating $\dot{\mathfrak{M}}_c$ pulses that anticipate $\dot{\mathfrak{M}}_d$ drops lasting substantially longer than the viscous timescale at $\sim 100R_S$, but it may play an important role by reheating and replenishing the corona, and affecting the local magnetic field geometry.

An important caveat in applying the LTMHM07 model came to our attention after running our simulations. For $\dot{M}_c \gtrsim 0.1$ Eddington near $R \sim 100R_S$, the conduction or Compton-cooling (at high $\dot{\mathfrak{M}}_d$) limiting temperatures may cross the coupling temperature (e.g., Bradley & Frank 2009). Under these conditions, the model will tend to overpredict condensation and thus exaggerate the amplitude and duration of the sympathetic mode, but triggering the effect requires strong, correlated $\dot{\mathfrak{M}}_c$, $\dot{\mathfrak{M}}_d$ to already be underway.

4. SIMULATION RESULTS

4.1. Models without EC

To illustrate how a combination of non-EC mechanisms has difficulty explaining the magnitude of $\dot{M}_d$ drops and especially the pattern of rapid decline versus slow recovery, we employ a very simple model where disk accretion is computed using the analytical machinery of Zdziarski et al. (2009). The latter is derived assuming a time-independent viscosity with power-law dependence on radius, and we referred to the thin-disk solutions of Frank et al. (2002, p. 93) for all relevant viscosity parameters. This method prevents incorporating radial dependence of $\dot{M}_w$, but because wind losses fall rapidly with decreasing radius, and since we predict they are fairly weak anyway, assuming that they take place near the boundary does not invalidate the main results of this toy model. This method also precludes incorporating he PHII, but as discussed in Section 3.4 the main effects of the PHII should typically be limited to radii beyond $\sim R_{\rm circ}$ in LMC X-3.

The left panel in Figure 10 shows a calculation with this reduced model geared toward reproducing the first disk drop in Figure 5. We set f_s manually, and SRM and wind losses were also computed beforehand as functions of the observed $\dot{\mathfrak{M}}_d$. To reproduce the depth of the first drop, we first allowed sustained f_s of 100% and when this proved insufficient we moved the outer disk radius inward to a mere $0.04R_{\rm circ}$ for the runs shown, still employing f_s of 100%, and leading to massive $\dot{\mathfrak{M}}_c$ pulses compared to our estimates. This can be corrected somewhat by invoking a wind stronger than our estimates.

Besides requiring unrealistic values with respect to our estimates, and an extreme ad hoc disk truncation, the toy model resists efforts to simultaneously improve agreement with other major features of the data. To improve model–data agreement for the second disk drop in the left panel of Figure 10 without increasing disk radius (which would obviously undo agreement with the first $\dot{\mathfrak{M}}_d$ drop) requires either increased SRM or increasing the height and duration of the second coronal pulse. The latter will generate obvious disagreement with the second $\dot{\mathfrak{M}}_c$ pulse by attaching a tail that is very clearly not observed; the former significantly reduces the amplitude of the first coronal pulse relative to the second so that one must invoke a stronger and more complicated wind mechanism.

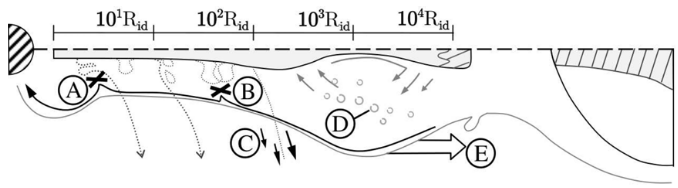

Figure 9. Possible complications to the model especially concerning EC (Sections 3.5 and 5). At small radii, the magnetic field (dotted lines) in the corona and at the disk–corona interface may be significantly non-poloidal thus suppressing condensation (A), and further outward buoyant magnetic loops may still alter the magnetic field geometry besides introducing additional reconnection heating to the corona to continue suppressing condensation (B). MHD winds might also be stronger than predicted and carry away more of the corona (C), while clumping of the corona at large radii may instead enhance condensation over evaporation there (D). The potential for the corona to viscously outflow radially wherever it achieves large density gradients (E) may also significantly affect our results.

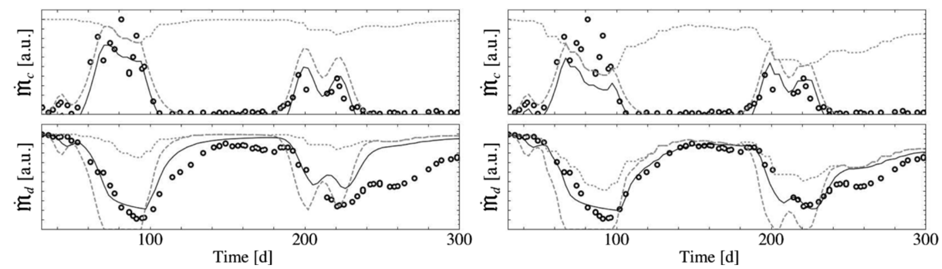

Figure 10. The solid curves in the bottom (top) panels show $\dot{\mathfrak{M}}_d$ ($\dot{\mathfrak{M}}_c$) simulated with the simplified model discussed in Section 4.1 and empty circles show the observed $\dot{\mathfrak{M}}_d$ ($\dot{\mathfrak{M}}_c$), where the simulation units first are chosen to match the observed and simulated initial $\dot{\mathfrak{M}}_d$, as the simple model's disk machinery has no direct dependence on absolute accretion rate. The data points in the top panels are then scaled so that the maximum observed $\dot{\mathfrak{M}}_c$ equals the initial $\dot{\mathfrak{M}}_d$ which is a much larger absolute scale than our estimates suggest. The right panels are for a run with greater variability in the total mass supply which is shown as a dotted curve in all panels. The dashed curves show the effective corona/disk inputs at the outer boundary so that the remaining difference between solid and dashed curves in top panels indicates the wind loss.

Again, the chief problem is that a disk flow will be viscously smeared too much to match observations unless variability is driven at a relatively small radius where even maximally efficient CHW should be insubstantial, and the PHII should not operate or regularly drive heating fronts. In the next section, we will show how EC may introduce a evaporation-to-condensation transition or gap at radii comparable to the outer edge of the arbitrarily truncated disk of the toy model, but that it also tends to overpredict condensation at inner radii, generating correlated $\dot{\mathfrak{M}}_d$–$\dot{\mathfrak{M}}_c$ rises and falls inconsistent with observations.

4.2. Models Including EC

Except where specifically noted otherwise, for these simulations we again use $\alpha_d = 0.1$, but a corona $\alpha_c = 0.2$, the standard Spitzer coefficient for electron thermal conduction, a $\beta_c = 0.8$ for the LTMHM07 EC prescription, the observationally favored $R_{\rm circ} = 2.7 \times 10^{11}$ cm, assume $R_{\rm id}$ is $3R_S$, and set $f_{xh} = 0.03$. We note here that the SRM results from Section 3.1 specifically correspond to a value of $L^{\rm ref}_{x,\rm eff}/L^{\rm ref}_{\star,\rm eff} = 0.4$ for $\dot{\mathfrak{M}}_d = 10^{18}$ g s^{-1}, and to 6.5 scale heights between the nozzle and the stellar surface for $T^{\rm ref}_{\star} = 16500$ K.

For the EC-inclusive model, we first simulated a disk with standard density profile extending to the circularization radius reacting to a mild Gaussian $f_s(t)$ pulse, and show the results in the left panel of Figure 11. Two immediately remarkable features include the sympathetic rise and fall of $\dot{\mathfrak{M}}_d$ with $\dot{\mathfrak{M}}_c$, and the general saturation of $\dot{\mathfrak{M}}_c$ response when the outer disk is most intensely siphoning onto the inner disk. This saturation physically arises from the steep transition between evaporation and condensation. In the mass exchange model of LTMHM07 that we employ, the local evaporation/condensation rate $\dot{M}_z$, varies with the local corona accretion rate in terms of Eddington ratio, $\dot{m}_c$, like

$$\dot{M}_z \sim a\dot{m}_c^{7/5}\left(1 - b\dot{m}_c^{20/21}\right) \quad (13)$$

where a and b are functions of many other parameters, local variables, and radius itself. If these other variables vary weakly with radius, then a very dense corona at some radius will lead to efficient condensation slightly further inward, and subsequent changes in $\dot{M}_z$ about zero will be driven by the weaker variations in the critical value of $\dot{m}_c$.

The issue of sympathetic accretion prompted us to consider a scenario in which the outer disk mass most vulnerable to being siphoned has already been evaporated away, such that there is a gap in the outer disk. We first studied the effects of simply truncating the disk, and show an example with radius 3×10^{10} cm and default LTMHM07 EC parameters in the right panel of Figure 11. Truncating the disk to this radius prevents triggering sympathetic accretion while generating appreciable $\dot{\mathfrak{M}}_d$ variability and diminishing, but not eliminating, EC's role in amplifying variability over the simulation domain.

We next attempted to generate this gap self-consistently, while preserving the interior aspect of the accretion flow that works fairly well. To this end, we first subjected a full disk to a constant f_s at the boundary. The run confirmed that a small seed corona can rapidly evaporate the outer disk, that this corona is immediately condensed only slightly inward, but also that the process of forming a complete gap would take on the order of years in our standard EC implementation. To pursue this idea further, we ran simulations with a gap already inserted of which Figure 12 is representative. Besides the initial relaxation of $\dot{\mathfrak{M}}_d$ due to viscous spreading of the inner disk exceeding

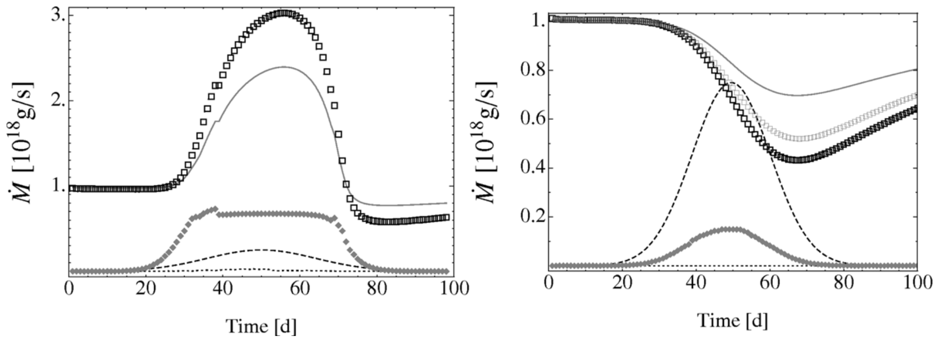

Figure 11. Results with rough EC-implementation showing $\dot{\mathfrak{M}}_d$ (empty black squares), $\dot{\mathfrak{M}}_c$ (filled diamonds), $\dot{M}_{\rm tot}$ (solid line), $\dot{M}_w$ (dotted line), $f_s \times 10^{18}$ g s^{-1} (dashed line) while $\dot{\mathfrak{M}}_d$ without EC turned on (gray empty squares) is included for the right panel. The run on the left uses the full circularization radius and shows strong condensation while the right panel shows a run with a disk size of 3×10^{10} cm (Section 4.2).

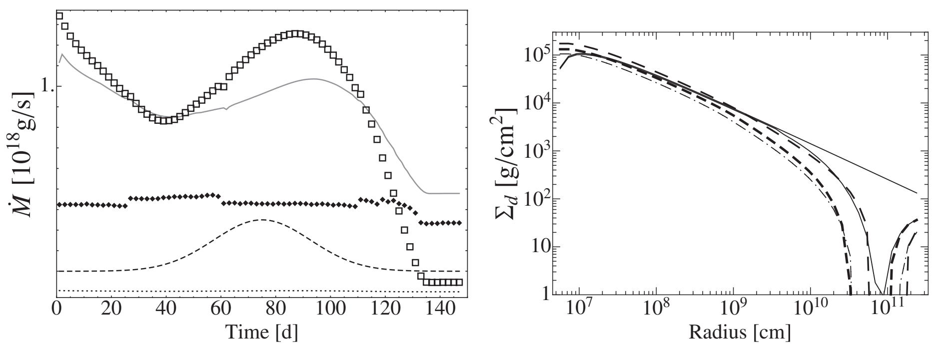

Figure 12. Accretion history (left, see Figure 11 caption for symbol meanings) and evolution of the disk surface density profile (right) with snapshots at 80, 100, and 120 days shown in long-dashed, thick-dashed, and dot-dashed lines while the thin solid curves show the gap initial conditions relative to the standard thin disk.

and resupply via condensation, one can see that sympathetic accretion is still an issue, and $\dot{M}_c$ variability inward of the gap is severely suppressed again, as the high corona fraction of the gap triggers the saturation effect described above.

Since our standard model and implementation of EC faces fundamental problems in reproducing major features of the data, we studied the effects of introducing physically motivated, if not yet rigorously justified, modifications. Thus far, it appears that the most successful modifications follow a fairly strict pattern of effectively raising the coronal heating and critical evaporation-to-condensation $\dot{m}_c$ over the innermost two decades in $R/R_{\rm id}$. The latter is nearly inversely proportional to b in Equation (13) which in the model of LTMHM07 scales with the corona viscosity parameter α_c, radius, electron thermal conduction coefficient κ, and gas-to-total pressure ratio β_c as

$$b \sim \beta_c \kappa^{1/5} \alpha_c^{-14/15} \left(\frac{R}{R_{\rm id}}\right)^{-1/10} \quad (14)$$

though we should point out that β_c enters their model strictly via a prescription for compressive heating. In the simulations producing Figure 13, we raised α_c linearly from 0.2 to 0.4 inward over $100 R_{\rm id}$, and independently adjusted b over radial zones spanning 10^0–$10^{2.7}$, $10^{2.7}$–$10^{3.4}$, and $10^{3.4}$–$10^{4.6}$ in $R/R_{\rm id}$. For run A in Figure 13, we scaled b in these zones by 0.1, 0.2, and 0.4, respectively, and for run B by 0.4, 0.6, and 0.8. Although the simulated $\dot{M}_c$ pulses are far more massive than observations indicate, these modifications very clearly control the degree of hysteresis versus sympathetic accretion. If the overall magnitude of EC is smaller, then for higher f_s, and/or SRM moderately larger than expected, this modified model could reproduce the observed hysteresis.

The most conceivably adjustable parameters in Equation (14) are α_c, especially if understood to include other heating mechanisms, and κ. Since the current contrast between simulation and observation still favors weaker EC, the requirement on additional heating would not likely be as extreme as implied by our modifications, but this then requires even greater deviation in κ which affects b rather weakly, and these parameters are not necessarily independent in reality.

5. DISCUSSION AND CONCLUSIONS

Thus far, we still cannot offer a very definitive solution for LMC X-3's behavior, but we have more rigorously examined several physical mechanisms popularly invoked to explain variability in LMC X-3 and additionally considered evaporation and condensation. We have found that if condensation is suppressed at inner radii (or over-predicted in the current model), then EC may naturally reconcile the observational evidence for RLO accretion and associated circularization radius, as well as the large amplitude, long duration, and rapid declines in hysteresis episodes with our estimates of other

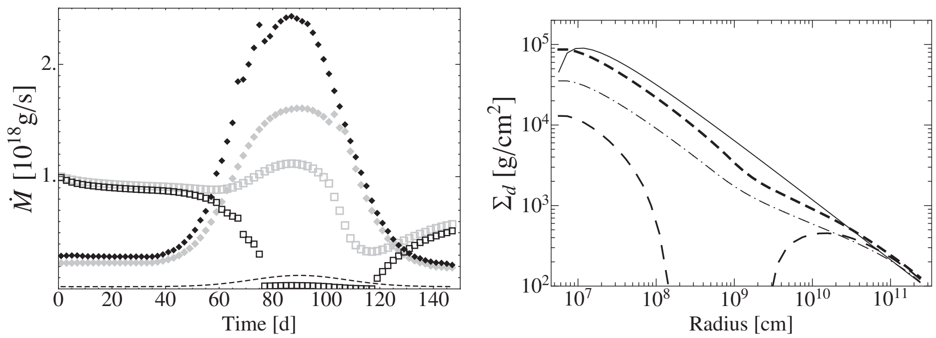

Figure 13. Left panel shows accretion histories for $\dot{\mathfrak{M}}_d$ (empty squares) and $\dot{\mathfrak{M}}_c$ (diamonds) in cases A (thin, black), and B (thick, light gray) as described in Section 4.2 where $f_s \times 10^{18}$ g s^{-1} is also shown again, but $\dot{M}_s$ and $\dot{M}_w$ are omitted. The right panel shows evolution of disk surface density profile for case A at 60, 90, and 120 days with the same convention as in Figure 12.

major viscous timescale variability mechanisms and the viscous dampening that they would undergo.

However, we wish to emphasize that our current EC implementation and the steady-state theory informing it by default led to excessive condensation when compared as accurately as possible to observations, and it led to significantly different predictions for the particular low-$\dot{M}_s$ case studied by MP07. As discussed in Section 3.5, both the LTMHM07 and MP07 models necessarily neglected some physics, some of which might enhance heating and/or suppress conduction closer to the black hole, and thus help explain the discrepancy between observations and the predictions of our code with the default EC prescription.

To this end, we have reproduced and are testing a code that follows MP07 and evolves the disk and corona mass and energy equations self-consistently. An additional advantage is that we can naturally include physics behind the PHII by incorporating detailed results for disk cooling as a function of density and central temperature from previous work—crucial for studying transient systems. However, this explicit method suffers from advancing by a very small time step. We have started building a parallelized implicit method which we hope to develop further during simulations with the explicit method, but we also hope to find ways to save on excessive computation through better physical understanding of the problem.

Our estimates for the reduced efficiency of CHW, and cursory examination of theory results for MHD winds in similar systems. Proga (2003) suggest that winds in general will have little affect on accretion dynamics in LMC X-3. However, we will continue to consider how efficiency of CHW might be increased, or that MHD winds may be stronger than anticipated (e.g., King et al. 2012).

Other assumptions in our current modeling that bear repeated mention include the alpha-prescription disk, and how we infer and interpret the disk and coronal accretion rates. Regarding the former, it is at least expected that under conditions associated with jet flow, angular momentum transport via the magnetically driven outflow may become substantial or dominant compared to viscous transport (i.e., the magneto-rotational instability) at least within the inner flow (e.g., Zanni et al. 2007; Casse & Ferreira 2000). Evolution of the magnetic fields in the disk may also lead to intrinsic variability out to $\sim 100 R_{\rm id}$, as in de Guiran & Ferreira (2011). The potential for corona flow to stall centrifugally as a function of external flow conditions and local viscosity (e.g., Chakrabarti & Titarchuk 1995; Garain et al. 2012) might be realized in LMC X-3, but is also usually expected to occur well within the innermost $100 R_{\rm id}$ of the flow and to destroy the disk interior to the centrifugal shock, so it may be most relevant to state transitions. If more frequently prevalent though, the latter could alter our picture of spectral production, enhance $\dot{\mathfrak{M}}_c$ variability especially on shorter timescales, and change the dynamics of EC. Based on the pattern of the power-law component to anticipate declines in blackbody flux and the viscous recovery timescale of the blackbody component, we are still naturally inclined to favor a picture where variability is driven outside-in so that mechanisms like these and EC would predominantly accelerate and enhance $\dot{\mathfrak{M}}_d$ declines driven by known mechanisms operating in the outer flow.

Our immediate focus will be resolving the outstanding questions regarding the current mechanisms considered, especially evaporation and condensation. After understanding and constraining these better, we hope to extend our investigations to additional physics, systems, and phenomena, especially the transients and jet launching.

The authors acknowledge support through the NASA ADP program grant NNX09AC86G. The authors would also like to thank the referee for suggestions that improved the content and clarity of the paper.

APPENDIX

RELATING ACCRETION RATES TO SPECTRA PRODUCTION

For the blackbody spectrum, Zimmerman et al. (2005) note that `XSPEC` fits the maximum temperature and normalization constant to a temperature profile of the form $T(R) = T_{\rm max}(R_{\rm id}/R)^{3/4}$. The fit to the peak temperature using this profile is only $\sim$5% smaller than the peak temperature found fitting a temperature profile based on a zero torque boundary condition and color-correction factor $f_{\rm col}$ (Ebisuzaki et al. 1984):

$$T_{\rm bb}(R) = f_{\rm col} T_{\rm eff}(R) = T_*(R_{\rm id}/R)^{3/4}\left(1 - \left(\frac{R_{\rm id}}{R}\right)^{1/2}\right)^{1/4}, \tag{A1}$$

where

$$T_* = f_{\rm col}\left(\frac{3GM_{\rm bh}\dot{\mathfrak{M}}_d}{8\pi\sigma_{\rm SB}R_{\rm id}^3}\right)^{1/4} = 2.05T_{\rm max}. \quad (A2)$$

Because there is little difference in the fitted peak temperatures, because we plan to fix the black hole mass and $R_{\rm id}$, and because we prefer the physically motivated temperature profile we will use it instead. Integrating over disk annuli then gives the familiar formula for flux:

$$F_\nu^{\rm mbb} = \frac{1}{f_{\rm col}^4}\frac{4\pi h\cos i\,\nu^3}{c^2 d_{\rm sys}^2}\int_{R_{\rm id}}^{R_d}\frac{R\,dR}{\exp(h\nu/f_{\rm col}k_{\rm B}T_{\rm eff}(R))-1}. \quad (A3)$$

Because Shimura & Takahara (1995) predict that $f_{\rm col}$ depends weakly on radius, accretion rate, and other parameters, we fix $f_{\rm col} = 1.7$. This then implies that the maximum disk accretion rate ranges from 0.07–0.29$\dot{M}_{\rm Edd}$ for $R_{\rm id}$ spanning 1 to 3 Schwarzschild radii. We scale the $\dot{\mathfrak{M}}_d$ of Figure 5 by matching the observation with the highest blackbody flux and temperature to the maximum 0.29$\dot{M}_{\rm Edd}$. We note that if dissipation interior to the last stable circular orbit is significant, this will also put the actual $\dot{\mathfrak{M}}_d$ below our estimate (Beckwith et al. 2008; Shafee et al. 2008).

Inferring $\dot{\mathfrak{M}}_c(t)$ requires additional assumptions but many are well constrained within ADAF theory (Narayan & Yi 1995b). Specifically, theory predicts that corona ions are very effectively virialized at inner radii and much hotter than the electrons, whose exact temperature depends on many conditions, but is generally flat over the innermost $100R_{\rm id}$ and of the order of 100 keV in the cases considered by Narayan & Yi (1995b). The former means that we can confidently predict scale height given corona α_c while the latter provides some justification for choosing a constant electron temperature in corona emission calculations. Taking $R_{\rm id} = 3R_S$, corona alpha parameter $\alpha_c = 0.2$, and gas-to-magnetic pressure ratio $\beta_c = 0.8$, we obtain (Narayan & Yi 1995b) the following estimates for corona density n_c, corona height H_c, and coronal optical depth τ in terms of $\dot{m}_c = \dot{\mathfrak{M}}_c/\dot{M}_{\rm Edd}$,

$$n_c(R_{\rm id},\dot{m}_c) \approx 1.2\times10^{19}\dot{m}_c(M_\odot/M_{\rm bh})[{\rm cm}^{-3}], \quad (A4)$$

$$H_c(R_{\rm id},\dot{m}_c)/R_{\rm id} = h_c \approx 1, \quad (A5)$$

$$\tau(R_{\rm id},\dot{m}_c) \approx 58\dot{m}_c. \quad (A6)$$

However, we remind the reader that the latter is fairly sensitive to α_c, scaling roughly like α_c^{-1}. If we take the scattering fraction to be $\mathcal{P}_\tau = 1 - e^{-\tau}$ then based on the scattering fractions returned by XSPEC for the mixed states, inversion gives us the simple $\dot{\mathfrak{M}}_c$ estimate shown as the solid line in Figure 5.

We compare this simple estimate with a more detailed power-law flux calculation. Hua & Titarchuk (1995) find a Green's function for the output energy spectrum given the seed photon energy spectrum per scattered seed photon (specifically, their Equation (9)), $G_\nu(x, x_s, T_e, \mathcal{P}_\tau)$. The latter depends again on scattering fraction, as well as corona electron temperature T_e, and the output (x) and seed (x_s) dimensionless photon energies ($x_* = h\nu_*/k_{\rm B}T_e$). Using the result of a more detailed calculation for the scattering fraction in a slab geometry from Zdziarski et al. (1994),

$$\mathcal{P}_\tau = 1 + \frac{1}{2}e^{-\tau}\left(\frac{1}{\tau}-1\right) - \frac{1}{2\tau} + \frac{\tau}{2}{\rm Ei}(1,\tau), \quad (A7)$$

we convolve $G_\nu(x, x_s, T_e, \mathcal{P}_\tau)$ with the flux of seed photons that can scatter (overall $\mathcal{P}_\tau$ factor) out of the modified blackbody spectrum. In terms of $r = R/R_{\rm id}$, and T_* the power-law energy spectrum, F_E is given by

$$F_E = \frac{1}{4\pi d_{\rm sys}^2}\mathcal{P}_\tau\int_0^\nu d\nu_s\int_1^{40}dr\,h\,G_\nu(x, x_s, T_e, \mathcal{P}_\tau)\frac{1}{f_{\rm col}^4}\frac{2h\nu_s}{c^2} \times \frac{2\pi r/(1+0.25h_c^2/(r-1)^2)^{1/2}}{\exp\left(h\nu_s(r^{3/4}(1-r^{-1/2})^{-1/4})/k_BT_*\right)-1}. \quad (A8)$$

Note that we have assumed that the corona emission is largely isotropic, but we have included the projection factor for blackbody emission from each annulus to half the height of the corona at $r = 1$, and we confirmed that $r = 40$ is a numerically acceptable cutoff. Fixing $\Gamma_{\rm pli} = 2.34$ and $T_e = 150$ keV (T_e dependence is relatively weak for $T_e \gg \max(T_*, 25\,{\rm keV}/k_{\rm B})$) we tabulated integrated flux for a range of $T_{\rm max}$ and $\dot{\mathfrak{M}}_c$ to be inverted numerically, ultimately obtaining the $\dot{\mathfrak{M}}_c$ points in the upper panel of Figure 5. For relatively high $T_{\rm bb}$ and low τ they agree fairly well with the simpler method, with the main difference due to the less step-like $\dot{\mathfrak{M}}_c$–τ relationship in the more detailed P_τ. However, to explain observations with higher F_{pl} and lower $T_{\rm bb}$, the formula quickly requires excessively high $\dot{\mathfrak{M}}_c$, and at these implied optical depths the formula itself becomes unreliable.

REFERENCES

Armitage, P. J., & Livio, M. 1998, ApJ, 493, 898

Arnaud, K. A. 1996, in ASP Conf. Ser. 101, Astronomical Data Analysis Software and Systems V, ed. G. H. Jacoby & J. Barnes (San Francisco, CA: ASP), 17

Beckwith, K., Hawley, J. F., & Krolik, J. H. 2008, MNRAS, 390, 21

Begelman, M. C., McKee, C. F., & Shields, G. A. 1983, ApJ, 271, 70

Bradley, C. K., & Frank, J. 2009, ApJ, 704, 25

Cannizzo, J. 1998, ApJ, 494, 366

Cao, X. 2011, ApJ, 737, 94

Casse, F., & Ferreira, J. 2000, A&A, 353, 1115

Chakrabarti, S., & Titarchuk, L. G. 1995, ApJ, 455, 623

Coriat, M., Fender, R. P., & Dubus, G. 2012, MNRAS, 424, 1991

de Guiran, R., & Ferreira, J. 2011, arXiv:1112.5343

Done, C., Gierliński, M., & Kubota, A. 2007, A&ARv, 15, 1

Dubus, G., Lasota, J.-P., Hameury, J.-M., & Charles, P. 1999, MNRAS, 303, 139

Ebisuzaki, T., Sugimoto, D., & Hanawa, T. 1984, PASJ, 36, 551

Esin, A. A., McClintock, J. E., & Narayan, R. 1997, ApJ, 489, 865

Fender, R., Corbel, S., Tzioumis, T., et al. 1999, ApJL, 519, L165

Fender, R. P., Southwell, K., & Tzioumis, A. K. 1998, MNRAS, 298, 692

Foulkes, S. B., Haswell, C. A., & Murray, J. R. 2010, MNRAS, 401, 1275

Frank, J., King, A., & Raine, D. 2002, Accretion Power in Astrophysics (3rd ed.; Cambridge: Cambridge Univ. Press)

Galeev, A., Rosner, R., & Vaiana, G. 1979, ApJ, 229, 318

Garain, S. K., Ghosh, H., & Chakrabarti, S. K. 2012, ApJ, 758, 114

Hessman, F. V. 1999, ApJ, 510, 867

Homan, J., & Belloni, T. 2005, Ap&SS, 300, 107

Hua, X.-M., & Titarchuk, L. 1995, ApJ, 449, 188

Janiuk, A., & Czerny, B. 2011, MNRAS, 414, 2186

Kim, S.-W., Wheeler, J. C., & Mineshige, S. 1999, PASJ, 51, 393

King, A. L., Miller, J. M., Raymond, J., et al. 2012, ApJL, 746, L20

King, A. R., Kolb, U., & Szuszkiewicz, E. 1997, ApJ, 488, 89

Lasota, J.-P. 2001, NewAR, 45, 449

Liu, B. F., Taam, R. E., Meyer-Hofmeister, E., & Meyer, F. 2007, ApJ, 671, 695

Lubow, S., & Shu, F. 1975, ApJ, 198, 383

Mayer, M., & Pringle, J. E. 2007, MNRAS, 376, 435
Meyer, F., Liu, B. F., & Meyer-Hofmeister, E. 2007, A&A, 463, 1
Meyer, F., & Meyer-Hofmeister, E. 1983, A&A, 121, 29
Meyer-Hofmeister, E., Liu, B. F., & Meyer, F. 2009, A&A, 508, 329
Montgomery, M., & Martin, E. 2010, ApJ, 722, 989
Nandi, A., Debnath, D., Mandal, S., & Chakrabarti, S. K. 2012, A&A, 542, A56
Narayan, R., & Yi, I. 1995a, ApJ, 444, 231
Narayan, R., & Yi, I. 1995b, ApJ, 452, 710
Ogilvie, G. I., & Dubus, G. 2001, MNRAS, 320, 485
Page, M. J., Soria, R., Wu, K., et al. 2003, MNRAS, 345, 639
Pringle, J. E. 1992, MNRAS, 258, 811
Proga, D. 2003, ApJ, 585, 406
Shafee, R., Narayan, R., & McClintock, J. E. 2008, ApJ, 676, 549
Shakura, N. I., & Sunyaev, R. A. 1973, A&A, 24, 337
Shields, G. A., McKee, C. F., Lin, D. N. C., & Begelman, M. C. 1986, ApJ, 306, 90
Shimura, T., & Takahara, F. 1995, ApJ, 445, 780
Smale, A. P., & Boyd, P. T. 2012, ApJ, 756, 146
Smith, D. M., Dawson, D. M., & Swank, J. H. 2007, ApJ, 669, 1138
Smith, D. M., Heindl, W. A., & Swank, J. H. 2002, ApJ, 569, 362
Soria, R., Wu, K., Page, M. J., & Sakelliou, I. 2001, A&A, 365, L273
Val-Baker, A. K. F., Norton, A. J., & Negueruela, I. 2007, in AIP Conf. Proc. 924, The Multicolored Landscape of Compact Objects and Their Explosive Origins, ed. T. di Salvo, G. L. Israel, L. Piersant et al. (Melville, NY: AIP), 530
van der Klis, M., Clausen, J. V., Jensen, K., Tjemkes, S., & van Paradijs, J. 1985, A&A, 151, 322
Viallet, M., & Hameury, J.-M. 2007, A&A, 475, 597
Wang, J.-M., Cheng, C., & Li, Y.-R. 2012, ApJ, 748, 147
Wilms, J., Nowak, M. A., Pottschmidt, K., et al. 2001, MNRAS, 320, 327
Woods, D. T., Klein, R. I., Castor, J. I., McKee, C. F., & Bell, J. B. 1996, ApJ, 461, 767
Zanni, C., Ferrari, A., Rosner, R., Bodo, G., & Massaglia, S. 2007, A&A, 469, 811
Zdziarski, A. A., Fabian, A. C., Nandra, K., et al. 1994, MNRAS, 269, L55
Zdziarski, A. A., Kawabata, R., & Mineshige, S. 2009, MNRAS, 299, 1633
Zimmerman, E. R., Narayan, R., McClintock, J. E., & Miller, J. M. 2005, ApJ, 618, 832

Chapter 7

Complementary work on warped-disk shadows modulating mass transfer

MNRAS **452,** 3620–3628 (2015) doi:10.1093/mnras/stv1580

Agitating mass transfer with a warped disc's shadow

H. Cambier★

Physics Department, University of California, Santa Cruz, CA 95064, USA

Accepted 2015 July 10. Received 2015 July 10; in original form 2015 April 2

ABSTRACT

For compact objects fed by Roche lobe overflow, accretion-generated X-rays irradiating the donor star can alter gas flow towards the Lagrange point thus varying mass transfer. The latest work specific to this topic consists of simple yet insightful two-dimensional hydrodynamics simulations stressing the role of global flow. To explore how a time-varying disc shadow affects mass transfer, I generalize the geometry, employ a robust hydrodynamics solver, and use phase space analysis near the nozzle to include coriolis lift there. Without even exposing the nozzle, a warped disc's shadow can drive mass transfer cycles by shifting the equatorial edges of the irradiation patches in turns: drawing in denser ambient gas before sweeping it into the nozzle. Other important effects remain missing in two-dimensional models, which I discuss along with prospects for more detailed yet efficient models.

Key words: hydrodynamics – X-rays: binaries.

1 INTRODUCTION

X-rays from accretion on to compact objects in Roche lobe overflow X-ray binaries can irradiate the donor star's envelope enough to raise surface temperatures up to factors of a few across the face of the donor. This can then affect the flow of gas towards the nozzle of the mass transfer stream at the inner Lagrange point (L1), and the mass transfer rate. Irradiation-driven enhancement was specifically invoked to explain prolonged superoutbursts in dwarf nova (DN) systems (see e.g. Hameury 2000; Smak 2000), while any net change would complicate the dividing line between transient and persistent X-ray binaries (Coriat, Fender & Dubus 2012). Because the problem is mostly interesting by connection to the accretion flow, an economical-but-sufficient model that can be integrated with more sophisticated disc models is also desirable.

The notion that X-ray irradiation may boost the total mass transfer rate, $\dot{M}_s$, dates at least as far back as Anderson (1975). In this and other early models, including Meyer & Meyer-Hofmeister (1983) and Osaki (1985), the authors assume irradiation efficiently heats gas close enough to L1. As the nozzle width, height, and pressure gradient behind it each scale roughly as the sound speed, c_s, $\dot{M}_s$ then scales with c_s and the local mass density, ρ like (Lubow & Shu 1975)

$$\dot{M}_s \sim \rho c_s^3. \qquad (1)$$

This implies a dramatic response to irradiation. However, as Anderson (1975) remarked, the accretion disc could shadow the nozzle while irradiation elsewhere could still drive flows towards the nozzle, raising $\dot{M}_s$ less dramatically.

The coriolis force then becomes important for steering gas away from or towards the nozzle as recognized by Osaki & Meyer (2003) and Smak (2004). Debate ensued how effectively it does either until Viallet & Hameury (2007, hereafter VH07), using global two-dimensional (2D) fluid simulations, resolved that coriolis forces do both during an outburst. Specifically, they solved the Euler equations on a spherical shell with irradiation and coriolis force terms mimicking those in the true Roche lobe geometry, including a disc shadow which splits irradiation into two patches, and a simple X-ray light curve for the outburst. As irradiation increased, anticyclones formed about the irradiation patches and the strong gales at the edges swept material into the nozzle until the centres of the anticyclones drifted such that the coriolis force steered more gas away. They also confirmed that the flow has ample time to cool while traversing the disc's shadow, i.e. in the disc-accretion context, irradiation affects mass transfer through influencing global weather versus directly blistering the nozzle.

For some time, Roche lobe tomography has shown that irradiation heating is also azimuthally asymmetric, e.g. Davey & Smith (1992). Most often the companions' prograde sides are warmer, consistent with additional irradiation from the stream–disc hotspot. More recently, observers can obtain maps fine enough to reveal cool patches most readily explained as star-spots, frequently including a spot sitting at the nozzle which may further suppress or affect mass transfer (see e.g. Watson et al. 2003, 2007; Hill et al. 2014).

X-ray irradiation strong enough to affect the companion can also warp the disc, and drive precession of it, e.g. Pringle (1997) and Foulkes, Haswell & Murray (2010, hereafter FHM10). This complicates the irradiation of the donor as a function of position and time, as well as the interaction between the mass transfer stream and the disc, i.e. as the warp precesses relative to the companion, more (or all) of the stream can pass the edge of the disc changing the nature of mass and angular momentum input, so variations in

★ E-mail: hcambier@ucsc.edu

© 2015 The Author
Published by Oxford University Press on behalf of the Royal Astronomical Society

$\dot{M}_s$ driven by the disc's changing shadow will affect the disc and warping in turn (see e.g. Wijers & Pringle 1999; Ogilvie & Dubus 2001).

To study the impact of a warped disc's shadow, and self-consistent hotspot irradiation in the future, motivates extending the VH07 model. I do so by using a simple and robust hydrodynamical method `AUSM-up`$^+$(Liou 2006), and relaxing the spherical grid assumption in favour of a grid fitted to the Roche lobe. In VH07, the authors also noted that the coriolis force will help lift the retrograde equatorial flow through the nozzle (or press down any prograde flow) further motivating three-dimensional (3D) simulations. Here, I partially account for this effect in 2D simulations with a sink term using 3D phase space analysis of transit orbits. This also yields initial conditions for the ballistic stream, and thus the means to derive information like the hotspot location.

In Section 2, I describe how the hydrodynamics are formulated on a Roche lobe fitting colatitude–longitude grid, and briefly review `AUSM-up`$^+$with details relegated to Section A. In Section 3, I cover the nozzle sink term; recording implementation details in Section B. I then present simulations comparing effects of geometry, sink term, boundary condition (BC), and warped-disc shadow in Section 4. I discuss these further as well important deficiencies in any 2D treatment, and suggest how economical modelling proceed in Section 5.

2 HYDRODYNAMICS ON THE (FITTED) ROCHE LOBE

The physical picture and strategy still follows VH07: irradiation deposits most of its energy within a shell of $\gtrsim$10 Thomson optical depth (also within an order of magnitude of the scaleheight) which is vertically isothermal and in hydrostatic equilibrium. VH07 then modelled fluid flow on this shell in a spherical geometry and angular coordinates.

To obtain similar equations for a 2D Roche lobe shell, I start with a Cartesian coordinate system whose origin sits at the donor's centre of mass where $\boldsymbol{x}$ points away from the 'primary', compact object, $\boldsymbol{z}$ normal to the orbital plane, and $\boldsymbol{y}$ parallel to the donor's orbital motion (Fig. 1). I denote primary mass by $M_{\rm p}$, donor mass by $M_{\rm d}$, orbital separation by a, donor-to-total mass ratio by $\mu \equiv M_{\rm d}/(M_{\rm d}+M_{\rm p})$, and barycentre–L1 distance in units of a by $k_{\rm RL}$. The sink term uses a collinear coordinate system, marked by subscripts 'cl', translated to L1, and scaled by a^{-1} (Section 3).

I define points on the critical Roche lobe equipotential surface, $\boldsymbol{r}_{\rm RL}$, through a function, $R(\theta, \phi)$:

$$\boldsymbol{r}_{\rm RL} = (x, y, z)_{\rm RL} \equiv R(\theta, \phi)\cdot(\cos\phi\sin\theta, \sin\phi\sin\theta, \cos\theta) \quad (2)$$

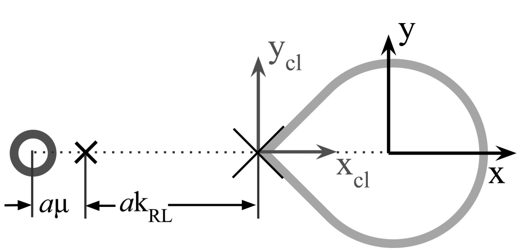

Figure 1. Default x, y, z are centred in the donor as shown while collinear coordinates $x_{\rm cl}$, $y_{\rm cl}$, $z_{\rm cl}$ are centred at L1 (large 'X'). The barycentre (small 'x') and important distances relative to it are also marked.

which I approximate by fitting Legendre polynomials to a grid of points found numerically

$$R(\theta, \phi) \leftarrow \sum_{m:\text{even}} \sum_{n} C_{mn} P_m\left(\cos\left(\theta - \frac{\pi}{2}\right)\right) P_n(\cos\phi). \quad (3)$$

Note that vertical symmetry precludes odd m. Going up to order 20 in m and n brings the 'nose' roughly within a scaleheight of L1 for the cases considered.

The metric thus takes the form

$$\begin{pmatrix} g_{\theta\theta} & g_{\theta\phi} \\ g_{\theta\phi} & g_{\phi\phi} \end{pmatrix} = \begin{pmatrix} R^2 + R_\theta^2 & R_\theta R_\phi \\ R_\theta R_\phi & R^2\sin^2\theta + R_\phi^2 \end{pmatrix} \quad (4)$$

from which follow the Christoffel symbols (Γ), transformations between linear and angular velocities, and the form of the conservation equations. In terms of the weighted stress-energy tensor $\bar{\mathcal{T}}^{\mu\nu}$ they are (e.g. Landau & Lifshitz 1975, Papadopoulos & Font 2000)

$$\bar{\mathcal{T}}^{\mu\nu}_{;\nu} = \bar{\mathcal{T}}^{\mu\nu}_{,\nu} + \Gamma^{\mu}_{\nu\alpha}\bar{\mathcal{T}}^{\nu\alpha}, \quad (5)$$

where commas and semicolons respectively denote partial and covariant derivatives.

Since this work closely follows VH07, I will also use Σ, $E_{\rm t}$, H, and P for height-integrated values of mass density, total specific energy density, enthalpy, and pressure, but I will use $\omega^\theta \equiv \dot{\theta}$ and $\omega^\phi \equiv \dot{\phi}$ for angular velocities, and M for total mass in a cell. Likewise, overbars indicate metric-weighted quantities (i.e. $\bar{\Sigma} \equiv \sqrt{g}\Sigma$). Integrating the conservation equations over $\mathrm{d}\Lambda = \mathrm{d}\theta\mathrm{d}\phi$ better conserves total mass, energy, and momenta in a cell, and for now I use the simplest discretization of multiplying cell-centred (cc) and face-centred (fc) quantities by $\Delta\Lambda = \Delta\theta\Delta\phi$ and the appropriate $\Delta\theta$ or $\Delta\phi$ (note that this does not impair conservation of mass, energy, etc. as they are exchanged between cells, but instead the accuracy of how much should be). Before discretizing the fluxes, I put them in a form that cancels to machine precision for uniform pressure using the identity

$$\sqrt{g}\cdot\left(\Gamma^{\mu}_{\alpha\beta}g^{\alpha\beta}\right) \equiv \sqrt{g}\cdot(-\partial_\nu(g^{\mu\nu}\sqrt{g})/\sqrt{g}). \quad (6)$$

The vector of conserved quantities $\boldsymbol{U}$ is then

$$(U_0, U_1, U_2, U_3) \equiv (\bar{\Sigma}, \bar{\Sigma}\omega^\theta, \bar{\Sigma}\omega^\phi, \bar{\Sigma}E_t)_{\rm cc}\cdot\Delta\Lambda$$
$$\equiv (M, M\omega^\theta, M\omega^\phi, ME_t) \quad (7)$$

which evolve according to the finite difference (square brackets) of θ- and ϕ-fluxes: $\boldsymbol{F}$ and $\boldsymbol{G}$, plus geometric and other source terms $\boldsymbol{Q}_{\rm g}$, $\boldsymbol{Q}_{\rm s}$ in the usual way

$$\partial_t\boldsymbol{U} = -[\boldsymbol{F}]_\theta - [\boldsymbol{G}]_\phi + \boldsymbol{Q}_{\rm g} + \boldsymbol{Q}_{\rm s}. \quad (8)$$

I relegate expressions for the basic terms to Section A, and describe the source terms here.

Besides mass lost to the supply stream, $\dot{M}_s(\theta, \phi)$, determined by the sink term described later, I consider a replacement flux $\dot{M}_+$ which for now adds back total mass lost and uniformly over the grid. Besides energy change due to advection (across the grid or through source/sink terms), thermal radiation, and irradiation, the gas is also radiatively heated 'from below' with temperature $T_\star$ set constant and uniform for now. Mass supplied by the source term enters with this temperature as well. Thus

$$Q_{\rm s0} = -\dot{M}_s + \dot{M}_+ \quad (9)$$

$$Q_{\rm s3} = \sigma_{\rm SB}\left(T_\star^4 + T_{\rm irr}^4 - T_g^4\right)\sqrt{g}\Delta\Lambda - \dot{M}_s E_t + \dot{M}_+\frac{k_{\rm B}T_\star}{\mu m_{\rm p}}, \quad (10)$$

where $\sigma_{\rm SB}$ is the Stefan–Boltzmann constant, $k_{\rm B}$ the Boltzmann constant, $m_{\rm p}$ the proton mass, and μ the mean molecular weight of the gas.

The coriolis force is implemented as a source term acting at cell-centres and generalizes to

$$Q_{\rm s1} = -f_{\rm cor} U_2 \sqrt{g^{\theta\theta} g^{\phi\phi}} \tag{11}$$

$$Q_{\rm s2} = +f_{\rm cor} U_1 \sqrt{g^{\theta\theta} g^{\phi\phi}}, \tag{12}$$

where $f_{\rm cor} = 2\Omega \boldsymbol{z} \cdot \boldsymbol{n}$ is the coriolis parameter, and Ω the orbital frequency.

Irradiation is treated and parametrized as in VH07: a characteristic peak irradiation temperature is defined for an area element at L1 directly facing a point source (the compact object). Elsewhere $T_{\rm irr}$ falls off with the displacement from the compact object, $\boldsymbol{r}_{\rm co} = \boldsymbol{r}_{\rm RL} - (a, 0, 0)$, as

$$T_{\rm irr} = T_{\rm irr}^{\rm max} (a - x_{\rm L1})^2 r_{\rm co}^{-3} |\boldsymbol{r}_{\rm co} \cdot \boldsymbol{n}|, \tag{13}$$

where $\boldsymbol{r}_{\rm RL} = (x_{\rm L1}, 0, 0)$ at L1.

The disc shadow is defined by converting its simpler form in the compact object's 'sky' to a function of θ and ϕ which scales $T_{\rm irr}$ by a factor 0 to 1 – softened over a tenth of a degree to smooth gradients that merely frustrate the code.

The code also includes a linear shear viscosity in the stress tensor with isotropic viscosity coefficient η (cm^{2}s^{-1}) which looks like

$$\bar{\mathfrak{Y}}^{\mu\nu} = \bar{\Sigma} \cdot \eta \left(g^{\nu\sigma} v^{\mu}_{;\sigma} + g^{\mu\rho} v^{\nu}_{;\rho} - \frac{2}{3} g^{\mu\nu} v^{\lambda}_{;\lambda} \right) \tag{14}$$

and contributes the following terms to the momentum and energy equations

$$Q_{\rm s1} = Q_{\rm s1} + \Delta\Lambda \left(\bar{\mathfrak{Y}}^{\theta\theta}_{;\theta} + \bar{\mathfrak{Y}}^{\theta\phi}_{;\phi} \right) \tag{15}$$

$$Q_{\rm s2} = Q_{\rm s2} + \Delta\Lambda \left(\bar{\mathfrak{Y}}^{\phi\theta}_{;\theta} + \bar{\mathfrak{Y}}^{\phi\phi}_{;\phi} \right) \tag{16}$$

$$Q_{\rm s3} = Q_{\rm s3} + \Delta\Lambda \left(g_{\alpha\mu} \omega^{\alpha} \bar{\mathfrak{Y}}^{\mu\nu} \right)_{;\nu}. \tag{17}$$

The derivatives are computed by simple differences and I omit the full expressions for brevity. This viscosity can be limited to instances of compression ($\omega^{\mu}_{;\mu} < 0$) and used as a more appropriate basis for artificial viscosity (see e.g. Höller et al. 2014) which I do here. To get some sense of scale, one might expect, at most, any physical viscosity to be

$$\eta \lesssim \Delta h \cdot c_{\rm s}/3 \approx (10^7\,{\rm cm})(10^6\,{\rm cm\,s^{-1}}) = 10^{13}\,{\rm cm^2\,s^{-1}}, \tag{18}$$

where Δh is the scaleheight near the nozzle. Note however, that Osaki & Meyer (2003) obtain an estimate orders of magnitude smaller by arguing that the relevant velocity is that of flow required to maintain thermal equilibrium in the lowest layers.

The hydrodynamic solver used involves computing an upwind purely advective flux and a separate pressure 'flux' between cells as functions of the flow's Mach numbers either side of the interface. This strict separation of the pressure proves convenient for geometric source terms in the non-orthogonal curvilinear coordinates considered here. Said functions are chosen to accurately approximate the subsonic regime while smoothly shifting to a modified upwind donor-cell method as the Mach number crosses unity. The method also includes a pressure diffusion term to prevent oscillations prevalent at low Mach numbers in compressible fluid solvers. The full, modified recipe of Liou (2006) is given in Section A.

3 THE POINCARÉ-SECTION AND BASIC SINK TERMS

Besides describing the Poincaré-section version of the sink term, which I'll consider the default one, I mention a simple prescription and test sink terms that will prove useful for comparisons at the end of the section.

The general steps in the sink term are: first to take some fraction, $f_{\rm s}$, of the sound speed as the normal velocity for each cell in the sink term domain, to be combined with grid ω^{θ} and ω^{ϕ} to give a 3D velocity. Resolving the nose of the donor via ever higher-order Legendre polynomials is inefficient, but using a surface deeper in the donor's gravity spuriously rejects transit trajectories, so the velocities are assigned to the same θ and ϕ on a (blunted, elliptical) nose cone that better fits the critical surface near L1. Defining this surface by a radius function, $R_{\rm nc}(\theta, \phi)$ (cf. Section B), permits straightforward transformation to Cartesian coordinates and momenta more suitable for the subsequent phase-space analysis. The latter quickly tells which cells will transfer mass, and the initial conditions for this stream.

Note that the sink term still parametrized the normal pressure gradient in this 2D setup, and it involves some complicated transformations, but these are inexpensive (many are computed once), and it automatically includes coriolis force normal to the surface. It thus provides an efficient, informative BC for this and future setups. More detail follows, and grittier details are found in Section B.

The heart of the phase space analysis dates back to work by Conley (1968) on transfer orbits in the planar-restricted three-body problem. Gómez et al. (2004) extended this to orbital itineraries, but I cite their work here for the inclusion of z-motion. The steps involved are: linearize the potential, write down corresponding equations of motion in local (and scaled) Cartesian coordinates ($x_{\rm cl}$, $y_{\rm cl}$, $z_{\rm cl}$) and associated canonical momenta ($p_{\rm xcl}$, $p_{\rm ycl}$, $p_{\rm zcl}$), and then find the eigenvectors and eigvenvalues ($q_1, q_2, q_3, p_1, p_2, p_3$). The transformation matrix components, which also indicate the sign convention, are given in equation (B3–B8). The Hamiltonian

$$h_{\rm cl} = \lambda q_1 p_1 + \frac{\nu}{2}\left(q_2^2 + p_2^2\right) + \frac{\varpi}{2}\left(q_3^2 + p_3^2\right) \tag{19}$$

in this basis, and the eigenvalues are

$$\lambda = \tfrac{1}{2}\sqrt{\rho_{\rm RL} - 2 + \sqrt{\rho_{\rm RL}(9\rho_{\rm RL} - 8)})} \tag{20}$$

$$\nu = \tfrac{1}{2}\sqrt{-\rho_{\rm RL} + 2 + \sqrt{\rho_{\rm RL}(9\rho_{\rm RL} - 8)}} \tag{21}$$

$$\varpi = \sqrt{\rho_{\rm RL}} \tag{22}$$

with

$$\rho_{\rm RL} \equiv \frac{\mu}{|k_{\rm RL} - 1 + \mu|^3} + \frac{1-\mu}{|k_{\rm RL} + \mu|^3}. \tag{23}$$

Transit trajectories can then be distinguished by positive q_1, p_1, and $0 < \mathcal{C} < 1$, where

$$\mathcal{C} \equiv h_{\rm cl}/(\lambda q_1 p_1). \tag{24}$$

The nose cone is defined by the opening horizontal ($\vartheta_{\rm h}$) and vertical ($\vartheta_{\rm v}$) angles

$$\tan\vartheta_{\rm h} = ((2\rho_{\rm RL} + 1)/(\rho_{\rm RL} - 1))^{1/2} \tag{25}$$

$$\tan\vartheta_{\rm v} = ((2\rho_{\rm RL} + 1)/\rho_{\rm RL})^{1/2} \tag{26}$$

and pushed in from L1 very slightly (cf. Section B).

Table 1. Component masses, orbital periods, stellar surface temperatures, and dimensionless nozzle scale for the cases studied.

Case	$M_{\rm p}$ ($M_\odot$)	$M_{\rm s}$ ($M_\odot$)	$P_{\rm o}$	$T_\star$ (K)	$c_{\rm s}/(a\Omega)$
GRS 1915+105	12.0	0.80	33.0 d	4500	0.039
LMC X-3	6.95	3.70	1.70 d	16 500	0.030
NS LMXB	1.40	0.50	0.20 d	4500	0.014
Dwarf Nova	0.70	0.07	1.50 h	2500	0.009

I make an extra concession here for the limited, uniform grid where the sink term 'membership' may drop to a dozen cells such that single cells joining or leaving trigger little jumps in the mass transfer rate. This certainly occurs if each cell loses

$$\dot{M}_{ij} = f_{\rm s} \cdot f_{\mathcal{C}} \cdot (\Sigma c_{\rm s}\sqrt{g}\Delta\Lambda)_{ij} \tag{27}$$

according to a simple binary condition that $f_{\mathcal{C}} = 1$ just for cells meeting the transit criteria. Based on examining typical values for $\mathcal{C}$ under various input conditions, I soften the condition to

$$f_{\mathcal{C}} \rightarrow 0.5\tanh((\mathcal{C}^{-1} - 0.35)/0.15) \tag{28}$$

which reduces the contribution of cells near the edges of the sink region, thus underestimating mass transfer.

I also consider a simpler sink prescription akin to equation (1) which estimates a scaleheight, $h_{\rm s} = c_{\rm s}/\Omega$, and total $\dot{M}_{\rm s}$ according to

$$\dot{M}_{\rm s} \approx (\Sigma/h_{\rm s})\exp\left(-\Delta h^2/h_{\rm s}^2\right)\cdot h_{\rm s}^2 \cdot (f_{\rm s}c_{\rm s}). \tag{29}$$

Specifically, I average $c_{\rm s}$ over a fixed region based on the original size of the nozzle (i.e. for $T_\star$), which then defines an effective nozzle area and drift speed to estimate $\dot{M}_{\rm s}$. This mass (and corresponding energy) is then removed from the region according to a Gaussian profile.

A 'velocity-ignorant' version of the full sink term that ignores the tangential grid velocities, and a 'tally-only' version that computes mass-loss as normal but does not remove it will also prove useful. In all cases, I also limit mass-loss per cell to one-tenth the contained mass.

4 SIMULATIONS AND RESULTS

The model is coded in CUDA C++ (5.0) to parallelize computations using the graphics card, which in this case was an NVIDIA GeForce GT 650M.

Given the simple colatitude–longitude grid, the simulation domain fully covers ϕ using a periodic BC, but must exclude the poles, and so I cut it off at values of ± 0.90 in $\cos\theta$. The default θ-BC is reflection, which I also compare to an outflow BC below. In warped-disc simulations the grid size is 384×768 in θ and ϕ while the earlier test cases had slightly smaller 352×704 grids. The default η is 2×10^{13} cm^2 s^{-1}, which chiefly serves to dampen vortices at high latitudes, but note that this value is fairly large (Section 2).

The simulations cover four model systems: two represent the luminous and persistent black hole X-ray binaries (BHXRBs) GRS 1915+105 (Eikenberry & Bandyopadhyay 2000; Reid et al. 2014) and LMC X-3 (Orosz et al. 2014), one is the 'generic' neutron star low-mass X-ray binary (NS LMXB) of Wijers & Pringle (1999), and one represents a DN based on 'model 1' of VH07. Table 1 lists the system parameters, including the dimensionless nozzle size. The grid and BC tests use the DN parameters while evolving-shadow simulations focus on the others, and especially the GRS 1915+105

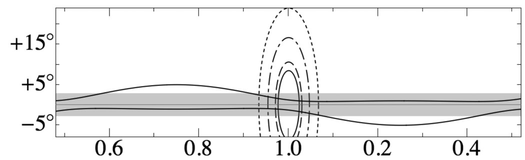

Figure 2. A portion of the primary's sky in degrees above/below the orbital plane and azimuthal angle showing the extent of the plain disc (shaded band), warped disc (solid curves), and extent of the companion for companion (ellipses), where solid, dashed, dot–dashed and dotted correspond respectively to the GRS 1915+105, DN, LMC X-3, and NS LMXB cases.

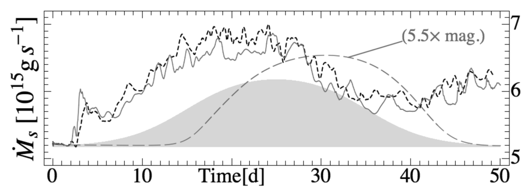

Figure 3. $\dot{M}_{\rm s}$ on the Roche lobe (dashed) and spherical (solid) grids evolve nearly identically – the grey hump and long dashed curves show the shape of the irradiation profile, and a magnified view of an earlier trial run with high-η for reference.

proxy as its properties prove conducive to strong irradiation-driven variability.

Spatially and temporally, the default maximum $T_{\rm irr}$ is set to 10^4K. The default shadow extends 2.°75 above and below the orbital plane in the compact object's sky, while the warped-disc shadows are made to resemble results of smoothed-particle-hydrodynamics simulations by FHM10 as shown in Fig. 2. These shapes are projected on to the companion's surface, and scrolled across it with a period, $P_{\rm w}$, for the warped-disc runs, which is given by the synodic period between the orbital and the precession periods (in the inertial frame). Because the latter is typically several times larger, I set $P_{\rm w} = P_{\rm o}$ except for GRS 1915+105 where I set $P_{\rm w} = 24.8$d.

Before exploring irradiation under a moving shadow, I compare spherical versus Roche lobe grid geometry, and reflection versus outflow BCs.

4.1 Grid geometry comparison

For comparing grid geometries the same Roche lobe coriolis force as a function of θ and ϕ is used, but all other grid properties for the spherical star are recalculated for a sphere with the same grid area. The simplified sink term is used for both grids. Here, I turned irradiation up and down over the first 40 d following a smooth pulse profile shown in Fig. 3 along with the results. In both cases, overall evolution is quite similar: irradiation drives enhancement of $\dot{M}_{\rm s}$, and afterwards a systematic increase of $\dot{M}_{\rm s}$ persists due to established

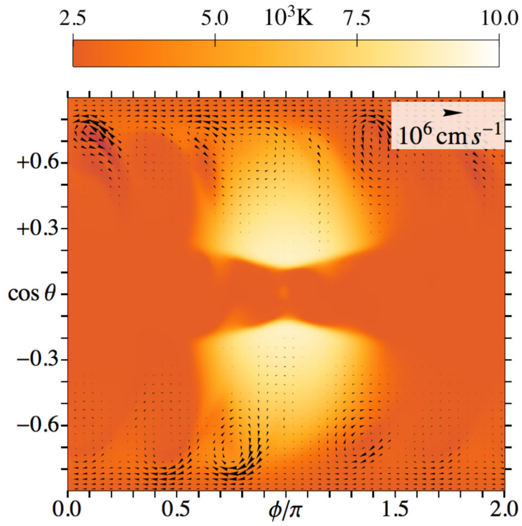

Figure 4. Temperature and velocity map of the full grid 25 d into the Roche lobe test showing the anticyclones formed near the poles which drive fluctuations that can survive as far as nozzle.

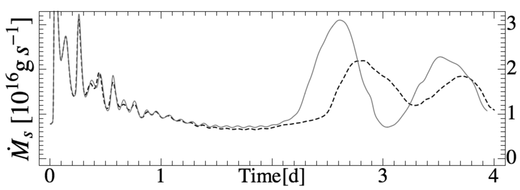

Figure 5. Simulations subject to immediate and intense (10^4 K) irradiation with outflow (dotted) and reflection (solid) BCs initially show little difference in $\dot{M}_{\mathrm{s}}$, but differences at the poles influence the nozzle within a few days.

flow towards the sink and throughout the grid. An early (Roche lobe grid) trial with subdued $\dot{M}_{\mathrm{s}}$ and even higher η (1×10^{14} cm^2 s^{-1}) gave a smooth response that decayed after irradiation, but with a stronger sink in a highly turbulent flow and a replenishment condition for $\dot{M}_{\mathrm{s}}$, the comparison runs may take much longer to decay, or have entered a positive feedback loop. Differences between each case are comparable to fluctuations inherent to each. Fig. 4 shows anticyclonic formation near peak $\dot{M}_{\mathrm{s}}$ in the Roche lobe grid run. Even higher values of η subdue them and their effects on $\dot{M}_{\mathrm{s}}$.

4.2 BC comparison

To compare polar BCs, I employed the Roche lobe grid, fully-detailed sink term, and immediately turned on irradiation with peak T_{irr} of 10^4 K to quickly reveal the maximal extent of the BC's influence. The two cases evolve almost identically for a couple of days (including strong oscillations due to the intense initial conditions) before differences near the poles finally reach the nozzle. Variation in $\dot{M}_{\mathrm{s}}$ still remains similar in structure and magnitude, though the timing of extrema in mass transfer shifts (Fig. 5).

4.3 Warped-disc shadow runs

As noted, the GRS 1915+105 case proves most susceptible to irradiation-driven variability in $\dot{M}_{\mathrm{s}}$, largely due to a thick shadow, long orbital period, and low surface temperature as made clear later. Motivated by the large amplitudes seen in $\dot{M}_{\mathrm{s}}$, I also ran this case with a large variety of sink terms, and Fig. 6 shows the resulting $\dot{M}_{\mathrm{s}}$. This case also demonstrates the mechanics of the warped-disc shadow driving $\dot{M}_{\mathrm{s}}$ most dramatically. Fig. 7 shows maps of temperature plus velocity, and density plus mass flux sampling such a cycle (times marked in Fig. 6), and walking through it helps to understand the $\dot{M}_{\mathrm{s}}$ curves.

The irradiation patches quickly evolve towards lower density to maintain pressure equilibrium with the cooler surrounding gas. When the warped shadow starts obscuring the equatorial end of one irradiation patch, ambient gas pours in. As that side of the shadow later retreats back towards the equator, the pressure gradient at the edge of the patch sweeps gas towards the nozzle where it squeezed against the edge of the idle patch, and forced out the nozzle or along the equator. The other patch does not linger long though, so $\dot{M}_{\mathrm{s}}$ promptly drops.

Unsurprisingly, the full sink term yields higher peak amplitudes than the velocity-ignorant one, but the latter also tends to give lower $\dot{M}_{\mathrm{s}}$ minima, i.e. lift appears to compensate slightly for the reduced densities during minima. The simple sink term yields less variation still, and misses the bumps in $\dot{M}_{\mathrm{s}}$ preceding major maxima, when the shadow is actually thinnest, and squeezes gas already at the nozzle before the bulk of swept gas reaches it. Slower, less regular modulation still occurs when I apply the same illumination profile without rotating the shadow. Sloshing of the equatorial jetstream

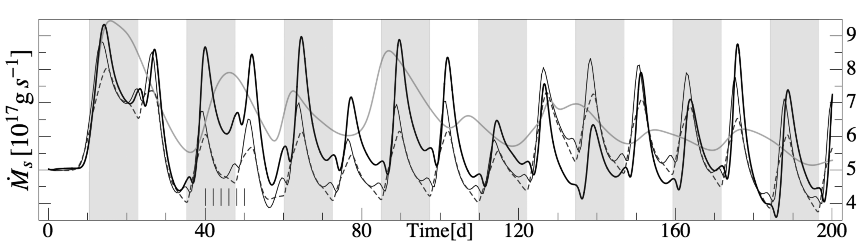

Figure 6. Runs for GRS 1915 parameters with default and velocity-ignorant sinks are shown by solid and dashed curves. The simple sink gives the similar thin curve, and the decaying grey curve with slower modulation comes from a precession-free run. The tally-only sink term gave $\dot{M}_{\mathrm{s}}$ within 1 per cent of the default sink term for 40 d, and is not plotted. The alternating grey/white bands show halves of P_{w} – the shadow is thinnest between them – and the ticks at 40 d onwards show snapshot times of Fig. 7.

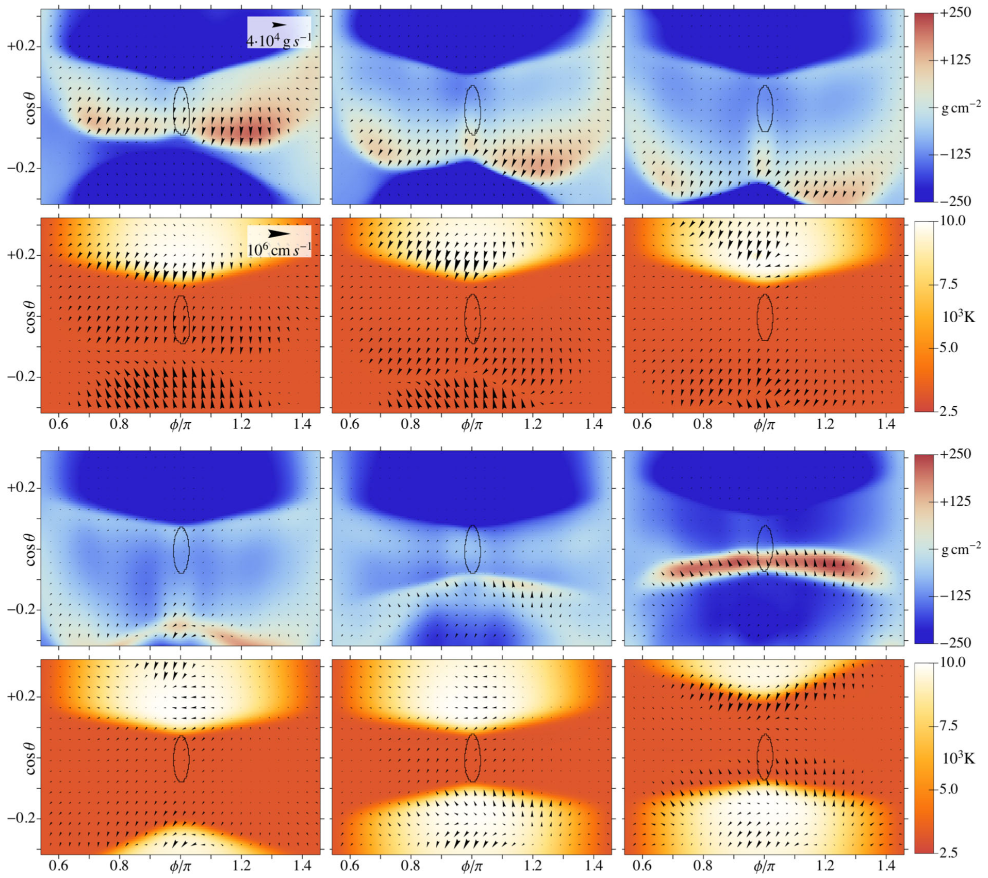

Figure 7. Top panels in each row show mass change and cell-mass fluxes, and bottom panels show temperature and velocities for a cycle in the GRS 1915+105 case with the full sink term whose cells are outlined by the oval. Fig. 6 shows snapshot times. See text for discussion.

drives density variations at roughly 100 d for a nearly-sonic flow, while smaller weather patterns drive modulation on shorter timescales.

The relatively long orbital period, i.e. weak coriolis force, and thick shadow aid the process by allowing more gas to pile up at the edge of the returning irradiation boundary. The thicker shadow and motion of the irradiation edges at higher latitudes also tie the process more closely to the global flow including anticyclonic activity near the poles. The value of $T_\star$ in this case allows irradiation to have a significant effect.

By contrast, $T_\star$ for the LMC X-3 model is almost sufficient to eliminate irradiation's influence. Fig. 8 shows $\dot{M}_{\rm s}$ settling into regular but weak cycles for the full and simple sink terms. The simple estimate is systematically offset and noticeably so against such small variations in $\dot{M}_{\rm s}$, but modulation amplitudes for each version are closer to each other than in GRS 1915+105.

Simulations for the neutron star case also produce $\dot{M}_{\rm s}$-cycles as shown in Fig. 9, and explore the combination of thin shadow and cooler star in a physically motivated situation. Using either the full or simple sink term returns similar $\dot{M}_{\rm s}$-curves, and like the LMC X-3 curves, they lack the 'substructure' of the GRS 1915+105 case.

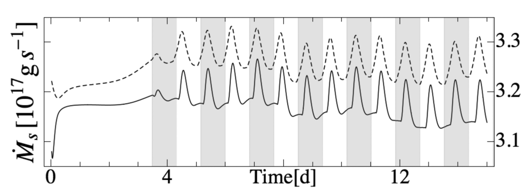

Figure 8. Runs with the full and basic sink terms are shown by solid and dashed curves. Again, shaded bands show halves of $P_{\rm w}$.

For the DN case, I show results of a cursory run using the default sink term in Fig. 10. Relative variability appears to be comparable or greater to the other cases except the GRS 1915+105 proxy, and the light curves for individual cycles show the same bump as those in GRS 1915+105. Of all the cases, the DN one places the most stress on the assumptions: the irradiation source is the least point-like, and the short orbital period quickly ties conditions near the sink to the global flow and regions where the vertical structure further differs from the irradiated layer around the nozzle.

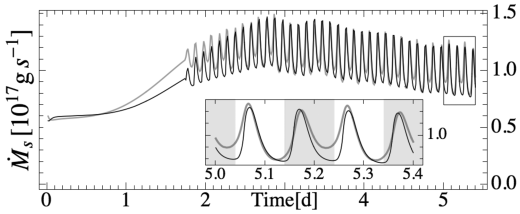

Figure 9. NS LMXB runs using full (black) and crude (thick, grey) sink term where the cycles versus precession phase are shown in the inset.

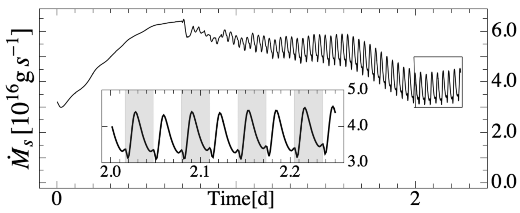

Figure 10. A run for the DN case using the full sink term, with inset magnifying cycles versus precession phase.

Since many direct effects or signs of the cycles will involve the stream–disc interaction, I integrate sink term trajectory data (post-simulation) until the trajectories cross twice the circularization radius,

$$2R_{\rm circ} = 2ak_{\rm RL}^4/(1-\mu_{\rm RL}). \tag{30}$$

Fig. 11 shows the $\dot{M}_{\rm s}$-weighted mean and vertical spread in terms of ± 2 standard deviations – all are nearly stationary in terms of azimuthal phase relative to the donor. Note these only offer a rough, comparative sense of the interaction. The computation is purely ballistic, for example the spread shown in GRS 1915+105 is roughly 3/4 that predicted by the fitting formulae in Hessman (1999). The stream is also sampled by progressively fewer sinks cells: from GRS 1915+105 ($\gtrsim$20) through the DN case ($\sim$10). Bouts of north/south flow near the nozzle, coinciding with high-$\dot{M}_{\rm s}$ lead to very slight vertical shifts, which may exaggerate overflow (Section 5).

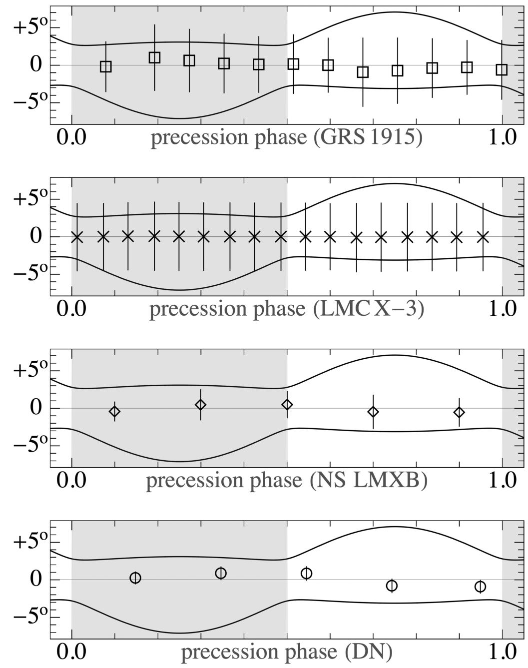

Figure 11. View from the compact object of the stream-impact centroid and angular extent above/below the plane versus phase relative to the warped-disc sampling each of the simulated cases. Shaded bands match the convention in $\dot{M}_{\rm s}$-plots.

5 DISCUSSION

The warped-shadow simulations each show the shadow driving mass transfer cycles using the irradiation patch boundaries like piston heads; gas pours in as they retreat, and is then compressed through the nozzle. Greater shadow extent, up to some degree, is conducive both to higher amplitude modulation, and less regularity as background flow (e.g. weather) can also interfere more easily. The grid and BC comparisons show that the spherical grid with Roche lobe driving terms mimics the Roche lobe within variability due to vortices intrinsic to each, while the differences between reflecting outflow polar BCs appear more systematic, i.e. unambiguous study of cases like the GRS 1915+105 one ideally use full grid coverage, but strongly-driven variability in the vicinity of the nozzle is not likely sensitive to this difference.

Modulation in $\dot{M}_{\rm s}$ at nearly twice the orbital frequency should directly vary the stream–disc hotspot luminosity. However, this may be hard to detect or distinguish from other processes, including the requisite warped disc.

For eclipsing systems, even if half of the hotspot luminosity is hidden from view, any offset between $P_{\rm o}$ and $P_{\rm w}$ should lead to variation from eclipse to eclipse, as seen for instance by Bąkowska & Olech (2014) for HT Cassiopeia. However, the disc in this and other systems with $M_s/M_p \lesssim 0.25$, can stretch and undergo apsidal precession in the potential due to tidal forcing (e.g. Lubow 1991, Wood et al. 2011), and this may also account for such variation (e.g. Rolfe, Haswell & Patterson 2001). Furthermore, Foulkes et al. (2004) find that dissipation in the outer radii of such discs may even peak twice per orbital period (though less symmetrically than in the cycles here).

The warped, tilted disc necessary for $\dot{M}_{\rm s}$-cycles can also drive modulation at twice the orbital frequency by letting the stream strike deeper disc radii as noted before (FHM10), by changing illumination of the donor, etc. FHM10 predict varying stream penetration to produce a square-wave-like signal (their fig. 5) relative to the sharp changes in $\dot{M}_{\rm s}$ found here which would effectively multiply the former, and substantially so in cases like the GRS 1915+105 one.

The fine details of the stream–disc interaction imply some subtle, and perhaps more important, consequences of the cycles. As part of their study on stream–disc interactions, Kunze, Speith & Hessman (2001) considered a burst in $\dot{M}_{\rm s}$, from 10^{-10} to 10^{-9} M$_\odot$ yr^{-1} for a CV system, and saw the stream deposit gas further inwards and more evenly. Since the cycles here both drop and raise $\dot{M}_{\rm s}$ above its 'idle' value, the net effect is unclear without knowing more about the hotspot's response to $\dot{M}_{\rm s}$ changes, e.g. would the cycles amplify, or offset the effect of stream penetration depositing mass further inwards?

Kunze et al. also find that the hotspot is not as 'tall' for $\dot{M}_s$-bursts, but more of the overflowing stream bounces and strikes the disc again. This would cause absorption dips at unusual phase (i.e. from the second stream–disc interaction when the donor is behind the primary), that are more prevalent when the donor is irradiated. In principle, this provides a means beyond optical or infrared observations to detect the cycles, but the authors found such dips would be limited to inclinations above 70° in this case which limits its usefulness for BHXRBs.

Despite largely accounting for coriolis lift near the nozzle, plenty of 3D physics remains to be tested, and most likely included, to understand the problem. Chief among these are magnetohydrodynamic (MHD) effects. For instance, Rogers & Komacek (2014) simulated flow in the atmospheres of hot-Jupiters and for their high-temperature cases of relevance here, they found that the induced magnetic field profile could exert sufficient tension back on the gas at high altitudes to reverse the flow direction. In the present context, if this effect reversed the predominant equatorial jet direction at high altitudes, then the coriolis force would predominantly pin down gas at the nozzle instead of lifting it. Xisto, Páscoa & Oliveira (2014) have recently extended `AUSM-up`$^+$to MHD so this element of the present method may carry over to future work.

Even barring magnetic effects, 3D treatment would permit more carefully defining the envelope, resolving flow normal to the surface, and unambiguous inclusion of gravity-darkening. At the very least, the latter will likely increase mass transfer systematically (by decreasing standard temperatures near the nozzle relative to irradiation temperature). More generally still, the entire surface can and should be covered by the grid to eliminate ambiguities due to polar BCs, and even static mesh refinement near the nozzle would help greatly.

Exploratory simulations using existing MHD codes fully covering just an ordinary sphere with relevant driving terms (in the spirit of VH07) are warranted, and might resolve whether some mechanism suppresses the cycles in general, if they are much weaker in DN systems than predicted here, or if they are simply difficult to detect or identify. Meanwhile, it appears possible to modify these, or use them to inform, a global yet computationally-inexpensive models of the donor that can be integrated with disc and emission models.

ACKNOWLEDGEMENTS

I thank my advisor, David M. Smith, for encouragement to pursue this project, and gratefully acknowledge a UCSC departmental grant that made it feasible to do so. Also, a detailed review and suggestions by the referee, Dr Jean-Marie Hameury, substantially improved the paper. This research has made use of NASA's Astrophysics Data System Bibliographic Services.

REFERENCES

Anderson L., 1975, ApJ, 202, 232
Bąkowska K., Olech A., 2014, Acta Astron., 64, 247
Conley C., 1968, SIAM J. Appl. Math, 16, 732
Coriat M., Fender R. P., Dubus G., 2012, MNRAS, 424, 1991
Davey S., Smith R. C., 1992, MNRAS, 257, 476
Eikenberry S. S., Bandyopadhyay R. M., 2000, ApJ, 545, L131
Foulkes S. B., Haswell C. A., Murray J. R., Rolfe D. J., 2004, MNRAS, 349, 1179
Foulkes S. B., Haswell C. A., Murray J. R., 2010, MNRAS, 401, 1275 (FHM10)
Gómez Koon W. S., Lo M. W., Marsden J. E., Masdemont J., Ross S. D., 2004, Nonlinearity, 17, 1571
Hameury J.-M., 2000, New Astron. Rev., 44, 15
Hessman F. V., 1999, ApJ, 510, 867
Hill C. A., Watson C. A., Shahbaz T., Steeghs D., Dhillon V. S., 2014, MNRAS, 444, 192
Höller H., Koskela A., Dorfi E., Benger W., 2014, Comput. Astrophys. Cosmol., 1, 2
Kunze S., Speith R., Hessman F. V., 2001, MNRAS, 322, 499
Landau L. D., Lifshitz E. M., 1975, The Classical Theory of Fields. Oxford Univ. Press, Oxford
Liou M.-S., 2006, J. Comput. Phys., 214, 137
Lubow S. H., 1991, ApJ, 381, 259
Lubow S. H., Shu F. H., 1975, ApJ, 198, 383
Meyer F., Meyer-Hofmeister E., 1983, A&A, 121, 29
Ogilvie G. I., Dubus G., 2001, MNRAS, 320, 485
Orosz J. A., Steiner J. F., McClintock J. E., Buxton M. M., Bailyn C. D., Steeghs D., Guberman A., Torres M. A. P., 2014, ApJ, 794, 154
Osaki Y., 1985, A&A, 144, 369
Osaki Y., Meyer F., 2003, A&A, 401, 325
Papadopoulos P., Font J. A., 2000, Phys. Rev. D, 61, 024015
Pringle J. E., 1997, MNRAS, 292, 136
Reid M. J., McClintock J. E., Steiner J. F., Steeghs D., Remillard R. A., Dhawan V., Narayan R., 2014, ApJ, 796, 2
Rogers T. M., Komacek T. D., 2014, ApJ, 794, 132
Rolfe D. J., Haswell C. A., Patterson J., 2001, MNRAS, 324, 529
Smak J., 2000, New Astron. Rev., 44, 171
Smak J., 2004, Acta. Astron., 54, 181
Viallet M., Hameury J.-M., 2007, A&A, 475, 597 (VH07)
Watson C. A., Dhillon V. S., Rutten R. G. M., Schwope A. D., 2003, MNRAS, 341, 129
Watson C. A., Steeghs D., Shahbaz T., Dhillon V. S., 2007, MNRAS, 382, 1105
Wijers R. A. M. J., Pringle J. E., 1999, MNRAS, 308, 207
Wood M. A., Still M. D., Howell S. B., Cannizzo J. K., Smale A. P., 2011, ApJ, 741, 105
Xisto C. M., Páscoa J. C., Oliveira P. J., 2014, J. Comput. Phys., 275, 323

APPENDIX A: HYDRODYNAMICS DETAILS

The components of $\boldsymbol{F}$ for the `AUSM-up`$^+$scheme and chosen discretization read

$$F_0 = \left(\left(\mathcal{M}_{\mathrm{sI}}\omega_{\mathrm{sI}}^{\theta}\right)_{\mathrm{fc}}(U_0/\Delta\Lambda)_{\pm}\right)\Delta\phi \tag{A1}$$

$$F_1 = \left(\left(\mathcal{M}_{\mathrm{sI}}\omega_{\mathrm{sI}}^{\theta}\right)_{\mathrm{fc}}(U_1/\Delta\Lambda)_{\pm}\right)\Delta\phi + (\mathcal{P}_{\mathrm{sI}}\sqrt{g}g^{\theta\theta})_{\mathrm{fc}} \tag{A2}$$

$$F_2 = \left(\left(\mathcal{M}_{\mathrm{sI}}\omega_{\mathrm{sI}}^{\theta}\right)_{\mathrm{fc}}(U_2/\Delta\Lambda)_{\pm}\right)\Delta\phi + (\mathcal{P}_{\mathrm{sI}}\sqrt{g}g^{\theta\phi})_{\mathrm{fc}} \tag{A3}$$

$$F_3 = \left(\left(\mathcal{M}_{\mathrm{sI}}\omega_{\mathrm{sI}}^{\theta}\right)_{\mathrm{fc}}(U_0 H_t/\Delta\Lambda)_{\pm}\right)\Delta\phi, \tag{A4}$$

where $\pm$ subscripts denote up-winding, and $\mathcal{M}_{\mathrm{sI}}$, ω_{sI}, and $\mathcal{P}_{\mathrm{sI}}$ are numerical interface Mach numbers, sound speeds, and pressures described below. Swapping one upper θ index in each term with ϕ, and $\Delta\phi$ with $\Delta\theta$ gives the form of $\boldsymbol{G}$. The geometric source terms read

$$Q_{\mathrm{g}1} = P_{\mathrm{cc}}\left(\Delta\phi\left[(g^{\theta\theta}\sqrt{g})_{\mathrm{fc}}\right]_{\theta} + \Delta\theta\left[(g^{\theta\phi}\sqrt{g})_{\mathrm{cf}}\right]_{\phi}\right) - U_0\left(\Gamma^{\theta}_{\beta\gamma}\omega^{\beta}\omega^{\gamma}\right)_{\mathrm{cc}} \tag{A5}$$

$$Q_{\mathrm{g}2} = P_{\mathrm{cc}}\left(\Delta\phi\left[(g^{\theta\phi}\sqrt{g})_{\mathrm{fc}}\right]_{\theta} + \Delta\theta\left[(g^{\phi\phi}\sqrt{g})_{\mathrm{cf}}\right]_{\phi}\right) - U_0\left(\Gamma^{\phi}_{\beta\gamma}\omega^{\beta}\omega^{\gamma}\right)_{\mathrm{cc}}, \tag{A6}$$

where repeated indices imply summation as usual.

Chapter 8

Summary and future work

Black hole X-ray binaries exhibit both a wide variety of intensity patterns, and corresponding spectral evolution cycles that must be tuneable (i.e. repeatable but not fixed within a system let alone between them). This includes variability on timescales $\sim$100d that points to significant changes occurring within the accretion flow at $\sim$100-1000 R_{S} which lack definitive explanation. This has important implications for the physics of the flow, and frustrates models based on transient BHXRBs alone and too inflexible in their spectral evolution.

Two-phase accretion flow involving evaporation-condensation between a cooler disk and hotter halo combines well-motivated assumptions with well-understood physics to provide a predictive model that can explain hysteresis in transient BHXRBs, and is even qualitatively promising for explaining hysteresis in persistent BHXRBs. Observations indicating more variable disk truncation suggest the model is at least slightly incomplete. However, such models also predict sustained correlated disk and power-law emission at high (but still sub-Eddington) luminosities, which is not observed. Some neglected effects may conceivably address these problems, or the underlying assumption of an independently-accreting corona flow may be wrong.

Difficulties with constant-α models in general strongly motivates looking for more intrinsic causes of accretion variability such as density and temperature dependence of α through non-ideal MHD effects on the MRI. If the effective diffusivity at large scales and magnetic field strengths is able to reduce α, or if the Potter & Balbus (2014) criterion for α-quenching still holds, then this may at least help account for sawtooth luminosity cycles in persistent BHXRBs without enforcing a particular type of spectral hysteresis or contradicting transient BHXRB cycles.

Strong observational evidence for magnetically-driven outflows exists. They have the potential to resolve the issue of how to cool and prevent the disk from undergoing the radiation pressure instability, and their presence may signal stalled disk accretion. It remains unclear what the exact conditions behind wind launching are, or whether it can be modeled as a function of local disk state in the kind of one-dimensional model used here. Thus, I described in Ch. 3.3 how to implement a simple wind model. As low disk-α may facilitate wind-launching, this may prove an interesting topic if the case for α-branching grows stronger.

Likewise, transport of magnetic flux through the disk may be amenable to 1D implementation, and may explain the tuneable nature of hysteresis if it triggers a specific spectral state, and variously "wins" or "loses" a race with mass transport depending on the details of the flow. Tests of other mechanisms even point to migrating flux raising α as a potential solution (e.g. Ch. 5.2.3), for which I also prepared a simple implementation described in Ch. 4.4 as a basis for future work.

More generally, the method might be further improved by including time evolution of angular momentum and energy. For the latter, tabulation could be replaced with direct computation once searching over models is no longer the primary concern, or perhaps tabulating in a more general surplus heating/cooling parameter that could be related to irradiation, advection, etc. so long as they don't depend in a detailed way on local properties.

So long as accretion flows can be factorized into local microphysics coupled by simple transport processes (i.e. mass, energy, magnetic flux, etc.) with small changes in geometry, the kind of modeling performed here can remain a useful tool. Ultimately though, more detailed and direct simulations must test, and inform such simple models, and real flows may defy such simple factorization.

Bibliography

Abe, Y., Fukazawa, Y., Kubota, A., Kasama, D., & Makishima, K. 2005, PASJ, 57, 629

Abramowicz, M., Brandenburg, A., & Lasota, J.-P. 1996, MNRAS, 281, L21

Abramowicz, M. A., Czerny, B., Lasota, J. P., & Szuszkiewicz, E. 1988, ApJ, 332, 646

Allured, R., Tomsick, J. A., Kaaret, P., & Yamaoka, K. 2013, ApJ, 774, 135

Altamirano, D., Belloni, T., Linares, M., et al. 2011, ApJL, 742, L17

Anderson, L. 1975, ApJ, 202, 232

Augusteijn, T., Kuulkers, E., & van Kerkwijk, M. H. 2001, A&A, 375, 447

Bai, X.-N., & Stone, J. M. 2013a, ApJ, 767, 30

—. 2013b, ApJ, 769, 76

Balbus, S. A., & Hawley, J. F. 1998, Rev. Mod. Phys., 70, 1

Balbus, S. A., & Henri, P. 2008, ApJ, 674, 408

Balbus, S. A., & McKee, C. F. 1982, ApJ, 252, 529

Bale, S. D., Pulupa, M., Salem, C., Chen, C. H. K., & Quataert, E. 2013, ApJL, 769, L22

Bardeen, J. M., & Petterson, J. A. 1975, ApJL, 195, L65

Begelman, M. C. 2002, ApJL, 568, L97

Begelman, M. C., & Armitage, P. J. 2014, ApJL, 782, L18

Begelman, M. C., McKee, C. F., & Shields, G. A. 1983, ApJ, 271, 70

Belloni, T. M., Sanna, A., & Méndez, M. 2012, MNRAS, 426, 1701

Bjoernsson, G., Abramowicz, M. A., Chen, X., & Lasota, J.-P. 1996, ApJ, 467, 99

Blaes, O. M. 2004, in Accretion Discs, Jets and High Energy Phenomena in Astrophysics, ed. V. Beskin, G. Henri, F. Menard, & et al., 137

Blandford, R., & Payne, D. 1982, MNRAS, 199, 883

Bradley, C. K., & Frank, J. 2009, ApJ, 704, 25

Cambier, H. 2015, MNRAS, 452, 3620

Cambier, H. J., & Smith, D. M. 2013, ApJ, 767, 46

Casares, J., & Jonker, P. G. 2014, SSR, 183, 223

Caunt, S. E., & Tagger, M. 2001, A&A, 367, 1095

Chakrabarti, S., & Titarchuk, L. G. 1995, ApJ, 455, 623

Chartas, G., Kochanek, C. S., Dai, X., et al. 2012, ApJ, 757, 137

Coriat, M., Fender, R. P., & Dubus, G. 2012, MNRAS, 424, 1991

Dexter, J., & Blaes, O. 2014, MNRAS, 438, 3352

Done, C., Gierliński, M., & Kubota, A. 2007, A&AR, 15, 1

Esin, A. A., McClintock, J. E., & Narayan, R. 1997, ApJ, 489, 865

Ferguson, J. W., Alexander, D. R., Allard, F., et al. 2005, ApJ, 623, 585

Foulkes, S. B., Haswell, C. A., & Murray, J. R. 2010, MNRAS, 401, 1275

Frank, J., King, A., & Raine, D. 2002, Accretion Power in Astrophysics, 3rd edn. (Cambridge)

Frank, J., King, A. R., & Lasota, J.-P. 1987, A&A, 178, 137

Fromang, S., Latter, H., Lesur, G., & Ogilvie, G. I. 2013, A&A, 552, A71

Galeev, A., Rosner, R., & Vaiana, G. 1979, ApJ, 229, 318

Genzel, R., Eisenhauer, F., & Gillessen, S. 2010, Reviews of Modern Physics, 82, 3121

Ghez, A. M., Salim, S., Hornstein, S. D., et al. 2005, ApJ, 620, 744

Guilet, J., & Ogilvie, G. I. 2012, MNRAS, 424, 2097

Hannikainen, D., Sault, B., Kuulkers, E., et al. 2002, The Astronomer's Telegram, 108, 1

Hirose, S., Blaes, O., Krolik, J. H., Coleman, M. S. B., & Sano, T. 2014, ArXiv e-prints, arXiv:1403.3096 [astro-ph.HE]

Hjellming, R. M., Rupen, M. P., Mioduszewski, A. J., et al. 1999, ApJ, 514, 383

Ichimaru, S. 1977, ApJ, 214, 840

Iglesias, C. A., & Rogers, F. J. 1996, ApJ, 464, 943

Io, Y., & Suzuki, T. K. 2014, ApJ, 780, 46

Janiuk, A., Czerny, B., & Siemiginowska, A. 2002, ApJ, 576, 908

Jones, C., Forman, W., Tananbaum, H., & Turner, M. J. L. 1976, ApJL, 210, L9

Kallman, T. R., Bautista, M. A., Goriely, S., et al. 2009, ApJ, 701, 865

King, A. L., Walton, D. J., Miller, J. M., et al. 2014, ApJL, 784, L2

Knigge, C. 1999, MNRAS, 309, 409

Krumholz, M. R., & Forbes, J. C. 2014, ArXiv e-prints, arXiv:1406.6691 [astro-ph.IM]

Kubota, A., & Makishima, K. 2004, ApJ, 601, 428

Kubota, A., Makishima, K., & Ebisawa, K. 2001, ApJL, 560, L147

Kubota, A., Dotani, T., Cottam, J., et al. 2007, PASJ, 59, 185

Kunze, S., Speith, R., & Hessman, F. V. 2001, MNRAS, 322, 499

Kuulkers, E., Wijnands, R., Belloni, T., et al. 1998, ApJ, 494, 753

Lamb, F. K. 2003, in Astronomical Society of the Pacific Conference Series, Vol. 308, From X-ray Binaries to Gamma-Ray Bursts: Jan van Paradijs Memorial Symposium, ed. E. P. van den Heuvel, L. Kaper, E. Rol, & R. A. M. J. Wijers, 221

Larwood, J. 1998, MNRAS, 299, L32

Larwood, J. D., Nelson, R. P., Papaloizou, J. C. B., & Terquem, C. 1996, MNRAS, 282, 597

Lasota, J.-P. 2001, NAR, 45, 449

Lesur, G., & Longaretti, P.-Y. 2007, MNRAS, 378, 1471

—. 2009, A&A, 504, 309

Li, S.-L., & Begelman, M. C. 2014, ApJ, 786, 6

Lightman, A. P., & Eardley, D. M. 1974, ApJL, 187, L1

Liu, B. F., Mineshige, S., & Shibata, K. 2002, ApJL, 572, L173

Liu, B. F., Taam, R. E., Meyer-Hofmeister, E., & Meyer, F. 2007, ApJ, 671, 695

Liu, J. Y., Liu, B. F., Qiao, E. L., & Mineshige, S. 2012, ApJ, 754, 81

Lubow, S. H. 1992, ApJ, 398, 525

Lubow, S. H., Papaloizou, J. C. B., & Pringle, J. E. 1994, MNRAS, 267, 235

Lynden-Bell, D., & Pringle, J. E. 1974, MNRAS, 603

Main, D. S., Smith, D. M., Heindl, W. A., et al. 1999, ApJ, 525, 901

Maloney, P. R., Begelman, M. C., & Nowak, M. A. 1998, ApJ, 504, 77

Maloney, P. R., Begelman, M. C., & Pringle, J. E. 1996, ApJ, 472, 582

Mayer, M., & Pringle, J. E. 2007, MNRAS, 376, 435

Meyer, F., Liu, B. F., & Meyer-Hofmeister, E. 2007, A&A, 463, 1

Meyer, F., & Meyer-Hofmeister, E. 1994, A&A, 288, 175

Miller, C., & Colbert, E. J. M. 2004, International Journal of Modern Physics D, 13, 1

Miller, J. M., Homan, J., Steeghs, D., et al. 2006a, ApJ, 653, 525

Miller, J. M., Raymond, J., Fabian, A., et al. 2006b, Nature, 441, 953

Miller, J. M., Raymond, J., Reynolds, C. S., et al. 2008, ApJ, 680, 1359

Miller, J. M., Raymond, J., Fabian, A. C., et al. 2004, ApJ, 601, 450

Miyamoto, S., Kitamoto, S., Hayashida, K., & Egoshi, W. 1995, ApJL, 442, L13

Montgomery, M., & Martin, E. 2010, ApJ, 722, 989

Motta, S. E., Belloni, T. M., Stella, L., Muñoz-Darias, T., & Fender, R. 2014a, MNRAS, 437, 2554

Motta, S. E., Muñoz-Darias, T., Sanna, A., et al. 2014b, MNRAS, 439, L65

Muñoz-Arjonilla, A. J., Martí, J., Luque-Escamilla, P. L., et al. 2010, A&A, 519, A15

Muñoz-Darias, T., Casares, J., & Martínez-Pais, I. G. 2008, MNRAS, 385, 2205

Muñoz-Darias, T., Coriat, M., Plant, D. S., et al. 2013, MNRAS, 432, 1330

Muñoz-Darias, T., Fender, R. P., Motta, S. E., & Belloni, T. M. 2014, MNRAS, 443, 3270

Narayan, R., & McClintock, J. E. 2005, ApJ, 623, 1017

Narayan, R., & Yi, I. 1995, ApJ, 444, 231

Nauman, F., & Blackman, E. G. 2014, ArXiv e-prints, arXiv:1409.2442 [astro-ph.SR]

Nayakshin, S., Rappaport, S., & Melia, F. 2000, ApJ, 535, 798

Neilsen, J., & Homan, J. 2012, ApJ, 750, 27

Neilsen, J., Remillard, R. A., & Lee, J. C. 2011, ApJ, 737, 69

Nixon, C., King, A., Price, D., & Frank, J. 2012, ApJL, 757, L24

Nixon, C., & Salvesen, G. 2014, MNRAS, 437, 3994

Obst, M., Pottschmidt, K., Lohfink, A. M., et al. 2013, in AAS/High Energy Astrophysics Division, Vol. 13, AAS/High Energy Astrophysics Division, 126.54

Oishi, J. S., & Mac Low, M.-M. 2011, ApJ, 740, 18

Orosz, J. A., & Bailyn, C. D. 1997, ApJ, 477, 876

Orosz, J. A., Steiner, J. F., McClintock, J. E., et al. 2014, ApJ, 794, 154

Papaloizou, J. C. B., & Pringle, J. E. 1983, MNRAS, 202, 1181

Parmar, A. N., Angelini, L., & White, N. E. 1995, ApJL, 452, L129

Plant, D. S., Fender, R. P., Ponti, G., Muñoz-Darias, T., & Coriat, M. 2015, A&A, 573, A120

Potter, W. J., & Balbus, S. A. 2014, MNRAS, 441, 681

Pottschmidt, K., Chernyakova, M., Zdziarski, A. A., et al. 2006, A&A, 452, 285

Pringle, J. E. 1992, MNRAS, 258, 811

Pudritz, R. E., & Norman, C. A. 1983, ApJ, 274, 677

Reid, M. J., McClintock, J. E., Steiner, J. F., et al. 2014, ApJ, 796, 2

Remillard, R. A., & McClintock, J. E. 2006, ARA&A, 44, 49

Rothstein, D. M., Eikenberry, S. S., Chatterjee, S., et al. 2002, ApJL, 580, L61

Różańska, A. 1999, MNRAS, 308, 751

Różańska, A., & Czerny, B. 2000, A&A, 360, 1170

Rybicki, G. B., & Lightman, A. P. 1986, Radiative Processes in Astrophysics

Sai, K., Katoh, Y., Terada, N., & Ono, T. 2013, ApJ, 767, 165

Saito, K., Yamaoka, K., Fukuyama, M., et al. 2006, in VI Microquasar Workshop: Microquasars and Beyond

Sala, G., Greiner, J., Vink, J., et al. 2007, A&A, 461, 1049

Sanbuichi, K., Yamada, T. T., & Fukue, J. 1993, PASJ, 45, 443

Schober, J., Schleicher, D. R. G., Federrath, C., Bovino, S., & Klessen, R. S. 2015, ArXiv e-prints, arXiv:1506.02182 [physics.plasm-ph]

Seifina, E., Titarchuk, L., & Shaposhnikov, N. 2014, ApJ, 789, 57

Shakura, N. I., & Sunyaev, R. A. 1973, A&A, 24, 337

Shidatsu, M., Ueda, Y., Tazaki, F., et al. 2011, PASJ, 63, 785

Simon, J. B., & Hawley, J. F. 2009, The Astrophysical Journal, 707, 833

Smale, A. P., & Boyd, P. T. 2012, ApJ, 756, 146

Smith, D. M., Dawson, D. M., & Swank, J. H. 2007, ApJ, 669, 1138

Smith, D. M., Heindl, W. A., & Swank, J. H. 2002, ApJL, 578, L129

Sorathia, K. A., Krolik, J. H., & Hawley, J. F. 2013, ApJ, 777, 21

Soria, R., Broderick, J. W., Hao, J., et al. 2011, MNRAS, 415, 410

Soria, R., Wu, K., & Johnston, H. M. 1999, MNRAS, 310, 71

Soria, R., Wu, K., Page, M. J., & Sakelliou, I. 2001, A&A, 365, L273

Spruit, H. C. 1996, in NATO Advanced Science Institutes (ASI) Series C, Vol. 477, NATO Advanced Science Institutes (ASI) Series C, ed. R. A. M. J. Wijers, M. B. Davies, & C. A. Tout, 249

Steeghs, D., McClintock, J. E., Parsons, S. G., et al. 2013, ApJ, 768, 185

Steiner, J. F., McClintock, J. E., Orosz, J. A., et al. 2014, ApJ, 783, 101

Subramanian, K. 1999, Physical Review Letters, 83, 2957

Taam, R. E., Liu, B. F., Meyer, F., & Meyer-Hofmeister, E. 2008, ApJ, 688, 527

Tagger, M., & Varnière, P. 2006, ApJ, 652, 1457

Tagger, M., Varnière, P., Rodriguez, J., & Pellat, R. 2004, ApJ, 607, 410

Tamura, M., Kubota, A., Yamada, S., et al. 2012, ApJ, 753, 65

Tomsick, J. A. 2006, Advances in Space Research, 38, 2805

Tomsick, J. A., Corbel, S., Goldwurm, A., & Kaaret, P. 2005, ApJ, 630, 413

Tomsick, J. A., Kaaret, P., Kroeger, R. A., & Remillard, R. A. 1999, ApJ, 512, 892

Tomsick, J. A., Lapshov, I., & Kaaret, P. 1998, ApJ, 494, 747

Tomsick, J. A., Yamaoka, K., Corbel, S., et al. 2009, ApJL, 707, L87

Tomsick, J. A., Kalemci, E., Kaaret, P., et al. 2008, ApJ, 680, 593

Truss, M., & Done, C. 2006, MNRAS, 368, L25

Val-Baker, A. K. F., Norton, A. J., & Negueruela, I. 2007, in American Institute of Physics Conference Series, Vol. 924, The Multicolored Landscape of Compact Objects and Their Explosive Origins, 530

Viallet, M., & Hameury, J.-M. 2007, A& A, 475, 597

Wijers, R. A. M. J., & Pringle, J. E. 1999, MNRAS, 308, 207

Wilms, J., Nowak, M. A., Pottschmidt, K., et al. 2001, MNRAS, 320, 327

Wood, M. A., Still, M. D., Howell, S. B., Cannizzo, J. K., & Smale, A. P. 2011, ApJ, 741, 105

Woods, D. T., Klein, R. I., Castor, J. I., McKee, C. F., & Bell, J. B. 1996, ApJ, 461, 767

Appendix A

Approximating opacity

The various contributions of: Kramer's opacity κ_K, Thomson opacity κ_T, partially-ionized hydrogen opacity κ_{H^-}, grain and molecular opacity κ_{gm}, and electron-conduction "transparency" κ_{ec}^{-1} can be composed in the following approximate, analytical way:

$$\kappa_{\text{tot}}^{-1} = \left[\left(\left(\kappa_T + \kappa_K\right)^{-1} + \kappa_{H^-}^{-1}\right)^{-1} + \kappa_{gm}\right]^{-1} + \kappa_{ec}^{-1} \tag{A.1}$$

where the specific approximations I use are

$$\kappa_T = 0.35\left(1 + 2.7\times 10^{11}\frac{\rho}{T^2}\right)^{-1}, \tag{A.2}$$

$$\log\kappa_K = \texttt{smin}\left[\log\left(\frac{5\times 10^{24}\rho}{10^{16}\rho^{0.175} + T^{7/2}}\right), 4.5 + \log\left(\frac{\rho}{10^{18}T^3}\right) - 1.6(\log T - 4.6)\right], \tag{A.3}$$

$$\kappa_{H^-} = 10^{-32}\rho^{0.2}T^9, \tag{A.4}$$

$$\kappa_{gm} = \left(1 + \texttt{pow}[10, (14.13\log T - 0.267\log\rho - 46.13)]\right)^{-1}, \tag{A.5}$$

$$\kappa_{ec} = 2.6\times 10^{-7}\left(T/\rho\right)^2\left(1 + 6.3\times 10^{-5}\rho^{2/3}\right), \tag{A.6}$$

all densities and temperatures are understood to mean their value in cgs units, and `smin[]` refers to a smoothed minimum function.

As far as I know, original credit belongs to Prof G. Knapp for the clever arrangement.

To understand its efficacy it may help to visualize the equivalent resistance network in Fig.(A.1), and note that κ_{H^-} is strangely placed because the approximation used doesn't fall off at high temperature so it is added in parallel with high-T dominant κ_T and κ_K to produce the same effect.

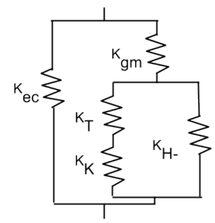

Figure A.1: The resistor analogy to A.1 though note non-intuitive placement of κ_{H^-} in parallel (see text)

To tune the analytical fits and judge their final accuracy, I stitch together opacities tabulated for high and low temperatures by Iglesias & Rogers (1996) (the OPAL project) and Ferguson et al. (2005) respectively. Fig.(A.2) compares this analytical approximation with tabulated values. I experimented with more rigorous spline fitting, but these slowed down the tabulation in `Mathematica` and tended to subdivide the cold branch.

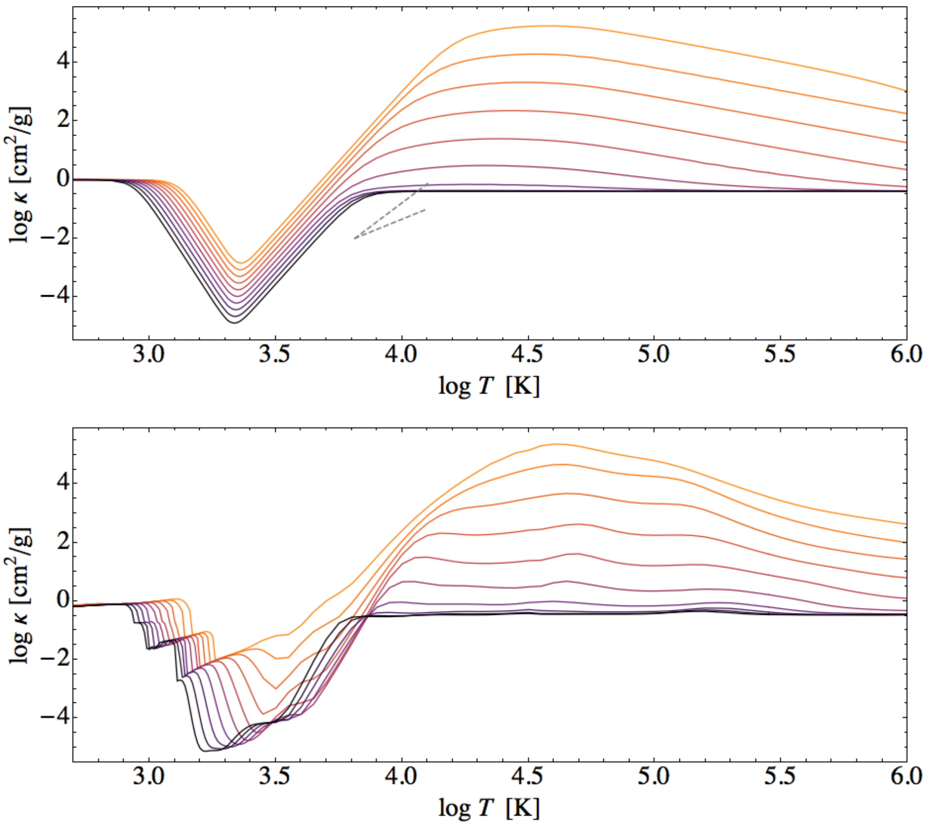

Figure A.2: Rosseland mean opacities plotted in temperature and sub-sampled in $\log(\rho/T_6^3)$ from 0 (orange) to -8 (purple) where the bottom plot is based on OPAL and lower-temperature tables, and the top plot shows the analytical fit. The gray dashed wedge in the top portion indicates the range of slopes yielding the basic PHII